Panoramic Interstellar Gas & Dust Observational Study of Massive Star Formation Based on Accurately Estimated Distances

Chibueze James Okwe

Department of Physics & Astronomy,
Graduate School of Science & Engineering,

Kagoshima University

A Dissertation submitted to the
Graduate School of Science and Engineering,
Kagoshima University
for the degree of

Doctor of Philosophy (PhD),

March, 2013

1. Reviewer: Professor Handa Toshihiro

2. Reviewer: Associate Professor Kameno Seiji

3. Reviewer: Associate Professor Nakanishi Hiroyuki

Day of the defense:

Signature from head of PhD committee:

Abstract

Very long baseline interferometry (VLBI) provides us with a useful tool for the study of the maser 3-dimensional kinematics and astrometry of massive star-forming regions. High-resolution sub-millimeter observations provide complementary information for understanding the nature of the driving sources of the maser kinematics. This dissertation is focuses on study of massive star formation with the aim of unveiling their evolutionary sequence, and also uncovering their formation scenario observationally.

The three theoretical models of massive star formation are; [1] merging of less massive stars, [2] competitive accretion in a protocluster environment, and [3] gravitational collapse involving high-rate, disk-assisted accretion into the core which helps to overcome radiation pressure. The results of the works in this dissertation along with more future work will test theory [1] and also provide useful parameters for other theories.

We conducted multi-epoch VLBI water maser spatio-kinematics study of HW3d object of Cepheus A massive star forming region with VLBI Exploration of Radio Astrometry (VERA). Adopting the parallax distance of 700 pc, we measured the relative proper motions of 30 H_2O maser features, whose spatio-kinematics traces a compact bipolar outflow. This outflow is highly collimated and expanding through $\sim$ 280 AU (400 mas) at a mean velocity of $\sim$ 20.7 km s^{-1} ($\sim$ 6 mas yr^{-1}) without taking into account the turbulent central maser cluster. The estimated opening angle of the outflow is 20.1°. The dynamical time-scale of the outflow is estimated to be $\sim$ 100 years. Our results provide strong support that HW3d harbors an internal massive young star, with the outflow tracing a very early phase of star formation. We also have analyzed Very Large Array (VLA) archive data of 1.3 cm continuum emission in 1995 and 2006 obtained towards Cepheus A,

indicating the existence of distinct young stellar objects (YSOs) in HW3d and/or strong variability in one of their radio continuum emission components.

Multi-epoch VLBI astrometry of NGC 6334I(North) massive star forming region with the Japanese VLBI Network (JVN) yielded the annual parallax to be 0.89±0.1 mas, corresponding to a distance of 1.12±0.1 kpc. It also includes JVN multi-epoch study of the spatio-kinematics of the H_2O masers detected towards SMA1 object, which shows some interesting bipolar outflow structure, traced by the maser proper motions, confirming the presence of a disk-associated young stellar object in SMA1.

We conducted a complementary high-resolution millimeter observations of NGC 6334I(N) using the Sub-millimeter Array (SMA). The results show not only the resolved continuum sources associated with the YSO candidates but also the lines that helps us classify the YSOs into hot or cold cores. SM2, a newly resolved YSO, having a core temperature of about 60 K is found near the boundary between the NGC 6334I and I(N) region. The pre-existence of H_2O masers prior to the formation of hot core in SM2, confirms that conditions suitable for maser emissions are reached between the cold and hot core phases of evolution of a massive star.

We conducted single dish ammonia line mapping observations of the molecular gas at the edge of the Monkey Head Nebula (MHN) in the Gemini OB1, estimated the kinetic temperature distribution and the virial & local thermodynamic equilibrium (LTE) mass of the cloud. We found only cold gas at the interface between the cloud and the ionized gas of the HII region, and warmer gas around a compact HII region, S252A. To confirm that it is not an artifact morphology due to obscuration by dust extinction, we conducted 3.5 cm (8.4 GHz) continuum observation, which traced the real distribution of the ionized gas. And the result was very similar to the optical image, so there was no visible interaction between the expanding HII region and the warmer gas around the compact HII region. This suggests that the exciting star of S252A formed spontaneously rather than through a sequential scenario due to the expanding HII region of the Monkey Head

Nebula. Using the Wide-field Infrared Survey Exploration point source catalog, we explored the low-mass star distribution in the region to trace any sequence in their formation. But the distribution of evolved young stellar object (class I and II YSOs) extracted from the catalog did not show any pattern in support of sequential star formation scenario, thus we proposed that the exciting star of S252A formed spontaneously.

Gleaning from our results, we tried to describe the evolutionary sequence of massive star formation in the light of our maser proper motion study and the sub millimeter comparative work. Using dynamical timescale approach, we have proposed the possible path of massive star formation. To follow up on some of the interest results contained in this thesis, I have suggested future works, which includes conducting studies similar to our work on Gem OB1 to confirm the dominant scenario of OB stars formation. This would likely lead to a modification of the currently accepted sequential formation scenario which does not hold true in the case of OB star associated with S252A .

To my Pearl, Chibueze Chioma Ezine for being the most supportive wife,
and to our energetic son, Chibueze Justin Jahbuike.

Acknowledgements

It has been an awesome journey of multiple laps, from the first phase of learning Japanese language, to the last phase of accomplishing my research goals. The support of a good number of people sum up to the successful completion of this PhD work. Firstly, the encouraging words of my Pearl, Chibueze Chioma Ezinne, produced echoes which kept resounding to motivating me to go on through difficult times of the research. Our lively son, Chibueze Justin Jahbuike, who joined us in the middle of the journey was always ready to play with daddy, relieving me of some of the accumulated academic stress.

I would like to acknowledge the support and encouragement of my Advisors, Prof. Toshihiro Handa, Prof. Toshihiro Omodaka, Ass. Prof. Seiji Kameno, Ass. Prof. Hiroyuki Nakanishi, Ass. Prof. Hiroshi Imai, and Asst. Prof Akiharu Nakagawa. They were always available to aid me when I met difficult challenges during the course of my PhD program. I have acquired useful knowledge and skills in radio astronomy, very long baseline interferometry (VLBI) technique including the special parts of VLBI Exploration of Radio Astrometry (VERA) research. Thank you Dr. Osamu Kameya for providing me with the Cepheus A VERA data. I will also like to thank Prof. Makoto Nakano (Oita University), Dr. Kazuyoshi Sunada (Mizusawa VLBI Observatory), Dr. Takumi Nagayama (NAOJ), Mr. Tatsuya Kamezaki for their support. My appreciation also goes to all those working in the VERA team, ranging from the observation scheduler (Dr. Shibata) to those in the operations and data correlation center in National Astronomical Observatory (NAOJ), Mitaka, Tokyo. Thanks Danny for making time to guide me through some of the research procedures. Your strong motivations are really appreciated. I am also grateful to Prof. Torrelles J.

M (Chema), collaborating with him (a professional in the field) was like a dream come true.

Furthermore, I would like to thank the Japanese Ministry of Education, Culture, Sports, Science and Technology (MEXT) for sponsoring my PhD studentship. Thanks also to National Radio Astronomy Observatory (NRAO) for the Graduate Internship program which served as a great boost to my research work. And to my host researchers, Dr. Todd Hunter, and Dr. Crystal Brogan, I am very appreciative of the opportunity.

Thanks Mum for coming around to take care of baby Justin, and to uncle Godwin Ogbonnaya, thanks for believing that I have got what it takes to succeed and for playing key supportive role. Ekeoma Emmanuel Chibueze (Ceemah), you are just the kind of brother everyone would dream to have, and to my little, pretty niece, Precious, I am still excitingly longing to have you in my arms. To my younger brothers, I sure look forward to playing with you all the way we did 2 decades ago.

My appreciation also goes to all the students in the Astrophysics Group of Kagoshima University, all our scientific discussions were worthwhile.

Chux, thanks for being my 'second eye' when I need it the most.

Contents

List of Figures

LIST OF FIGURES

LIST OF FIGURES

List of Tables

LIST OF TABLES

1

Introduction

"Subduction of the things around us, only possible through our understanding of the universe around us." —— James Chibueze

1.1 Massive Star Formation – The History and Problems

The formation of stars in general constitutes an integral part of past and present studies in Astronomy. Based on our current understanding, low-mass stars ($M_{\rm star} < 8M_{\odot}$) form by the collapse of molecular clouds, which leads to the formation of the pre-stellar cores. The pre-stellar cores subsequently become gravitationally unstable, and start to isothermally collapse, in which case the gravitational energy given out are radiated away, leaving the collapsing pre-stellar core isothermal. This phase results in a dense, opaque, hydrostatic object at the core surrounded by a gaseous envelope. As the gaseous envelope accumulates more matter and increases in its density, the escape of the radiated gravitational energy becomes increasingly difficult, leading to steady drop in the luminosity of the core (Hayashi track). The core starts accretion through which it accumulates most of the its stellar mass from its accretion disk and the surrounding infalling envelope. This phase is also associated with a corresponding rise in the temperature of the core, as well as a violent, high velocity, collimated bipolar outflow of materials from the central object. Evidently, the bipolar ejection aids the release of excess angular momentum contributed by the infalling materials. As the central object accretes enough mass it gets into the pre-main-sequence phase. With the increase in the core temperature, radiation dominates the original convective energy transport as

the star gradually gets into the main sequence phase with enough core density, and hot enough to begin nuclear burning of hydrogen. Eventually the radiative pressure becomes high enough to stop accretion. At this point, the luminosity of the formed star is mostly from the hydrogen burning.

The formation scenario of low-mass stars briefly described above fails as we try to scale it up and adopt it to explain massive star formation. The major difference lies in the fact that massive stars reach main-sequence phase, producing substantial amounts of stellar radiation and winds before the end of its accretion phase. This can be shown by comparing the Kelvin-Helmholtz contraction timescale of a massive proto-stellar object, given by $t_{KH} = \frac{GM^2}{RL}$, (where M is the mass of the proto-stellar object, R is its radius and L is its luminosity), to its accretion timescale $t_{accretion} \sim M/\dot{M}$, where $\dot{M}$ is the accretion rate. For massive stars, assuming the Osorio et al. 1999 accretion timescale, $t_{accretion} \sim 10^5$, the $t_{KH} < 10^5$ yr (Zinnecker & Yorke, 2007). Unlike their low-mass counterparts which ends its accretion phase and blows away the gaseous envelope that supplied the formation materials before entering the main-sequence phase, massive stars continues to accrete materials into its core even after entering the main-sequence phase.

Massive stars ($M_{star} > M_{\odot}$) are key players in galactic evolution, having strong influences on the interstellar medium. The understanding of interstellar medium, as well as evolution of galaxies will not be complete without the understanding of massive star formation. This is one strong motivation toward the various aspects of massive star studies contained in this dissertation, ranging from the spatio-kinematics of masers in massive star-forming regions, to their astrometric measurement, and influence on their immediate environment.

Though we do not yet fully understand how massive stars form, there exist a few fundamental knowledge on high-mass star formation. Among the things we know about massive stars include that they form in dense, and very large molecular clouds called giant molecular clouds. Observationally, column density, the size, mass, and temperature distribution, and other physical parameters of dense molecular clouds which are natal environment of high-mass stars can be determined (Toujima et al. 2011; Chibueze et al. 2012). The typical temperature of giant molecular clouds are $\sim$ 10 K (Chibueze et al. 2012). High-mass stars form deeply embedded in their natal molecular clouds which are located several kilo-parsecs in distance away from us. The closest known

MSF region is the Orion KL at 437 pc (Hirota et al. 2007), followed by Cepheus A at $\sim$ 700 pc (Moscadelli et al. 2009, Dzib et al 2011). The distance factor is one of the major reasons for the slow progress in understanding massive star formation. Yet another factor that impedes our understanding of massive star formation is the fact that they form in close proximity to each other. Megeath et al. 2005 reportedly identified five early-phase protostellar OB stars in W3 IRS5 clustered within 5600 AU using a space-based near-infrared telescope. Granted, infrared observations can sometimes be able to resolve some massive protostars, but could also suffer from dust extinction which may obscure a significant fraction of the protostellar cores deeply embedded in the molecular cloud. Alternatively, millimeter and sub-millimeter dust continuum emissions which remain optically thin even at high column densities ($N_{\rm H} \geq 10^{25}{\rm cm}^{-2}$) are used to trace massive young stellar cores in their natal environment (see Hunter et al. 2006).

Dense molecular cores are sustained by internal thermal and non-thermal gas pressure against the gravitational force. This is aimed at preventing the cores from collapsing. Cores which are more massive compared with Jean's mass can no longer be supported by the internal gas pressure and thus gravitationally collapse giving out gravitational energy which heats up the core. This hot molecular core phase is known to be associated with accretion disks, jets, and other violent ejections in form of outflows (e.g. bipolar outflows).

Based on Zinnecker & Yorke (2007), the evolution of high-mass stars from a giant molecular cloud take place in the following sequence; (i) Cold dense molecular cores or filaments formation, induced by gravo-turbulent cloud fragmentation (Mac Low & Klessen 2004). This means that supersonic turbulence rapidly produces localized compressed pockets of gas, some of which remain gravitationally bound and provide the initial conditions for collapse (Padoan & Nordlund 2002; Klessen et al. 2005). A characteristic density of about 10^5 cm^{-3} and temperature of 10 – 15 K results from the equation of state of dusty molecular gas of solar abundance (Jappsen et al. 2005, Larson 2005). (ii) Non-homologous gravitational collapse of portions of the cores into optically thick, pressure-supported protostellar embryos with initial masses of the order of 10^3 $M_\odot$ (Larson 1969, Bate 2000). The term non-homologous collapse refers to the fact that the relative distribution of material changes, as opposed to a homologous or

self-similar collapse. (This is different from Shus (1977) inside-out collapse of a self-similar isothermal sphere). (iii) Accretion of material onto protostellar objects as they evolve toward the main sequence. For low-mass objects the accretion stops well before hydrogen burning commences, and these premain-sequence objects of fixed mass then slowly and quasi-hydrostatically contract to the main sequence (Palla & Stahler 1993, Baraffe et al. 2002). However, high-mass objects eventually start burning hydrogen and develop radiation-driven winds as they continue to accrete and evolve up the main sequence to hotter and more luminous states (Kudritzki 2002). (iv) Disruption of the birth cloud, as the first high-mass stars strongly influence their environment by their winds, outflows, and UV radiation, and eventually become supernovae. The most massive stars go supernova ~ 3 Myr after their birth. When the remnant molecular cloud has been dissipated, the result is mostly a cluster of OB stars or an OB association, with an associated co-spatial population of lower mass stars (Zinnecker, McCaughrean & Wilking 1993). Often, several evolutionary stages of star formation can be found side by side; the 30 Dor region in the LMC is a good example (Walborn et al. 1999). (extract of Zinnecker & Yorke 2007)

The choice of the very long baseline interferometry (VLBI) as the technique employed in this PhD work is informed by its provision of the required high angular resolution for probing the formation of high-mass stars. Such high resolution is difficult (currently not possible) to obtain with optical observation, considering also that massive stars form embedded in their clouds. Infrared and single dish radio observations are useful for investigating the effects of their strong winds on their surrounding molecular gas clouds.

1.1.1 Radiation Pressure and Ionization Feedback in Massive Stars

Massive stars reach the main sequence phase while still accreting materials into the cores (Shu et al. 1987), but it is natural to expect the large radiation pressure from the nuclear hydrogen burning to overcome the gravitational force of the star and halt the infall of gas and natal materials into the central cores. A number of perplexing questions arise from the radiation pressure problem of massive stars:
1. What is the upper limit of the mass of a star at which radiation pressure due to high luminosity of high-mass stars can reverse the incoming natal gas and dust materials and completely stop the accretion process?

2. How are materials accreted into the central mass from the surrounding gas and dust envelop? Does spherical symmetric accretion or disk-assisted accretion hold the answer to these important questions?

The first simulation to verify the upper limit of the mass of a star beyond which accretion cannot continue was done by Larson & Starrfield (1971). They obtained the upper mass limit to be of the range of 50 – 60 $M_{\odot}$. Kahn (1974) and Wolfire & Cassinelli (1987) repeated similar simulation with the assumption of a spherically symmetrical accretion scenario and obtained the upper limit to be 20 – 40 $M_{\odot}$ for typical galactic metallicity. Accretion through a disk as well as high accretion rate ($> 10^{15} M_{\odot} yr^{-1}$) could be a means of subduing the radiative pressure.

Nakano (1989), Nakano, Hasegawa, & Norman (1995) and Jijina & Adams (1996) attempted a non-spherically symmetric accretions case based on disk-assisted accretion assumption. The idea behind this calculation technique involves constraining the accretion into the massive pre-stellar through a small solid angle of an accretion disk. Their results show that radiation pressure of the young stellar object remained a significant impedance to the disk-assisted accretion. Evidently, with the disk-assisted accretion, the upper mass limit is $\sim$ 40 – 60 $M_{\odot}$ (Yorke & Sonnhalter 2002). If radiation pressure should stop accretion into the massive young stellar object (MYSO) when it reaches the upper mass limit, then the problem of explaining how star of masses up to 100 $M_{\odot}$, such as the one observationally detected and reported by Walborn et al. (2004) are formed becomes more perplexing.

1.1.2 Theories of Massive Star Formation

Theories of massive star formation constitute the most debated area of massive star formation studies. All existing theories and concepts of massive star formation (MSF) have their strengths as well as their weaknesses. This subsection will focus on the three main theories of MSF, pointing out their merits and demerits. It is vital to note that any of the theories may be obtainable in star-forming cloud depending on its initial and environmental conditions. The three main theories of MSF are (1) monolithic collapse and disk accretion, (2) competitive accretion and runaway growth, and (3) stellar collisions and mergers.

1. INTRODUCTION

Monolithic collapse and disk accretion was proposed by Yorke & Sonnhalter (2002). This theory suggests that high-mass star form through the collapse of isolated, non-magnetic, massive molecular cores, followed by a disk-assisted accretion. This is based on their simulation results obtained from their consideration of 30 $M_{\odot}$, 60 $M_{\odot}$, 120 $M_{\odot}$ molecular cores using a frequency-dependent radiation hydrodynamics code. Yorke & Sonnhalter successfully accreted 33.6 $M_{\odot}$ and $\sim$ 43 $M_{\odot}$ into the central cores for the 60 $M_{\odot}$ and the 120 $M_{\odot}$ molecular cores, respectively. In each case, a disk formed around the accreting young stellar object. Krumholz, Klein & McKee (2005) similarly reported the accretion of $\sim$ 27 $M_{\odot}$ ($\sim$ 25 $M_{\odot}$ for a turbulent case), also attesting to the formation of a disk around the protostar. The weakness of this theory is that the innermost part of the collapsed core cannot be spatially resolved. Therefore, it is difficult to tell if the core is a single stellar system, or a cluster of cores of a multi-stellar system. Thus, the assumption that all materials accumulate on a single object through accretion is the demerit of this theory, though it provides the upper limit to the mass of stars that could possibly be formed for a particular case.

Competitive accretion and runaway growth was proposed by Bonnell et al. (1997, 2001). This theory highlights two important factor in massive star formation, location and time of birth. In a giant molecular cloud housing a cluster of protostars, the location of each protostar determines the possibility of becoming a high-mass or low-mass star. The protostars located at the center of the protostellar cluster have more natal material (gas) reservoir as more gas flow down toward the center. The gravitational potential of the protocluster clump or cluster of stars funnels a significant fraction of gaseous material to the cluster center, there to be accreted by the massive protostars. They also argued that early birth of a protostar may afford it an advantage in the competitive accretion process. Krunholz, McKee and Klein (2005) tried to debunk this theory by arguing that cloud housing a cluster of protostars are supported by turbulent motions, in which case, the analytical consideration by Krunholz, McKee and Klein (2005) argued the protostellar masses cannot grow in such a turbulent environment. Both criticisms were done assuming global variable system. Applying analytical and numerical method, Bonnell & Bate (2006) buttressed their theory that massive stars form through a competitive accretion process after a gravitational collapse. Assuming local properties, rather than global variables, they showed that fews stars located at the center of a local stellar system would initially accrete low relative velocity gas as

a result of the influence of turbulence. Subsequently, after acquiring enough mass to maintain a high-accretion rate, accretion of higher relative velocity gas begins and leads to the formation of high-mass stars. Most of the stars located away from the center of the stellar system, as well as those that enter the higher relative velocity gas region with insufficient mass to maintain a high accretion rate, can only retain their low-mass status. The strength of competitive accretion is that it provides a physical mechanism to gather the matter required for forming the star. The fundamental difference between the monolithic collapse and the competitive is that in monolithic collapse, the mass is assumed to be gathered before the start of star formation, while in the competitive accretion the mass is gathered during the star formation process.

Stellar collisions and mergers is based on the fact that massive stars form in close proximity of each other. The closeness of high-mass stars are considered too tight , thus, sufficiently large gas reservoir for monolithic collapse may be unavailable. High density cluster of massive stars or at least intermediate-mass stars is required for stellar collisions and mergers to be possible. The estimated average star-to-star separation, d, is $d = n^{-1/3}$, where n is the threshold stellar number density. While being the most plausible theory to explain the formation of massive stars in some regions, the required initial condition is not very common (see below extract from Zinnecker & Yorke 2007).

Stellar mergers will be rare and only relevant for the most massive stars in the richest young clusters (such as young globular clusters). One reason to invoke stellar mergers is that ongoing competitive accretion (mass loading) increases the stellar density in the cluster center (mass segregation at birth), potentially to the point where grazing collisions become unavoidable. Stellar collisions with small impact parameters might be the process that forms rapidly rotating massive stars and hence the progenitors of (slow, long-duration) gamma-ray bursts.

1.2 The Big Picture

This section is an illustrative description of the sequence of processes leading to the formation of high-mass stars based on information obtained from my PhD research along with other relevant newly published results. Please note how each chapter of this dissertation contributes in the big picture in description that follows. Assuming massive star formation (representing the big picture) to be a huge puzzle made up of

multiple pieces, each of the pieces represent one of the evolutionary phases of the big picture. In this puzzle, the most important piece is the dense molecular cloud without which the next evolutionary phase would be impossible. It is necessary to note that the process leading to the formation of the dense molecular cloud itself is not considered in this puzzle. Starting with the dense molecular cloud ($\sim$ 15 K), it is expected that turbulence coupled with gravitational instabilities will lead to the collapse of the cloud and the formation of cold cores ($\sim$ 20 K), almost indistinguishable from the rest of the cloud in temperature. The column densities of the cold cores are higher than the rest of the molecular cloud. The higher density will imply more collisions within the core, and the trapping of more of the surrounding natal materials. Between the cold core phase and the formation of hot cores ($\sim$ 50 K), condition for the excitation of masers are reached, therefore masers especially water masers are pumped. Observationally, there are evidence of violent (periodic) ejections from the core traced by maser proper motions which signify the motion of the gas clumps around the core (*see Chapter 3*). In the hot core phase, the turbulence in the core is already translating into increasing kinetic temperatures, and a disk begins to form around the core (*see Chapter 5 for an example*). The disk formation coincides with the formation of a hyper-compact H II region of size ($\sim$ 0.03 pc) as a result of the ionizing effect of the photons emitted by the hot core (Beltán et al. 2006). This disk aids accretion (infall of material) into the core leading to an increase in its mass. While materials are being accreted into the core, more photons are being released, thus the hyper-compact H II region expands to a size of $\sim$ 0.1 pc (ultra-compact $\sim$ 100 K), then to a compact H II region, and then becomes a more extended H II region. As the ultra-compact H II evolves high-velocity ($\sim$ 500 km s^{-1}) jet is formed. As the jet passes through the surrounding materials, they acquire some kinetic energy from the jet and accelerates slowly, giving rise to low-velocity bipolar outflow with small opening angle (collimated) (examples are discussed in Chapters 3 and 4). Over time, materials some angular distance away from the jet are also effected by the motion, leading to the formation of wide-angle outflows (Torrelles et al. 2011). At this point the massive star is already visibly evolved.

1.3 Astrophysical Masers

Microwave amplification by stimulated emission of radiation, maser, is the microwave equivalent of laser. Russian scientists were instrumental in the laboratory development of masers as well as the theoretical description of the operating principles of maser in the early 1952. Not until the next decade were masers actually detected in nature.

1.3.1 History of Astrophysical Masers

The discovery of maser in space was done by Weinreb (1963) in his OH detection in absorption line towards Cassiopeia A. Subsequently, he and his collaborators also made the first detection of maser emission (Weaver et al. 1965). They detected the 1665-MHz main line transition of the hydroxyl ion (OH) towards several interstellar H II regions. Weaver et al. (1965) named OH emission the mysterium because they found the ratio of the 1667-MHz/1665-MHz emission to be inconsistent with either optically thin or optically thick thermal emission. This is sure not a thermal but synchrotron emission and their obtained result is understandable with current knowledge background. Their work opened the door to further discoveries of many other species of maser.

Cheung et al. (1968) became the first to detect the ammonia (NH_3) line in space. Happily, he and his collaborators also discovered water (H_2O) maser in Orion nebular. Though their observation had poor position accuracy of about $1'$, it marked the beginning of new era in maser studies. Snyder et al. (1969) found the formaldehyde (H_2CO), while the methanol (CH_3OH) maser was first detected by Ball et al. (1970). Like the H_2O masers, CH_3OH in all its classes have become a vital tool for the study of massive star formation. In fact, the detection of 6.7 GHz around a protostellar object is an evidence that the star in the making must be a massive star. Silicon oxide (SiO) masers was later discovered by Snyder & Buhl (1974). So many other different maser species were found, along with the detection of new transitions of originally detected species.

1.3.2 Fundamentals of Maser

To understand the fundamentals of maser emissions, it is important to first understand terms like pumping mechanism and population inversion. For masers to be emitted, at least three (in actual sense more than three energy levels) are required for the

distribution of the molecules. If we designate the energy levels as E_1, E_2, E_3, where E_1 has sub-energy levels and are more stable than E_2, which is more stable than E_3 (see Figure 1.1). Pump mechanism is the natural process in interstellar medium which can excite molecules in E_1, giving them enough excitation energy to move from E_1 to E_3. Without this kind of process, masers cannot be emitted.

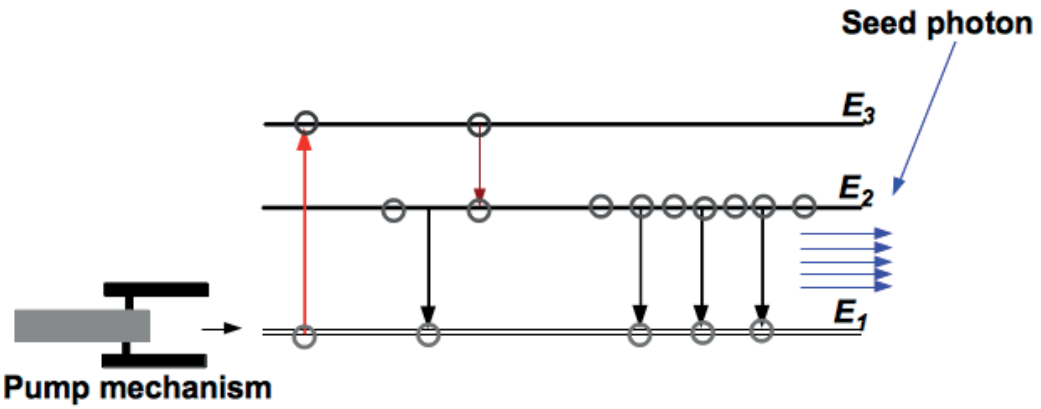

Figure 1.1: Maser emission excitation mechanism - Pictorial illustration of how maser emission is excited and pumped in nature.

Molecules have very high affinity for lower energy levels. They would prefer E_1 to E_2 or E_3, similarly there is preference for E_2 compared to E_3. Population inversion is a situation where the number of molecules in a higher energy level is higher than the number of molecules in a lower and more stable energy level. Naturally, more molecules occupy E_1, but when stimulated by the pumping mechanism, they relocate to E_3, release some energy and drop to E_2. While some of the molecules release some energy and move down to E_1, the pumping process continues to stimulate more and more molecules to E_2 via E_3. The population of molecules in E_2 become higher than the population of E_1, pollution inversion is achieved.

Finally, a seed photon is required to stimulate the emission of other photons with same frequency and phase as the original photon whose energy is $hv = E_2 - E_1$. The

unabsorbed seed photon triggers the emission of multiple similar photon, that is maser emission.

1.3.3 Usefulness of Masers

In nature, masers can be found in various types of astronomical objects like star-forming regions, water fountain late-type stars, the circumstellar environments of planetary nebulae, cometary halos, extragalactic sources, and supernova remnants. Masers can be likened to indicators, which are useful in studying the environments where they are found. Masers are known for their high brightness temperature, and compact size, thus providing an excellent tool for scientific study of their natal region. For instance, we currently know that infall on the disc around massive stars are largely regulated by the magnetic field around it (Surcis et al. 2011) from maser polarization study, similarly masers have also helped reveal the fact that magnetic field helps to collimate the jet from evolved star.

Their compact nature gives us the needed advantage for accurate distance determination. VLBI annual parallax measurement is one of the currently most famous use of masers in astronomy/astrophysics. Such compact nature provide the high accuracy needed in the estimation of the distance to different sources. The Japanese VERA project is mainly aimed at observing masers source in the Milky Way and measuring the trigonometric parallaxes and their corresponding distances. At the end, making a 3-dimensional map of the distribution of stars in the Milky Way (Hirota et al. 2007, 2008, Honma et al. 2007, Choi et al. 2008, Ando et al. 2011, Imai et al. 2007, Nagayama et al. 2011).

The lifespan of masers are relatively short (a few years), indicating the variation of physical conditions of their pumping environment. Within the life time of a maser feature, a multi-epoch observation of its absolute or relative positions and intensities can be tracked. The absolute or relative proper motion of the maser feature can be traced and this provides some clues into the motion of the interstellar materials around it. This technique has been used in revealing star formation activities in massive star-forming regions like Cepheus A (Chibueze et al. 2012, Torrelles et al. 2011). Measurement of annual parallax and the tracing of the proper motion is of paramount interest to me in my research.

1.4 Very Long Baseline Interferometry

VLBI is aimed at utilizing long baseline to virtually synthesize a large telescope which is currently technologically impossible to construct, providing high angular resolution in the order of milliarcsecond (mas). There are two astronomical discoveries which motivated the development of VLBI, namely; the discovery of a few light-days size radiation emitting regions in quasars and the discover of connected-array unresolved OH masers (Burke & Graham-Smith 1997). Both findings required higher angular resolution than was obtainable then to conduct more detailed studies in them.

Fundamentally, VLBI technique is used for studying high brightness temperature (of the order of 10^6 K) sources (maser sources). These sources emit by non-thermal processes like synchrotron radiation or maser amplification. Generally, thermally radiating sources like the photosphere of stars are not detected in VLBI observations. In this thesis, all the sources explored are maser emitting sources and have been studied in one way or the other with the VLBI technique. Some of the VLBI studies has been directly conducted in the course of my PhD program, while others are previously conducted VLBI studies which provided vital information needed to conduct the part of the studies reported herein. For instance, in chapter 6, a new understanding of the formation scenario of OB stars around the Monkey Head Nebula is considered. This is not directly as a result of VLBI observations, but rather single-dish NH_3 and 8.4 GHz continuum observations. Yet, we employed the VLBI parallax distance information of the source reported in Reid et al (2009) in order to accurately extract the physical parameters of the region under consideration. And this led to our proposed modified view of the OB star formation scenario in the region. VLBI is useful in parallax measurement, but not limited to that. It can also be used for geodetic studies. Geodetic VLBI is a technique for determining ground positions to centimeter accuracy.

Works that appear in this thesis were largely carried out with the Japanese VLBI Network (JVN), which is a collaborated project of universities and institutes that manage VLBI antennas in Japan. The project is led by Hokkaido University, the National Astronomical Observatory of Japan (NAOJ), Ibaraki University, Tsukuba University, the Geographical Survey Institute (GSI), the National Institute of Information and Communications Technology (NICT), the Japan Aerospace Exploration Agency (JAXA), Gifu University, Osaka Prefecture University, Yamaguchi University,

and Kagoshima University. It includes the VLBI Exploration of Radio Astrometry (VERA), Nobeyama Radio Observatory 45 m telescope, National Institute of Communication Technology, NICT, 34 m telescope in Kashima, Gifu 11 m telescope and other telescopes in Japan, there are some VERA only cases too. VERA is a Japan VLBI project operated by the National Radio Astronomical Observatory of Japan (NAOJ). Its goal is to map a 3-dimensional map of the Milky Way by determining the accurate distances to the stars therein by measuring their trigonometric parallax. The four 20 m VERA telescopes are equipped with a dual-beam system, enabling it to simultaneously observe a target maser source and a position reference source, thus avoid the problems of fast-switching method in terms of the variabilities in atmospheric condition. Other interferometric facilities and connected arrays used directly or indirectly in this thesis includes very long baseline array (VLBA), very large array (VLA), and some short baseline interferometers like the sub-millimeter array (SMA), Atacama Large Millimeter Array (ALMA). For details on how radio interferometer work the principles behind it, see Interferometry and Synthesis in Radio Astronomy by Thompson, Moran and Swenson.

1.5 Dissertation Goals & Overview

Understanding massive star formation will involve both small-scale and large-scale view of star-forming regions. Small-scale view involves high-angular resolution view of massive star formation through VLBI maser studies as well as high-resolution continuum study. This explores the micro-physics of massive star formation. Large-scale view involved low-angular resolution, but large scale mapping observations of massive star-forming environment. NH_3 lines mapping observations can be classified among the large-scale view of the MSF.

The principal objectives of this dissertation are:
(1) To conduct VLBI annual parallax determination of H_2O masers in MSF regions with VERA and accurately estimate their corresponding distances.

(2) To determine the relative proper motions of H_2O masers in MSF regions, thus tracing the motion of interstellar material, a reflection of the processes associated with massive star formation. As far as possible, using it as a means to trace the evolutionary stages of high-mass stars.

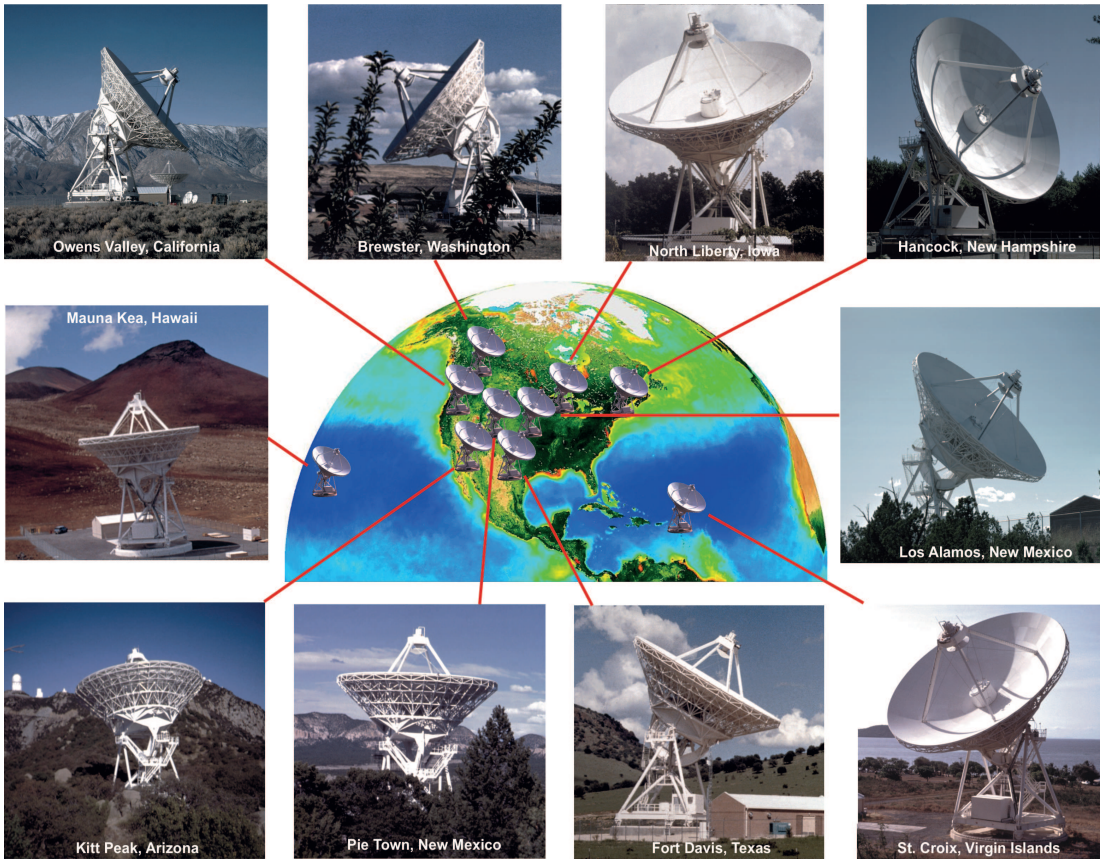

Figure 1.2: The Very Long Baseline Array (VLBA) - Locations of all the VLBA telescopes (Image courtesy of NRAO/AUI and Earth image courtesy of the SeaWiFS Project NASA/GSFC and ORBIMAGE http://images.nrao.edu/549).

Figure 1.3: Japanese VLBI Network (JVN) - Map of Japan showing the location of all the JVN telescopes. *credit http://www.astro.sci.yamaguchi-u.ac.jp/jvn/eng/index_e.html*

Figure 1.4: The Very Large Array (VLA) - Very Large Array telescopes (Image courtesy of NRAO/AUI and Earth image courtesy of the SeaWiFS Project NASA/GSFC and ORBIMAGE http://www.aoc.nrao.edu/epo/puente/views/vlaviews.index.html).

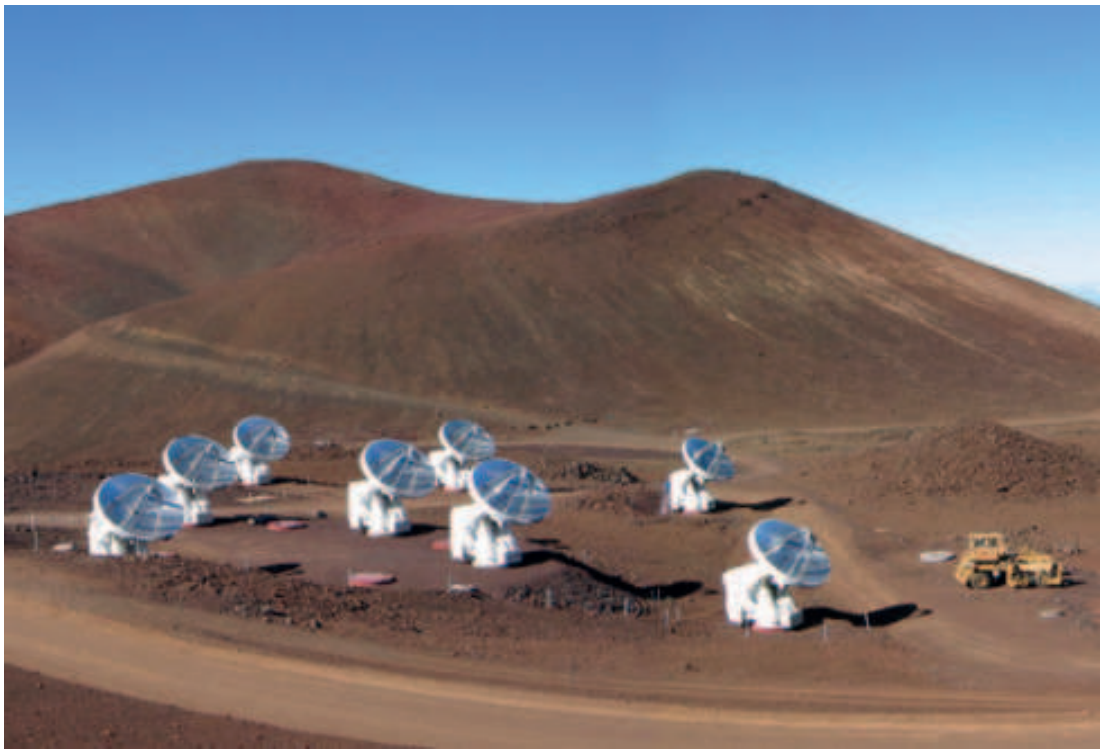

Figure 1.5: Sub-millimeter Array (SMA) - Sub-millimeter Array telescopes. *credit http://www.cfa.harvard.edu/sma/*

Figure 1.6: The Atacama Large Millimeter Array (ALMA) - Atacama Large Millimeter Array telescopes. *credit https://science.nrao.edu/science/aas/219/alma-special-session-at-the-219th-aas*

(3) To conduct high-resolution sub/millimeter continuum and line observations to resolve the unresolved sources associated with the expected masers in 2 above.

(4) Verify the accuracy of the sequential star formation and also investigate the influence of the strong winds from massive star on its immediate environment.

This dissertation is mainly composed of VLBI study of the maser 3-dimensional kinematics and astrometry of massive star-forming regions. It also includes high-resolution sub-millimeter study of massive young stellar objects in the early phases of evolution. The formation scenario of massive stars in OB associations was also explored in the light of the suggested sequential star formation scenario as previous work by Elmegreen & Lada in 1977. Though our results indicate that massive stars trigger the formation of low-mass stars near it, it suggests spontaneous formation scenario to be responsible for the formation of the high-mass stars. The following is a brief breakdown of the individual chapters of the thesis.

Chapter 1 gives an overview of the currently understood and the yet-to-be understood issues of massive star formation. This is a brief description of the historical development in understanding of massive stars and the problems associated with it. The three theories of massive star formation, namely, [1] massive star formation through the merging of less massive stars (Bonnell, Bate, & Zinnecker 1998), [2] competitive accretion in a protocluster environment (Bonnell & Bate 2006), and [3] gravitational collapse involving high-rate, disk-assisted accretion into the core which helps to overcome radiation pressure (Yorke & Sonnhalter 2002; McKee & Tan 2003; Krumholz et al. 2005, 2009) are also explained in this chapter. VLBI techniques including the phase referencing and other special procedures, as well as the fundamentals of astrophysical masers are properly described. This chapter ended with an elaborate explanation of the goals of this thesis and the approaches applied in achieving them.

Chapter 2 describes the procedures of the VLBI data reduction. Unlike the single dish data reduction, VLBI data after its correlation requires a number of key calibration procedures before the final image can be produced. Some of the sub-sections of this chapter have been dedicated to the description of some of these calibrations like amplitude calibration, bandpass calibration, phase calibration, self-calibration and then the imaging. The fundamentals of these processes are the same for the different data reduction packages (Astronomical Image Processing System, AIPS, MIRIAD, and CASA) used.

Chapter 3 is a detailed description of the results of our multi-epoch VLBI water maser spatio-kinematics studies of Cepheus A massive star forming region. This study was conducted with the VLBI Exploration of Radio Astrometry, VERA. In this chapter, the general description of the maser kinematics in the entire region is documented with more attention on the Cepheus A HW3d object. We traced for the first time proper motions of the water masers associated with the HW3d massive young stellar object. These maser proper motions traced a bipolar outflow from the object. This result well explains the elongated structure seen in the very large array (VLA) 1.3 cm continuum emission from the object. This is the first confirmative work showing the presence of an internal exciting source in HW3d. We objectively verified the maser results using the position and velocity variance and covariance matrix analyses technique. Applying an expanding flow model to the observed outflow, our result suggests that there may be more than one source within HW3d.

Chapter 4 describes our multi-epoch VLBI astrometry of NGC 6334I(N) massive star forming region. The importance of accurate distance measurement in astronomy cannot be over-emphasized. Inaccurate estimation of the distance to star-forming regions will give rise to wrong estimations of physical parameters like dust mass which are dependent on the distance. Currently, the most accurate way to determine the distance to a source is by measuring with high accuracy its annual parallax by VLBI technique. We have done this in the case of NGC 6334IN using the advantage of the VERA dual-beam system and obtained the annual parallax to be 0.89 mas, corresponding to a distance of 1.2 kpc. It also contains details of the Japanese VLBI Network (JVN) multi-epoch study of the spatio-kinematics of the water masers detected in the entire region. This is with particular attention to SMA1 object, which shows some interesting structures, traced by the maser proper motions.

Chapter 5 describes the results of our high-resolution millimeter observations of NGC 6334I(N) using the Sub-millimeter Array (SMA). These observations were conducted in such a way that they include both the continuum and millimeter line emissions. Therefore, the results show not only the resolved continuum of all the YSO candidates but also the lines that helps us classify the YSOs into hot or cold cores. SM2, a newly resolved YSO, having a core temperature of about 60 K is found near the boundary between the NGC 6334I and I(N) region. This chapter describes in details the forest of millimeter lines detected in this object and its implications.

Chapter 6 describes the novel idea born out of our study of the influence of an expanding HII region of massive OB association. Elmegreen & Lada in 1977 proposed that OB stars form sequentially due to the influence of expanding HII region. In effect, they proposed that OB stars ionized their surroundings and form HII regions, which expand and sweep together molecular gas, then due to the heating effect, the gas cloud collapse and form another generation of OB stars, and the process continues. This implies that a temperature gradient should be expected at the boundary of an expanding HII region and a molecular cloud. Gemini OB1 (also called Monkey Head Nebula) is a fitting example of such region. We conducted single dish ammonia line mapping observations of the molecular gas, estimated the kinetic temperature distribution and the virial & LTE mass of the cloud. We found only cold gas at the interface between the cloud and the ionized gas of the HII region, and warmer gas around S252A compact HII region. Because this may have been because the optical image of the nebula is obscured by dust extinction, we conducted 8.4 GHz continuum observation, which traced the real distribution of the ionized gas. And the result was very similar to the optical image. So there was no visible interaction between the expanding HII region and the warmer gas around S252A. This suggests the exciting star of S252A to have formed spontaneously rather than through a sequential scenario due to the expanding HII region of the Monkey Head Nebula. Using the Wide-field Infrared Survey Exploration point source catalog, we explored the low-mass star distribution in the region to trace any sequence in their formation. But the distribution of the class I and II YSOs extracted from the catalog didn't not show any pattern in support of sequential star formation scenario, thus we proposed that the exciting star of S252A formed spontaneously.

Chapter 7 captures the summary of the works reported in this thesis and tried to describe the evolutionary sequence of massive star formation in the light of our maser proper motion study and the sub millimeter comparative work. Using dynamical timescale approach, we have proposed the possible path of massive star formation. To follow up on some of the interest results contained in this thesis, I have suggested future works, which includes conducting studies similar to our work on Gem OB1 to confirm the dominant scenario of OB stars formation. This would likely lead to a modification of the currently accepted sequential formation scenario which does not hold true in the case of S252A associated OB star.

Chapter 8 elaborates the planned future work in follow up of the achieved results and the unanswered issues emanating from my PhD research works. These include follow-up ALMA observations toward NGC 6334I(N), in order to estimate the stellar number density and check for the possibility of stellar collisions and mergers (proposal already submitted). VERA/KVN maser study to explore the evolutionary sequence of massive stars. And finally studying other expanding H II regions apart from Gemini OB1 to verify sequential and spontaneous formation of OB stars.

2

Fundamentals of VLBI Data Reduction

2.1 Introduction

VLBI data reduction is key to obtaining images, and maser information that are needed in order to make meaningful scientific discussions. Any recorded failure in the data reduction procedure will translate into inaccurate and worse still untrue results. This underscores the importance of the reduction phase of VLBI data. This chapter will focus on the fundamental VLBI data reduction procedure and as well elaborate on the special technique (inverse phase referencing technique) applied in some of the data in order to detect weak position reference source (sometimes referred to as the phase reference source). In summary, the inverse phase referencing technique involved the application of the fringe phase solution of a bright maser spot to the position reference source data in order to detect the source in fringe fitting procedure. Details of this special technique will be discussed in the section 2.4.

2.2 Four Basic Observables of VLBI

Unlike other form of astronomical observations, VLBI observations involve obtaining radio emission signals from a radio source simultaneously with at least 2 independent telescopes. During correlation, data obtained at the same frequency are cross correlated, in the case of VERA data, the Mitaka FX correlator is used for the correlation process. This process can be viewed as a playback of the data recorded at each of the

VLBI stations for the purpose of characterizing the delay in the arrival time of the electromagnetic wave at the different station due to the difference in their locations. The end product of a VLBI observation is called visibilities.

The correlator response to the playback process can be expressed as;

$$r(\tau) = \lim_{T\to\infty} \frac{1}{2T} \int_{-T}^{T} V_1(t) V_2^{\star}(t-\tau) dt, \tag{2.1}$$

where t is the time of arrival of the signal in antenna 1, while τ is the time delay caused by the lag in time of signal arrives at antenna 2.

$$\tau = \frac{\psi}{2\pi\nu} \tag{2.2}$$

where ψ is the fringe phase.

The area four basic observables which can be derived from a VLBI data and they are fringe frequency, fringe amplitude, fringe phase and group delay. Fringe frequency (F_ν) explains the time variation of fringe phase. It is given by the derivative of fringe phase with respect to time.

$$2\pi F_\nu = \frac{d\psi}{dt}. \tag{2.3}$$

Fringe frequency (F_ν) contains the source position information and is important for astrometric studies.

Fringe amplitude is important in estimating the source intensity, it does not contain any source position information and thus not used in astrometric studies. It can be derived from the cross correlation function simply by integrating it.

Fringe phase (ψ) expressed as $2\pi\nu\tau$, can also be derived from the cross correlation function. It is directly dependent on the angular frequency (ν) and delay (τ), with the range ($0 < \nu\tau < 1$), therefore the fringe phase range is $0 < \psi < 2\pi$. It contains astrometric information of the target source and absolute position determination would be inaccurate without the fringe phase.

Group delay (τ_g) is the phase gradient of the cross correlation spectrum with respect to the observing frequency band and can be expressed as;

$$\tau_g = \frac{1}{2\pi} \frac{d\psi}{d\nu} \tag{2.4}$$

2.3 Data Reduction Procedures

The description that follows of VLBI data reduction procedures, assumes that the correlation process had already been done, in the case of VERA correlation with Mitaka FX correlator completed. So starting with the correlated data and the fundamental calibration files, the rest of the processes are described in principle. The tasks and nomenclatures used in the description below applies with AIPS, but in principle applies to all interferometric data reduction (run with a different task name in other reduction packages like CASA, MIRIAD, difmap).

2.3.1 Loading and Editing the Data

After the correlation of a VLBI observation, loading (into the data reduction package, in most cases the Astronomical Image Processing System) and editing of the resultant data which is usually in flexible image transport system (FITS) format is the first step in reducing VLBI data to a meaningful and interpretable images, sensible enough to have significant scientific impact. The VLBI FITS data files are usually multi-source, multi-scan data files, and in the case of VERA contains the TY and GC extension tables. FITLD (fit load) is the AIPS task used for loading the data into AIPS and can be flexibly used for a number of purposes. For example, by adjusting the FITLD adverb (command for adjusting the parameters of an AIPS task) DOCONCAT to 1 (which comes with -1 as the default) one can concatenate two FITS data into one. Activating auto-correction adverb is also useful for automatically correcting correlation defects in the data. This is slightly a different procedure in the data obtained in the dual-beam mode (DIR2000) of VERA, in which case, one would need to use AIPS task AVSPC to average the spectral channel to be in harmony with the second to which it is to be glued to. To glues the two data sets together in common spectral channel, AIPS task VBGLV is used.

It is beneficial to inspect the loaded data and confirm that it is in the right order before proceeding with the rest of the data reduction steps. In AIPS, there a couple of text-based and plot-based tasks for data inspection. The text-based inspection tasks are IMHEAD, LISTR, UVPRT, DTSUM, while the plot-based are UVPLT, VPLOT, POSSM, FRPLT (see the AIPS cookbook for details of these inspection tasks).

After thoroughly inspecting the data, bad data points can be flagged or edited. Tasks TVFLG and IBLED can be used for flagging bad visibilities. These tasks are easy-to-use, interactive tasks with TV display of the visibilities. TVFLG is most commonly used, as it offers multi-baseline display and editing, while IBLED can only be done one baseline at a time. After flagging and editing, if necessary, it is vital to run task MSORT. This task sorts the (u, v) data sets into time and baseline, and also creates the NX and the CL (1) extension tables. For VERA data the accumulation time needs to be set as 1 second, same as adopted during the data correlation at Mitaka FX correlator. After this the data sets are ready for the calibration phase.

2.3.2 Amplitude Calibration

Amplitude calibration is important for obtaining the flux densities of the detected emission. Generally, in AIPS such process is executed with the task APCAL. In the case of JVN and VERA data, it is necessary to run the task ACCOR for the calibration of the correlation sampling bias. Normally, correlation coefficients should be normalized in the correlation output, but in the case of the Mitaka FX correlator, the correlation coefficient is 3 - 4 times larger than the normalized coefficient. Thus, the need to run ACCOR with solution integration time (SOLINT adverb) of 10 to 30 minutes.

2.3.3 Bandpass Calibration

In AIPS, BPASS task is used for computing the bandpass calibration of a VLBI autocorrelation and cross-power data. There are two options in computing the bandpass response using the BPASS AIPS task. The first is to perform the general computation of the amplitude response from the autocorrelation data, setting the phase response to zero. The second method decomposes the cross-power functions of the baseline into antenna-based complex bandpass response. Bandpass response is usually computed on channel by channel basis. Scans of the calibrators (continuum emission sources) are defined with the adverb CALSOUR, while the SOLINT is set as -1 in order to obtain one solution for the whole observation. AIPS task CPASS can also be used to solve the bandpass response and compute the calibration, but in a different way compared to the BPASS task (see AIPS cookbook for details). At the end of a successful run of the BPASS or CPASS task, a bandpass (BP) extension table is created.

2.3.4 Doppler Velocity Correction

Rotation and revolution of the Earth, as well as the motion of the Sun in the Milky Way introduce a Doppler shift in the desired velocity. This velocity is expressed as center frequency of a spectral line VLBI observation. Real-time velocity tracking is not available in present VLBI systems including VERA, therefore the individual stations move along the line of sight of the target source making the spectra to meander with time within the bandpass. In the case of VERA, there is also the contribution of the motion of the continental plate, sometimes caused by the effect of earthquakes. Thus the accurate positions of the antenna need to be calibrated first using a model created by the VERA group in NAOJ, whereas in the case of VLBA, the correlator rotates all the antenna phases to the same point, thereby removing the effects of the motion of the stations due to the rotation of Earth. And the remainder of the time-dependent residual of velocity shifts can be removed with the AIPS task CVEL. In the case of VERA, a trial velocity tracking is required before one can fully correct for the Doppler shift. Thus, CVEL has to be done at least twice for VERA data.

2.3.5 Phase & Delay Calibration

Phase calibration involves the determination and removal of the residual effects on phase portion of the complex antenna gain due to instrumentation and propagation through the ionosphere. Continuum sources observed between the scans of the target source can be used to monitor the clock parameters, thus useful for correcting the residual delays and delays due to individual antennas. Residual group delays (residual of the derivative of the fringe phase with respect to the observed angular frequency) appears as phase slopes in the frequency domain. Fringe-fitting can be used to determine the residual delays and fringe-rates and thus coherent averaging of the data becomes possible. The fringe-fitting of the continuum calibrator can be done with the AIPS task FRING. This task (FRING) produces a solution table which can be examined and applied to the spectral line (maser) data set.

2.3.6 Self-Calibration

Self-calibration of masers is a data reduction technique which can be applied in order to detect weak maser emissions that would ordinarily not be detected. This involves

the selection of a spectra channel containing the brightest, most stable maser emission. Fringe fitting of the single-channel maser emission is carried out with the AIPS task 'FRING' and using the adverbs 'BCHAN' and 'ECHAN' to be the same value which is equal to the bright maser emission channel number. It is important to bear in mind that the 'BIF' and 'EIF' adverbs are not tampered with in this task. The reason is to retain the same number of IF channels in the solution table (SN) newly created during the 'FRING' task as that of the AIPS UV data. Of course, the obtained solution table is applied to the entire single source maser data, thus the need to remain the IF channels as they were, without modifications. Furthermore, using the AIPS task 'SPLIT', 3 or 4 channels on the both sides of the selected channel with the bright maser emission is cut out of the rest of the data for iterative generation of the solutions to be used for the self-calibration of the entire single-source data. The tasks 'MULTI' and 'INDXR' are carried out on the SPLIT data. IMAGR task is then used to to make a dirty image map of the bright maser feature, using a CLEAN box on the bright emission, the map is CLEANed. Subsequently, the task 'CALIB' is used to apply the solution of the CLEANed image to the SPLITed, MULTI data and this generates a solution table which is then applied and imaged again. This process is repeated, iteratively until the dynamic range (the ratio of peak of the emission to the rms noise) of the emission reaches its peak. At this point, multiple SN tables are already generated and these are copied to the single source data (usually the CVEL file) containing all the spectra channels. And then the SN tables are applied using the task CLCAL, completing the self-calibration procedure.

2.3.7 Imaging

Fundamentally, the making of image cubes of maser sources can be done with either self-calibrated data or a position referenced calibrated data. In the case of self-calibrated data, the image cube usually have the coordinated in OFFSETs (x-offset, y-offset). This implies that the position of other maser features in the source is obtained with respect to the bright maser feature (represented by the maser spot which appears at the origin of the maser map) used for the self-calibration procedure. In self-calibrated data, absolute positions of the maser features cannot be determined, only their positions relative to the bight maser spot can be derived. On the other hand, the absolute positions of

the maser features obtained in a position-referenced calibrated data (calibrated with a bright quasar) can be derived.

IMAGR is the task used for making the wide-field image map and the tasks below are useful. IMSTAT to find a rms noise level for each of velocity channels. BLANK to set intensities of pixels without true maser emission to zero. At this stage, image files for the individual velocity channels are obtained. SUMIM to sum image files for the individual velocity channels into one map.

In order to obtain the vital information of the maser spots, Gaussian fitting is carried out. This could be done with the AIPS task JMFIT. The large number of maser spots obtainable in star-forming regions make this task a time-consuming process. Alternatively, the AIPS task SAD (Search And Destroy) can automatically perform the identification of the Gaussian components and their fittings. This could also be done using the AIPS POPS 'MMAP' developed by Hiroshi Imai.

2.4 Inverse Phase Referencing Technique

Obtaining the absolute positions of maser features is very important for comparative study of masers activities and other observational results of the same source at different wavelength. This affords us the opportunity to superimpose maps (masers and continuum emission maps e.g. Chibueze et al. 2012). Sadly, sometimes the position-reference source (quasar) is too weak to be detected in a normal phase-referencing calibration procedure. Hence, the need for a special technique to be able to detect the weak calibrator and thus derive the absolute positions of the masers feature.

This technique involves standard calibrations on both the maser and the position reference source, followed by the task 'FRING' with the advert 'CALSOUR' specified as the other calibrators apart from the position reference source. The 'FRING' solution is then applied to the maser source data, and self-calibration is carried out after that. The solutions obtained from the maser self-calibration procedure is applied to the SPLITed, MULTI data of the position reference source. Then IMAGR task is used to image the source and the offset positions shifted back to origin while the offset values are used to recalculate the maser positions to derive their absolute positions. This procedure has been applied independently to measure the annual parallax of a late-type star (see Imai et al. 2012) and Figure 2.1 shows the flow chart of the data reduction procedure.

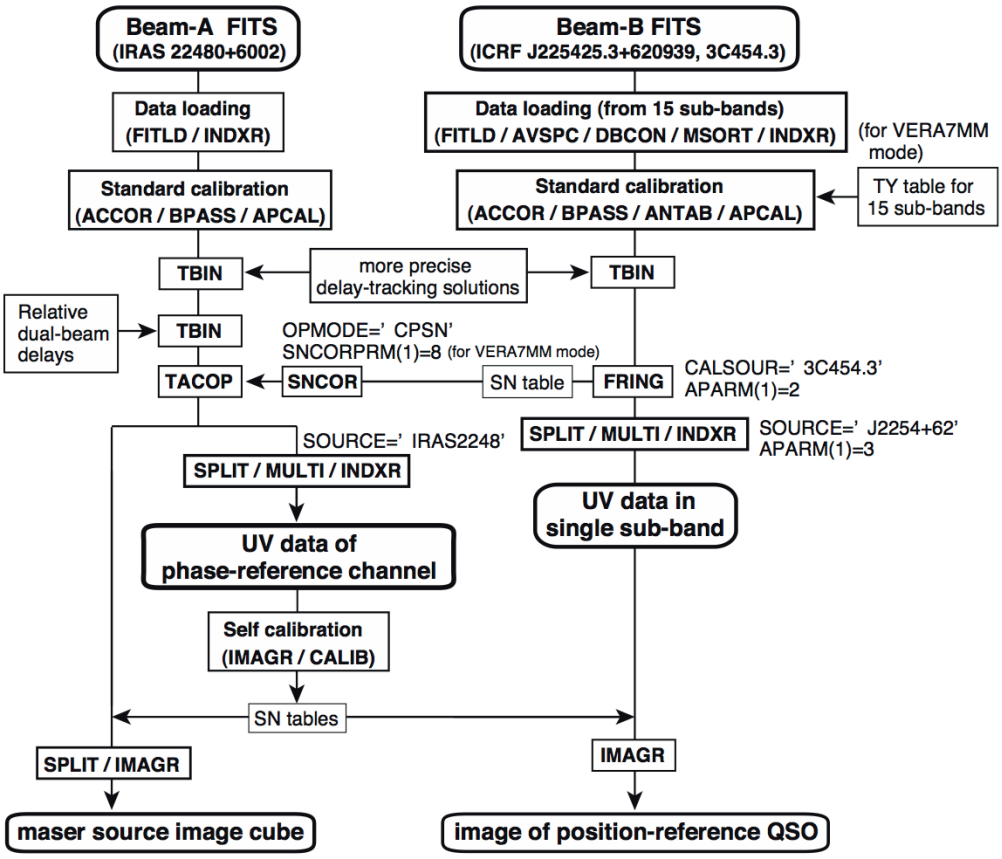

Figure 2.1: Flow chart of a inverse phase referencing steps - The flow chart of a successful data reduction procedure which applied inverse phase referencing technique in annual parallax method (adopted from Imai et al. 2012).

3

A Highly Collimated Water Maser Bipolar Outflow in the Cepheus A HW3d Massive Young Stellar Object

Adapted from Chibueze et al., 2012, ApJ, 748, 146

3.1 Introduction

The last decade has seen a lot of efforts toward understanding how massive stars form and evolve. The fact that massive stars have a very significant impact on the evolution of the interstellar medium of galaxies, with strong influences in their environments (through strong winds, expanding HII regions, UV radiation, supernova explosions), and sometimes activating other star formation events, underscore the importance of this research. However, it is still among the most poorly understood topics in the field of astronomy. This is mainly because massive stars form in highly obscured mediums, thus, making it very difficult to observe them in their early phases. In addition, they evolve quickly (formation timescales of $\sim 10^5$ yr), and form in distant clusters and associations, therefore hard to isolate single high-mass stars for their study (see reviews by e.g., Hoare & Franco 2007; McKee & Ostriker 2007; Zinnecker & Yorke 2007). Based mostly on theoretical simulations, different attempts have been made in proposing

the formation scenarios of massive stars. There are mainly three proposed scenarios; massive star formation through the merging of less massive stars (Bonnell, Bate, & Zinnecker 1998), competitive accretion in a protocluster environment (Bonnell & Bate 2006), and gravitational collapse involving high-rate, disk-assisted accretion into the core which helps to overcome radiation pressure (Yorke & Sonnhalter 2002; McKee & Tan 2003; Krumholz et al. 2005, 2009).

With high brightness temperatures exceeding 10^{10} K and compact nature, H_2O masers have proven to be very useful in astrophysical studies using very long baseline interferometry (VLBI) with milliarcsecond (mas) angular resolution, particularly in identifying present sites of high-mass star formation in molecular clouds for studying the very vicinity of massive young stellar object (YSO) candidates (e.g., Genzel et al. 1981; Torrelles et al. 2001a, 2003; Imai et al. 2002; Goddi et al. 2005, 2006; Moscadelli et al. 2006;Vlemmings et al. 2006; Surcis et al. 2011). This chapter explores the results of nine epochs of H_2O maser observations toward the Cepheus A (Cep A) high-mass star-forming region using the VLBI Exploration of Radio Astrometry (VERA).

3.1.1 Accurate Distance to Cepheus A

The distance to Cep A is one of the most debated issue in the study of the famous galactic massive star-forming region. So far, a wide range of distance estimation has been made by different researchers using different methods. The estimates range from 300 pc reported by Migenes et al. (1992) to 900 pc reported by Moreno-Corral et al. (1993). While Migenes and collaborators used the hydroxyl (OH) maser proper motions observed with the multi-element radio-linked interferometer network (MERLIN), Moreno-Corral and collaborators applied the photometric method in their distance estimation. The mostly cited of them all is Johnson (1957) estimate, which pegged the value at 725 pc.

VLBI measurement of annual trigonometric parallax remains the most accurate means of obtaining the distance to star-forming regions. This requires determining the absolute positions of the same maser feature consistently at different times of a year and obtaining the parallax by trigonometric fitting. Moscadelli et al. (2009) conducted multi-epoch methanol maser observations of toward HW 2 object of Cep A with very long baseline array (VLBA) and derived the trigonometric parallax to be 1.43 ± 0.08 mas corresponding to a distance of 700 ± 40 pc. Similarly, using the VLBA detected

strong variability on in radio continuum emission in the HW9 in a 10-epoch observation, Dzib et al. (2011) obtained the trigonometric parallax to be 1.43 ± 0.07 mas (distance of 700^{+31}_{-28} pc) improving the uncertainty to about 3.5%.

In this work, the distance to Cep A was adopted to be ∼ 700 pc (Moscadelli et al. 2009, Dzib et al. 2011).

3.1.2 Recent VLBI Results on Cepheus A

Cep A is probably among the mostly studied massive star-forming (MSF) region in the Milky Way, and the second nearest MSF region after Orion. It provides a good 'laboratory' for the study of massive star formation processes. Cep A is the densest component of the molecular cloud complex Cepheus OB3 (Sargent 1977). There are two main regions of ionized gas in Cepheus A, namely; Cep A East and Cep A West both separated by a distance of approximately 1′.5 (Hughes & Waterloot 1982; Rodriguez & Canto 1983). Hughes et al. identified 16 high density compact radio sources in an approximately 25″ radius region, centered around H_2O maser activity. Garay et al. 1996 argued the existence of two types of radio sources in the Cep A East region namely; internally excited and externally excited objects. Based of their classification, objects 2, 3a, 3c, 3d, 8, and 9 are radio sources showing some indications of having an internal exciting source within them. Among these indications are the presence of H_2O and OH masers in objects 2, 3a, 3d (Lada et al. 1981; Cohen et al. 1984), positive spectral indices of objects 2, 3c, 3d (Garay et al. 1996), large variability in flux densities of objects 3a, 8, 9 (Hughes 1988, 1991; Garay et al. 1996) and the association of infrared (IR) point sources with object 3a (Lenzen 1988).

Objects 1a, 1b, 4, 5, 6, 7a, 7b, 7c, and 7d were classified as objects excited by an external source of energy. Among the distinguishing characteristics are exhibition of extended halos of diffused emission, a string-like pattern, and the location along the edges of the dense ammonia condensations reported by Torrelles et al. 1993. Garay and collaborators found the string sources to show a mixture of positive, flat and negative spectral indices across their faces, thus suggesting that both thermal emissions and non-thermal emissions arise from the string. This is a phenomenon peculiar to shock wave front moving through a magnetized medium, in which part of the electrons are relativistically accelerated giving rise to non-thermal synchrotron emission and the majority of the electrons with thermal velocity distribution will give out the thermal

free-free emission (Henriksen, Ptuskin & Mirabel 1991). Important of note is Hughes et al. 1995 suggestion that the source 3dii contains a star that is undergoing mass loss.

Torrelles et al. (2011) is currently the most recent VLBI H_2O kinematic study towards Cep A. They reported a 0.4-mas (0.3 AU) resolution multi-epoch H_2O maser observations with VLA and VLBA. The results show the morphological changes in the R4 and R5 maser clusters at scales of $\sim 0.1''$ (70 AU) in 5 years. Particularly, the R5 expanding bubble structure observed 5 years before, located $\sim 0.6''$ (400 AU) south of HW2, is currently dissipating in the circumstellar medium, losing its previous degree of symmetry, thus corroborating the very short-lived nature of this phenomenon (see Figure 3.1). On the other hand, the masers of the R4 structure trace a nearly elliptical patchy expanding ring of ~ 70 mas size (50 AU), supporting the ring scenario proposed previously by Gallimore et al. (2003), rather than the bow-shock scenario proposed by Torrelles et al. (2001) (see Figure 3.2). They suggested a central YSO to be driving the observed expanding motions of the ring, this YSO is a still unidentified (probably a massive object given the high luminosity of the associated water masers), and should be located $\sim 0.2''$ (145 AU) south of HW2. Their results also reveal a relatively slow wide-angle outflow (opening angle $\sim$102°) with the simultaneous presence of the high-velocity ionized jet (opening angle$\sim$18°) associated with HW2. The presence of high-velocity jets, enclosed within wide-angle outflows, has been observed in low-mass protostars. The importance of our result is that this is now observed in a massive protostar, with the highly collimated and wide-angle outflow in HW2 occurring simultaneously at a similar physical scale of $\sim 1''$ (700 AU) (see Figure 3.3).

We focus mainly on HW3d in Cep A, one of the 16 radio continuum objects discovered by Hughes & Wouterloot (1984), and located $\sim 3''$ south from the brightest radio continuum source in the region, HW2. HW2 clearly harbors a massive YSO in it, which is indicated by the observations of a jet and a disk, intense magnetic fields, and powerful H_2O masers (Rodríguez et al. 1994; Patel et al. 2005; Curiel et al. 2006; Jiménez-Serra et al. 2007; Torrelles et al. 2007, 2011; Vlemmings et al. 2010). On the other hand, the observational properties are not so clear in the case of the other HW objects. In fact, Garay et al. (1996), through multifrequency Very Large Array (VLA) radio continuum observations, argued that some of the HW objects are internally excited by a YSO, while others are externally shock-excited at the interface between winds of other YSOs and molecular clumps in the region. HW3d is one of the

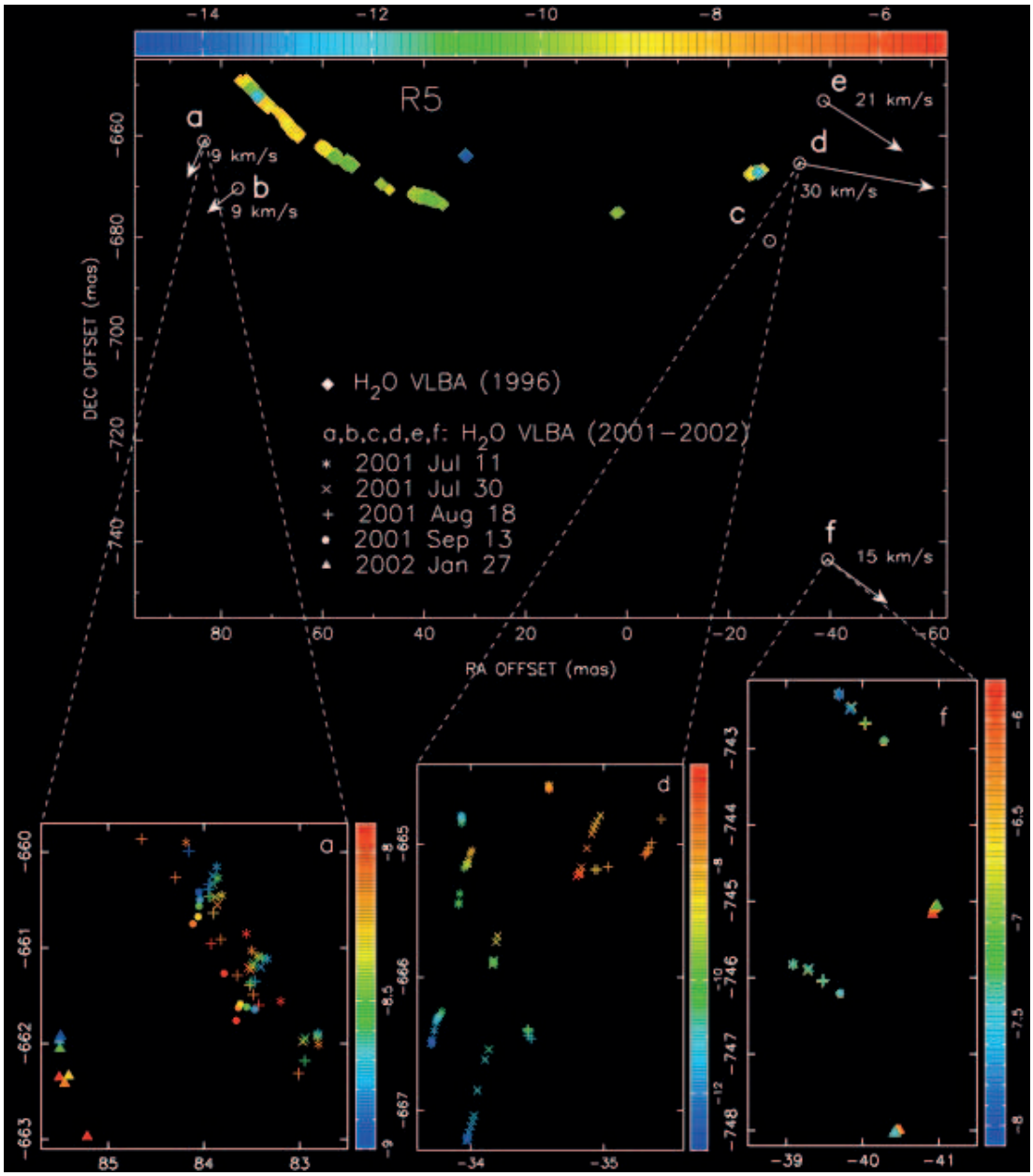

Figure 3.1: Cep A HW2 R5 H_2O Masers - Expanding bubble structure of the H_2O maser features in R5 and the traced proper motions from a, b, c, d, e, and f features based on the VLBA observations. The color codes and bar represent the LSR velocities of the different maser features. R5 has known exciting massive star (Torrelles et al. 2011).

3. A HIGHLY COLLIMATED WATER MASER BIPOLAR OUTFLOW IN THE CEPHEUS A HW3D MASSIVE YOUNG STELLAR OBJECT

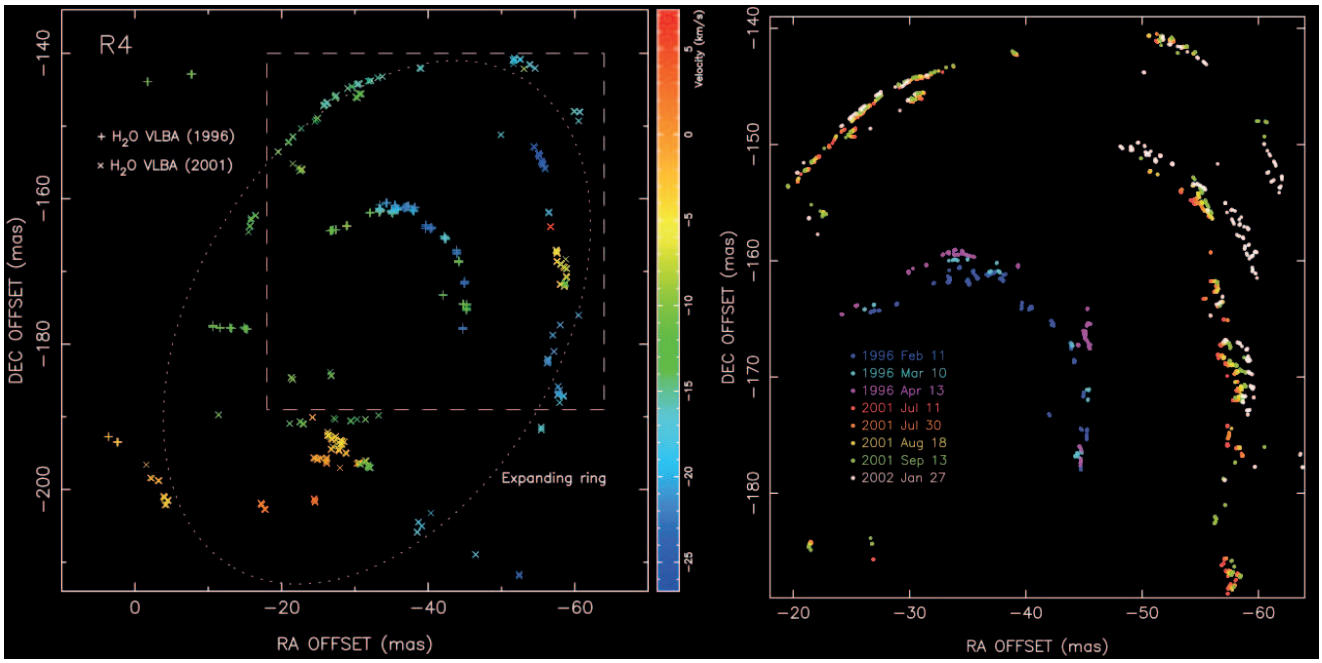

Figure 3.2: Cep A HW2 R4 H_2O Masers - Ring structure of the H_2O maser features in R4. The color codes and bar represent the LSR velocities of the different maser features. The massive star HW2 is not responsible for the observed violent ejection traced in the expanding ring structure, and the exciting star of this maser activity is yet to be identified (Torrelles et al. 2011).

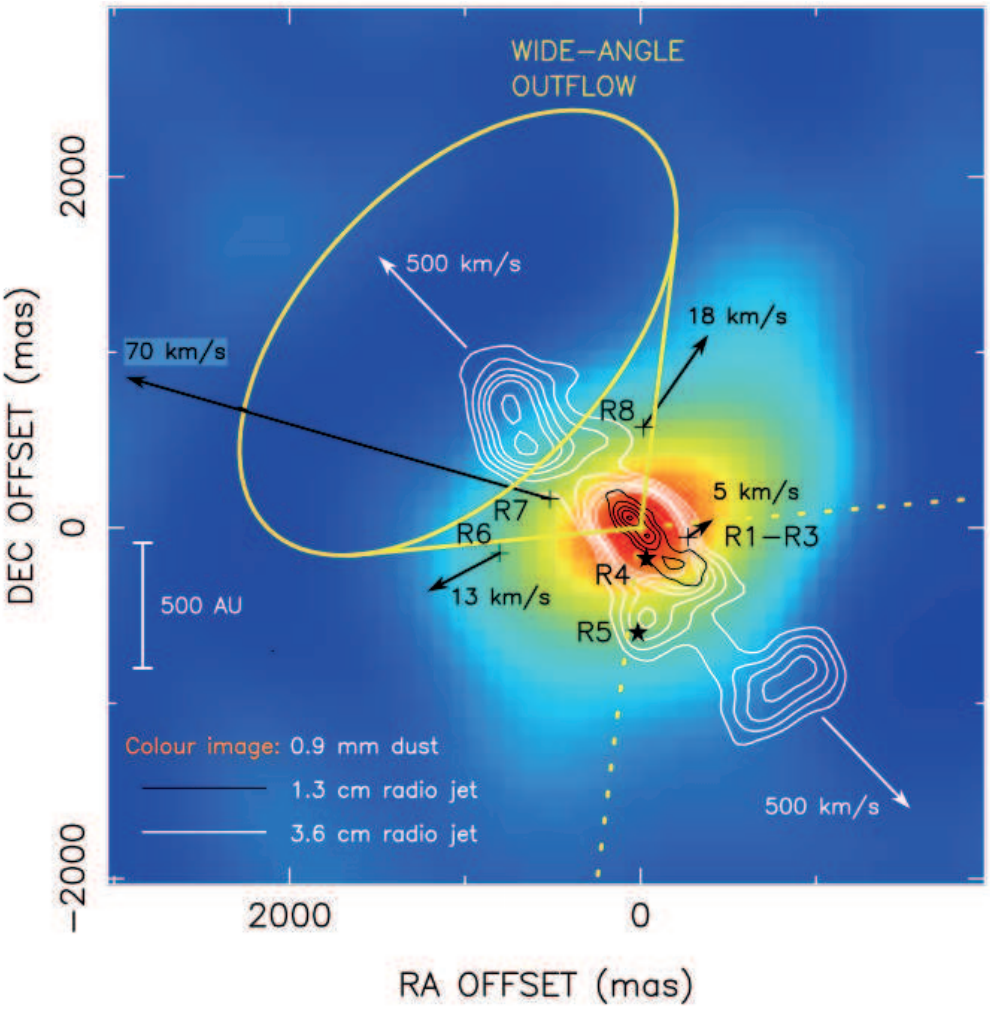

Figure 3.3: Cep A HW2 wide-angle outflow - Wide-angle outflow of HW2 traced by H_2O masers. They obtained an opening angle of 102° for the wide-angle outflow based on the proper motions of the H_2O masers in R6, R7, and R8 (Torrelles et al. 2011).

objects that was proposed to be excited internally by its own YSO, on the basis that the radio continuum emission presents an elongated structure with positive spectral index, which is suggestive of a thermal jet nature. Hughes, Cohen, & Garrington (1995) also supported it on the basis of its association with strong hydroxyl (OH) and H_2O maser emission (Cohen et al. 1984), although they did not find evidence for outflow activity in this object. The evidence for outflow activity is now presented in this paper through our VERA H_2O maser observations, giving a conclusive support that the HW3d object is internally excited by a massive YSO.

3.1.3 Goals of the Study

Is HW3d tracing the path of the more evolved HW2 counterpart? Does it have a driving source as its positive spectral index suggests? If so can we find any evidence for the presence of a star? What useful information can we derive from the maser spatio-kinematics of HW3d? And how does that add to the composite picture of the evolutionary sequence of massive stars? By means of this study we explore the answers to the above questions to the extent possible within the limits of the available data and information.

The basic goal is to trace the proper motions of the H_2O masers in HW3d in a multi-epoch observations and then study the structure of the traced motions in order to understand the star formation activities prevalent in the object. The dynamical time scales of the different, known maser activities like violent ejections, outflows, are useful for identifying the different evolutionary stages of high-mass stars. Using the existing pieces of information on the dynamical timescale of maser activities in massive star-forming region, we attempt to build a description of the evolutionary sequence of massive stars.

3.2 Observations and Data Reduction

The VLBI observations used for this study were made with the VERA and VLA. In subsections 3.2.1 and 3.2.2, we will describe the details of these observations and the data reduction procedures.

3.2.1 VERA Multi-epoch Observations of Cep A

The observations of the Cep A H_2O masers at 22.235080 GHz with VERA (see Figure 3.4) were carried out in 9 epochs from 2006 May to 2007 August. Table 3.1 gives a summary of these observations. At each epoch, the total observation time was about 8 hours, including the scans on the calibrators (J2005+7752, BL Lac, J2015+3710). Using the advantage of the VERA's dual-beam system, Cep A and J2302+6405 (a position reference source spatially separated by 2.19° from Cep A) were simultaneously observed with the aim of determining the annual parallax of Cep A. The result of the measurement of the parallax distance would be published in a separate paper. The received signals were digitized in four quantization levels, and then divided into 16 base-band channels (BBCs) in a digital filter unit, each of which had a bandwidth of 16 MHz, corresponding to a velocity coverage of 216 km s^{-1} centered around 50 km s^{-1} with respect to the local standard of rest (LSR). One of the BBCs was assigned to the frequency of the H_2O maser emission in Cep A while the other 15 BBCs were assigned to the continuum emission from J2303+6405 and other sources observed in the B-beam of the VERA system.

Code	Epoch	Noise [Jy beam^{-1}]	Beam [mas, °]	Duration (Hr)
r06133b	2006 May 13	0.12	1.49×0.87 , −38.8	8
r06208an	2006 July 27	0.40	1.38×0.91 , −2.9	8
r06291a	2006 October 18	0.58	1.79×0.85 , −40.7	11
r06310a	2006 November 6	0.03	1.79×0.84 , −37.9	11
r07004a	2007 January 4	0.06	1.57×0.76 , −61.6	11
r07049a	2007 February 18	0.09	1.57×0.86 , −51.9	11
r07103a	2007 April 13	0.09	1.64×0.96 , −51.4	11
r07135a	2007 May 15	0.10	1.46×0.94 , −66.0	11
r07243a	2007 August 31	0.06	1.84×0.81 , −82.9	11

Table 3.1: VERA observations of Cepheus A. - VERA observations of Cepheus A. All the VERA telescope stations (Mizusawa, Iriki, Ogasawara, and Ishigakijima) participated in every epoch of the observations. Beam refers to the synthesized beam size resulting from naturally weighted visibilities; major and minor axis lengths and position angle, while noise is the typical noise per spectral channel.

The data correlation was made with the Mitaka FX correlator. The accumulation

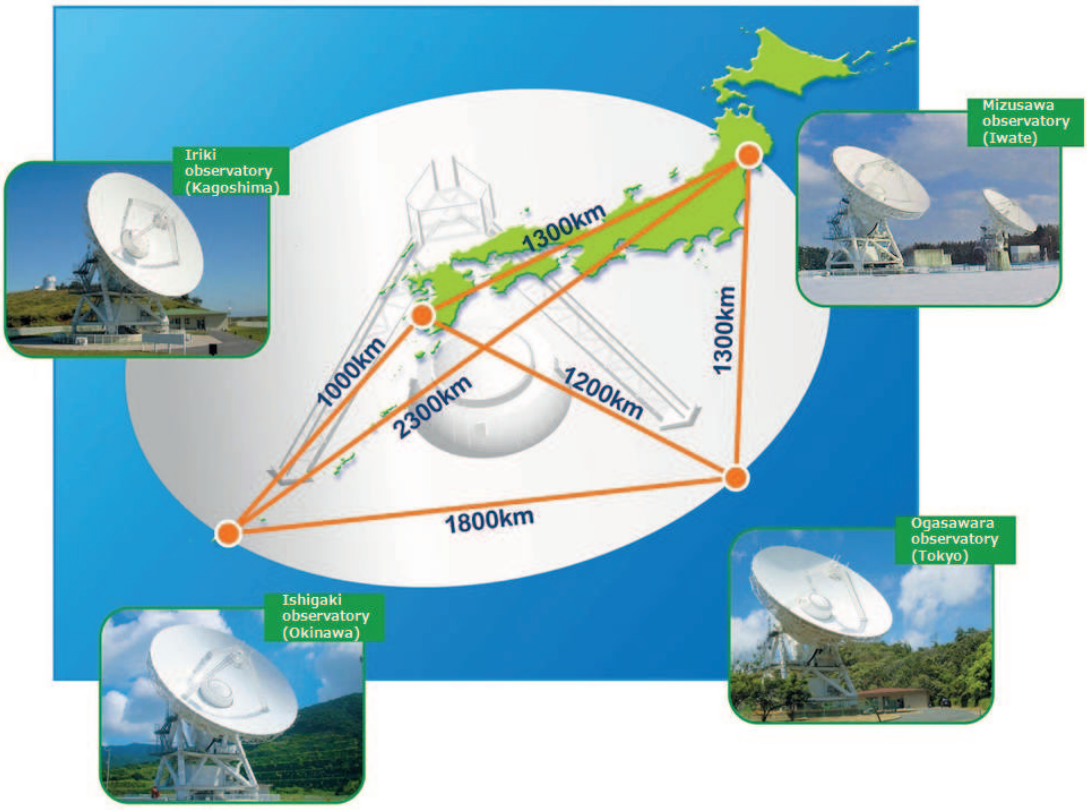

Figure 3.4: VERA Array - VERA array showing the location of the four 20 m telescopes with a synthesized beam of $\sim$ 2300 km.

period of the correlation was set to 1 second. The correlation outputs consisted of 512 and 64 spectral channels for the H_2O maser and reference continuum emission, respectively. A velocity spacing of 0.21 km s^{-1} was obtained in each spectral channel for the H_2O maser emission.

The data reduction was made with the National Radio Astronomy Observatory (NRAO) Astronomical Image Processing System (AIPS) package using standard procedures. The instrumental delay calibration was made with the scans on the calibrators. The fringe fitting and self-calibration procedures were performed for a Doppler velocity channel including a bright maser spot (velocity component) in the HW3d region of Cep A. Their solutions were applied to all the data and then the map of the maser clusters were made. The CLEANed image cubes of the maser source were created using the beam that was synthesized from naturally weighted visibilities. The typical size of the synthesized beam was $\sim$ 1.3 mas. The H_2O maser image cubes were made with a cell size of 0.2 mas.

Because we carried out self-calibration procedure using a bright maser spot in the HW3d region, the maser spot positions in the image cubes were measured with respect to the bright maser spot used for self-calibration mentioned above. For the wide-field mapping and objective maser spot identification, we used an automatic pipeline script which runs on the AIPS POPS environment and mainly consists of AIPS tasks and adverbs: IMAGR, IMSTAT, and SAD. The H_2O maser feature identification was done by adopting a signal-to-noise ratio cut-off of $\sim$ 8. From the Gaussian fitting errors, we estimated the accuracies of the relative positions of the maser spots to be 0.01 – 0.20 mas in Right Ascension and 0.02 – 0.30 mas in declination. The individual maser features were defined as clusters of maser spots or velocity components and each feature position was defined from the brightness peak of the feature following the identification method of Imai et al. (2002).

We adopted special procedures (inverse phase referencing, see Section 2.4) to measure the absolute coordinates of the detected H_2O masers. This enables a comparative study with the 1.3 cm continuum emission map from VLA observations described in §3.2.2. The position-reference source J2303+6405 observed concurrently in the B-beam of the VERA system was not detected by applying the normal fringe fitting. To detect the weak emission of the position-reference source and thus measure the coordinates of

the maser features with respect to it, we applied the inverse phase-referencing technique. This procedure involves common calibrating the group delay residuals of the A- and B-beam data using the data of the bright continuum calibrators (BL Lac, J2005+7752) observed in the B-beam. Then we did fringe fitting and self-calibration as described above using a bright maser velocity component. Subsequently, we applied all the phase calibration solutions obtained to the position-reference source (J2303+6405) data. We successfully carried out this procedure in the observation epoch of February 18, 2007, using a bright maser spot at $V_{LSR} = -6.67$ km s^{-1} near HW2 and detected the position-reference source (30 mJy/beam) at a position offset of 15.4 mas in R.A. and 606.5 mas in declination from the J2303+6405 map center. This inversely indicates the position offset of the phase-reference maser spot from the delay-tracking center. We determined the absolute coordinates of the position-reference maser spot (maser spot used for the AIPS self-calibration procedure) to be RA(J2000) = $22^h56^m17.97745^s$ DEC(J2000) = $+62°01'49.3784''$ by computing the negative of the offset of the position-reference source (J2303+6405) from the map origin.

There was no maser feature consistently identified in all the epochs which could be used as a reference position, therefore we adopted the following method to trace individual maser features at as many successive epochs as possible. Firstly, from any two adjacent epochs, we calculated the mean coordinate offset of the maser features at the second epoch with respect to that at the first epoch using only the maser features that were detected at both epochs. Secondly, these mean offsets were referred with respect to the earliest epoch taken on May 13, 2006. Then, these offsets were subtracted from the coordinates originally used in the individual epochs (see Torrelles et al. 2001b). In so doing we were able to register all maser feature maps and obtain a reference frame whose spatial stability at all epochs depends on that of the maser feature distribution. The map origin of the reference frame is very close to a quasi-stationary maser feature in HW3d (Feature 15 in Table 3.2). We tested the stability of the reference position offset using the Feature 15 (seen at the same position within 1 mas and at the same LSR velocity; see Appendix) identified at 5 epochs. The residual proper motion in the reference frame is $\mu_x \sim 0.001$ (mas yr^{-1}) and $\mu_y \sim 0.003$ (mas yr^{-1}), and the standard deviation of the offset coordinates of the maser feature is 0.02 mas in Right Ascension

and 0.05 mas in Declination. All maser offset positions in this paper are given with respect to the derived reference position offset.

3.2.2 VLA Archive Data

In order to compare the masers imaged from our VERA observations with the radio continuum emission of HW3d, we retrieved data from the VLA archive. We found a 1.3 cm continuum data set around the same epoch of the VERA observations under the project name AC0810, taken on 2006 February 11 in the most extended A configuration of the VLA at an observation frequency of $\sim$ 22.29 GHz. The data include the two circular polarizations with an effective bandwidth of 100 MHz. It is important to note that these continuum data do not overlap with the frequency of the H_2O masers, thus they are free of contamination from the line emission. The sources 1331+305 and 2230+697 were the flux density and phase calibrators, respectively. The calibration was carried out under standard procedures outlined in the chapter 4 of the AIPS cookbook. The assumed flux density for the amplitude calibrator was 2.59 Jy, while the estimated flux density of the phase calibrator was 0.51 Jy. The total time on source was $\sim$ 4 hours, which yielded an RMS noise in the final image of $\sim$ 52 μJy beam^{-1} using naturally weighted visibilities.

3.3 Results

3.3.1 Highly Collimated Bipolar Outflow of Cep A HW3d

Herein is a quick overview of the implication of the results presented in the (sub) sections that follows. The main success of this study is the confirmation of the presence of an internally exciting source in HW3d of Cep A. The evidence is found in the H_2O maser bipolar outflow detected with VERA with a collimation factor of 3, The H_2O maser outflow structure aligns well with the observed elongation of the VLA 1.3 cm continue emission from HW3d, with an opening angle of 30° (highly collimated). The maser positional distribution and the proper motion velocity dispersion analyzed with an objective tool reconfirms our results. An expanding model of the H_2O maser proper motions suggest that there might be more than one exciting sources present in HW3d.

3.3.2 Spatio-kinematics of H_2O Masers and the Morphology of the Radio Continuum Emission in HW3d

We detected H_2O maser clusters corresponding to all the sub-regions R1-R8 around HW2, previously reported by Torrelles et al. (2011), as well as maser clusters associated with HW3d. In this chapter, we will concentrate on the results obtained toward HW3d, presenting for the first time H_2O maser proper motion measurements in this object.

We have carried out careful registration and identification of the H_2O maser relative proper motions in the HW3d especially for the masers in the C cluster (see Figure 3.9). Maser features coincident in LSR velocity within 1 km s^{-1} and position offset within 2 mas between epochs were used in tracing the proper motions. A larger fraction of the proper motions were traced in 3 or more epochs, while some were traced in just 2 epochs. The proper motions traced in 2 epochs are either clearly isolated in LSR velocity or position or in both. This is to avoid any case of proper motion misidentification especially in the complex C maser cluster. Before arriving at the 30 H_2O maser proper motions, we have carefully dropped some maser proper motions with high identification uncertainties. The tracing of the relative proper motions is shown in Figure 3.10 - 3.12. A gradient is expected for the R.A. and Declination trace of the maser relative motions except for the reference maser feature (feature 15; see Table 3.2) which is quasi-stationary, but the LSR velocity is observed to remain constant. It can be observed that the LSR velocity was not actually constant in some of the proper motions. Some of the masers indicate LSR velocity drift, but in this paper we do not consider the possible acceleration of the H_2O masers.

Figure 3.6 show the traced proper motions using our VERA data. We would not be considering the maser activities in and around HW2 as they have been thoroughly treated by Torrelles et al. (2011).

The VLA 2006 data turned out to be very useful because they also allowed us to explore the variability of HW3d by comparing these observations with those of VLA 1995 reported in Torrelles et al. (1998). Figure 3.5 shows the VLA 1.3 cm continuum map obtained from the 2006 data, showing the HW2 radio jet, the HW3c and the HW3d objects, which are located $\sim 3''$ south from HW2, superimposed on the H_2O maser map obtained from our VERA observations. In what follows, we will concentrate on the HW3d object. The main properties of the HW2 thermal radio jet and the HW3c object can be found in Rodríguez et al. (1994) and Garay et al. (1996). Figure 3.7

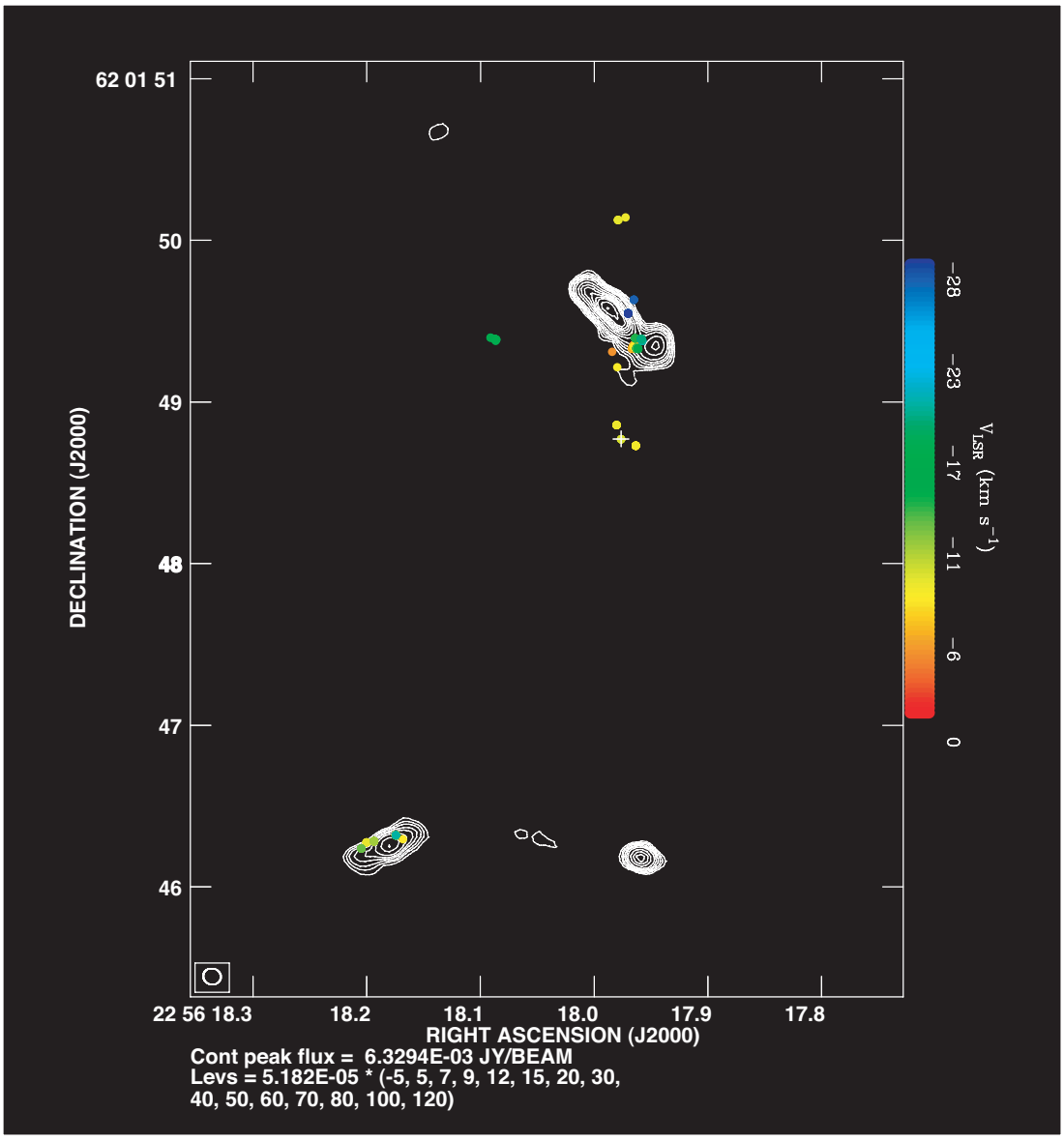

Figure 3.5: Cep A H_2O Masers & 1.3 cm VLA continuum - Distribution of the H_2O maser features detected in our VERA Observations superimposed on the VLA 1.3 cm continuum emissions observed in 2006. The color codes and bar represent the LSR velocities of the different maser features.

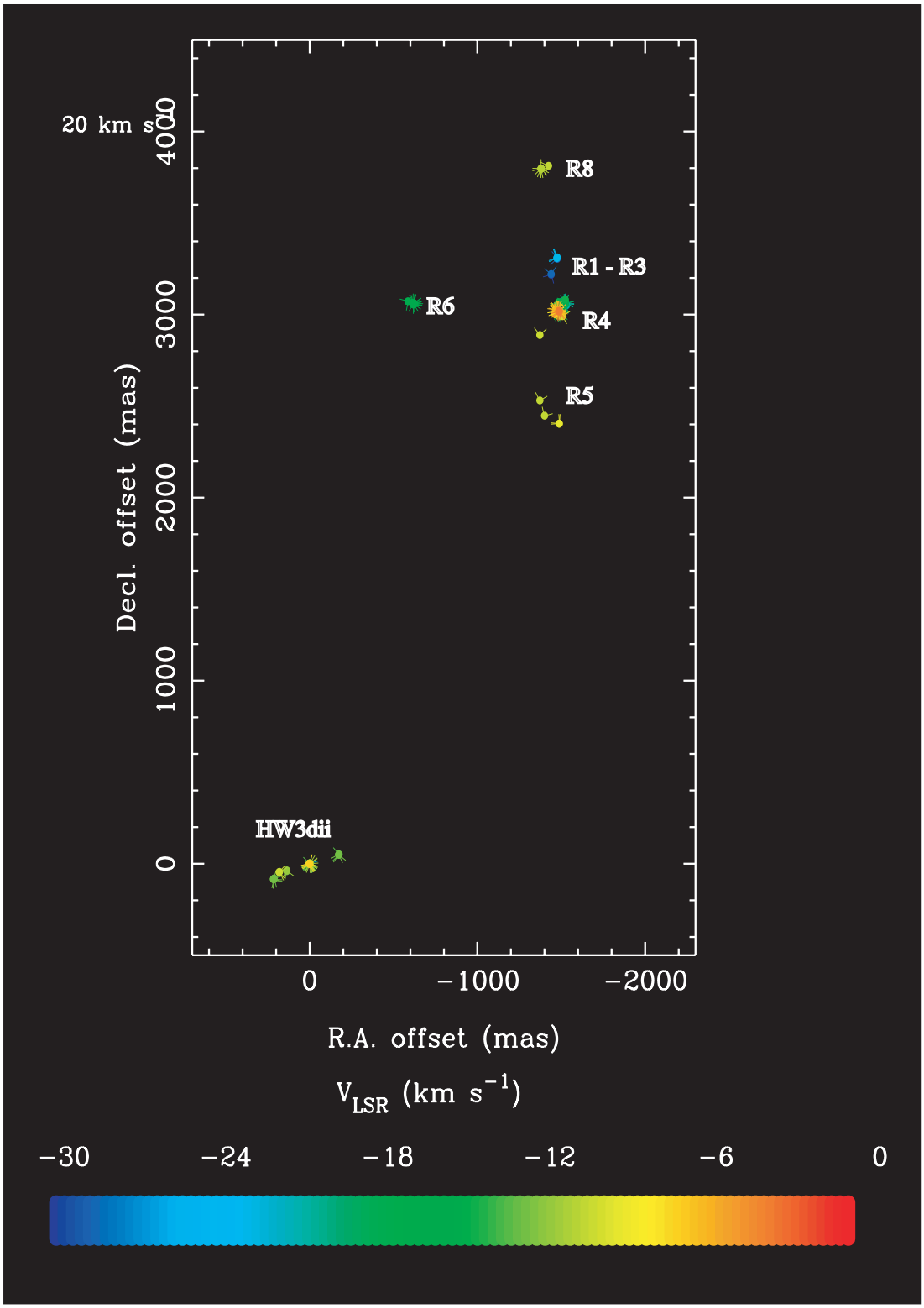

Figure 3.6: Cep A H_2O Maser Proper Motions - Distribution of the proper motions traced from the H_2O maser features detected in our VERA Observations. The color codes and bar represent the LSR velocities of the different maser features.

shows the difference in the peak position of HW3d between the 1995 and 2006 epochs of the VLA observation, while Figure 3.8 shows the clear evidence of the elongation of the continuum emission of HW3d between 1995 (orange contour) and 2006 (white contour), with its associated H_2O masers.

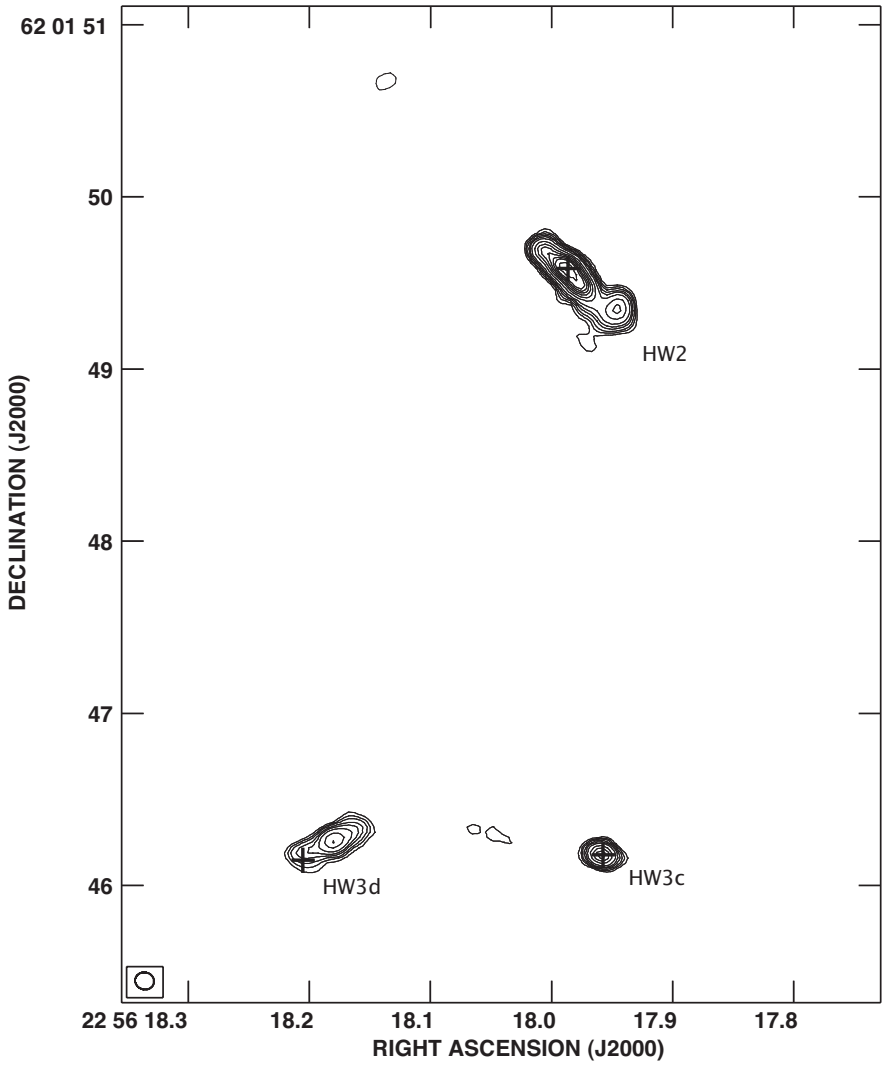

Figure 3.7: Cep A VLA 1.3cm continuum emissions map (peaks) - Cep A VLA 1.3cm continuum emissions of 2006 epoch. The cross sign on HW3d indicates the peak position of the compact continuum emission observed in the 1995 epoch.

Figure 3.9 shows the distribution and the relative proper motions of the H_2O maser features around HW3d superposed on the VLA 1.3 continuum map of this object. The accuracy in the absolute position of the maser feature estimated from the astrometric

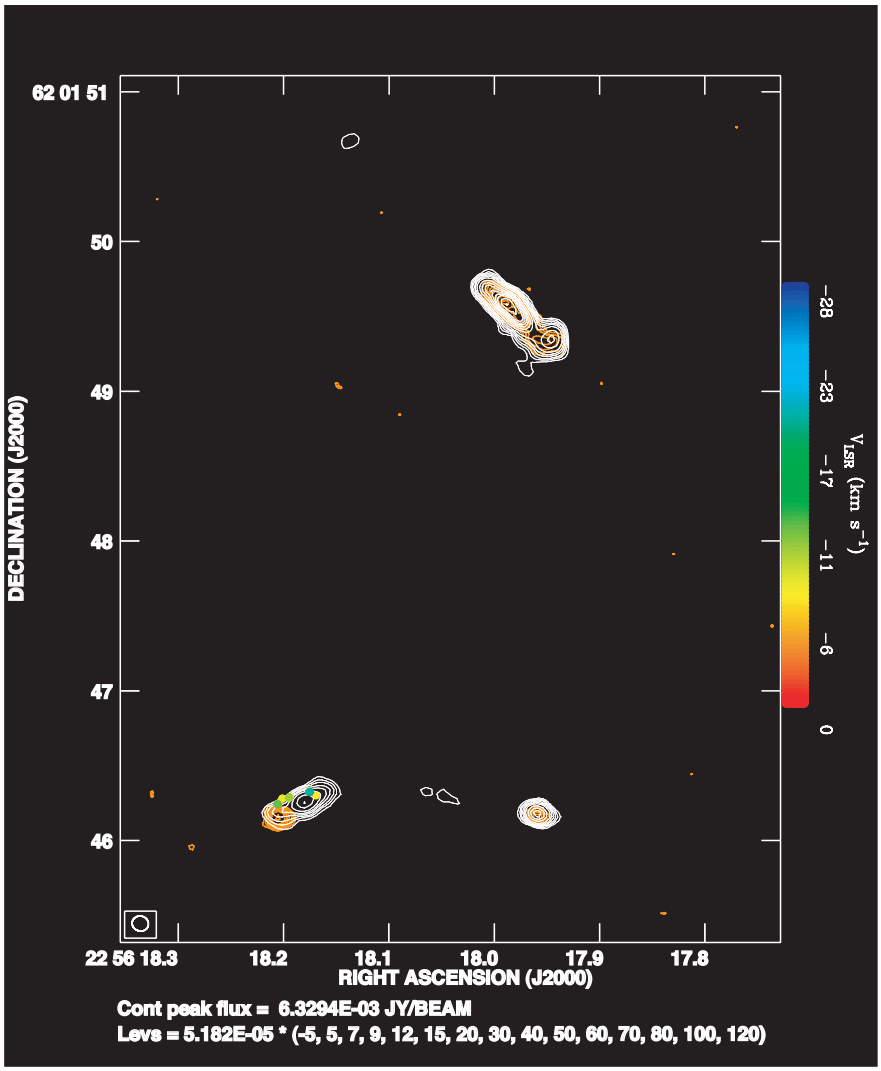

Figure 3.8: Cep A VLA 1.3cm continuum emissions map (contours) - Cep A VLA 1.3cm continuum emissions of 1995 epoch (orange contour) superimposed on the 2006 epoch (white contour), showing the change in the peak position of HW3d.

data analysis is better than 1 mas. On the other hand, the accuracy in the absolute position of the continuum emission observed with the VLA is estimated to be $\sim$ 50 mas. We find that the H_2O maser features are distributed on a linear structure of $\sim$ 400 mas (280 AU) in size, well aligned with the elongation direction of the radio continuum emission of HW3d ($\sim$ 500 mas in total length). Within this linear structure, we identify three main clusters of masers, one located at the center position (hereafter C cluster), and the other two in opposite direction with respect to the center, at $\sim$ (–170 mas, +40 mas) (hereafter NW cluster) and $\sim$ (+220 mas, –80 mas) (hereafter SE cluster), respectively. The maser proper motions of these three groups of masers indicate the presence of a bipolar outflow moving outward from the central positions along the major axis of the radio continuum emission. In fact, while the masers of the NW cluster are moving toward the northwest, those of the SE cluster are moving toward the southeast. These bipolar motions are also observed in the masers of the central cluster at scales of $\sim$ 4 mas (see Figure 3.9 and Table 3.2). Table 3.3 shows the detection or non-detection of each of the maser features in the various epochs of the VERA observations. The spatial distribution of the masers and the mean value of the proper motions without considering the turbulent central cluster ($\sim$ 6 mas/yr or $\sim$ 21 km s^{-1}) indicate that in HW3d there is a collimated bipolar outflow driven by an internal (probably) massive YSO that we propose to be located very close to the central position of cluster C. The fact that this cluster has the highest radial velocity dispersion ($\sim$ 20 km s^{-1}; Table 3.2) of all the observed maser clusters in HW3d, also supports this C cluster as the main center of activity containing a driving YSO. The estimated dynamical time-scale of this outflow is $\sim$ 100 years. The fact that the radio continuum emission of HW3d is elongated along the direction of the outflow masing motions suggests a radio jet nature for this object, supporting the interpretation given by Garay et al. (1996) based on spectral index measurements.

There is in addition a fourth group of masers located at $\sim$ (+135 mas, –39 mas), but their proper motions toward the north-west (see Figure 3.9 and Table 3.2) cannot be explained within a single bipolar outflow scenario excited by a single YSO close to the (0,0) position. The possibility of multiplicity of YSOs in this region is considered in §3.3.4. We estimated the opening angle of the outflow using the deconvolved size of the radio jet of HW3d ($\sim$ 325 $\times$ 99 mas), giving a value of $\sim$ 30°.

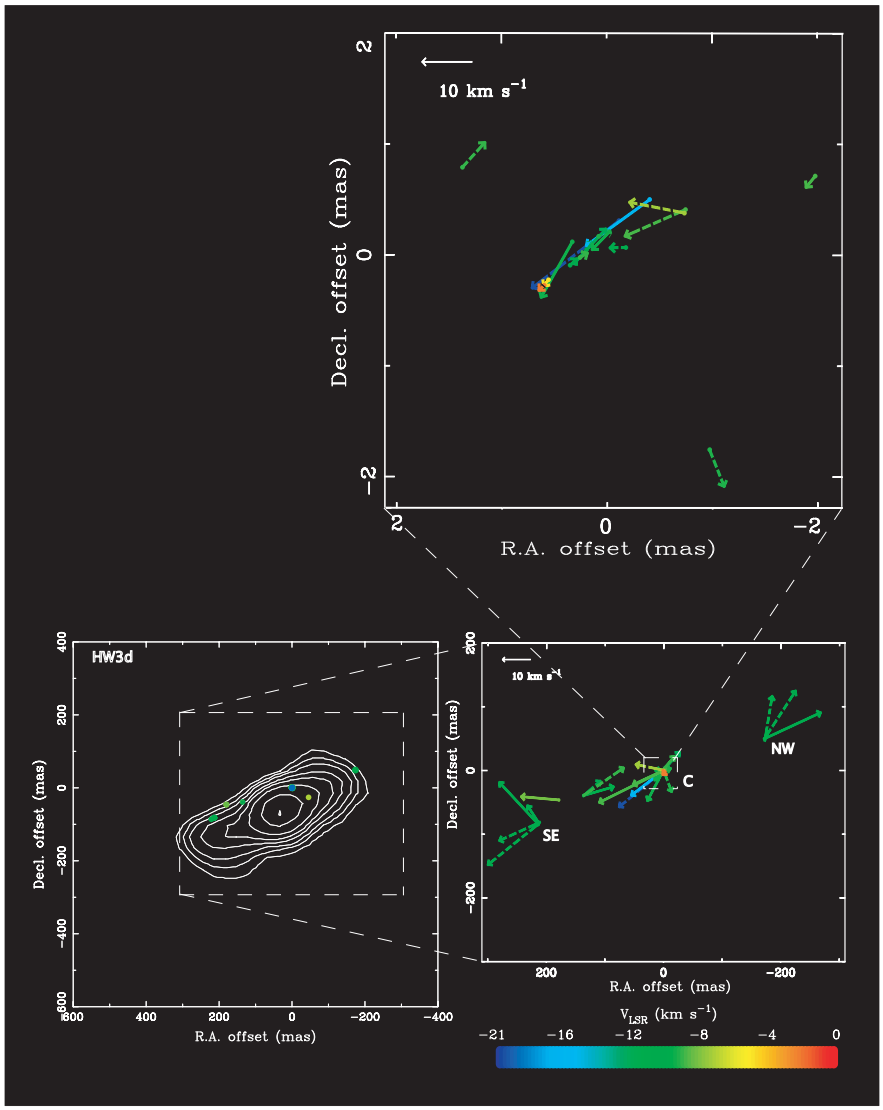

Figure 3.9: HW3d bipolar outflow - Left: The distribution of the H_2O masers detected in our VERA observations superposed to the HW3d 1.3 cm continuum map obtained with the VLA in 2006. Right: The proper motions of these maser features. The position, length, and direction of an arrow indicate the position, speed, and direction of the maser feature motion on the sky, respectively. The continuous lines represent proper motions traced in 3 or more epochs while the dashed lines represent those traced in 2 epochs only (see also Figure 3.10 - 3.12). The motion speed of 10 km s^{-1} is indicated by a white arrow length in the upper left corner. The color code indicates the LSR velocity of the individual maser features. The absolute coordinates of the (0,0) position (feature 15, Table 3.2) are RA(J2000) = $22^h56^m18.1753^s$, DEC(J2000) = $+62°01'46.2114''$.

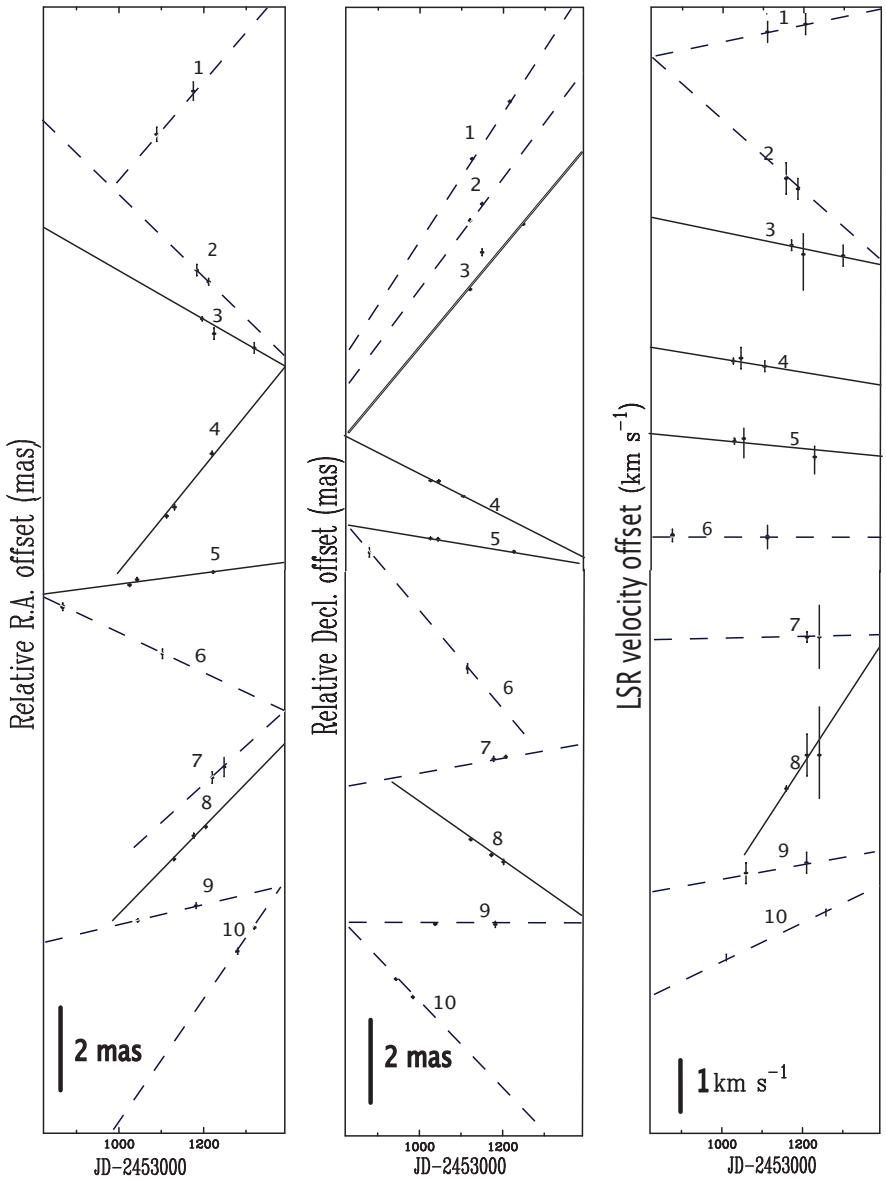

Figure 3.10: H_2O maser relative proper motions in the HW3d (i) -

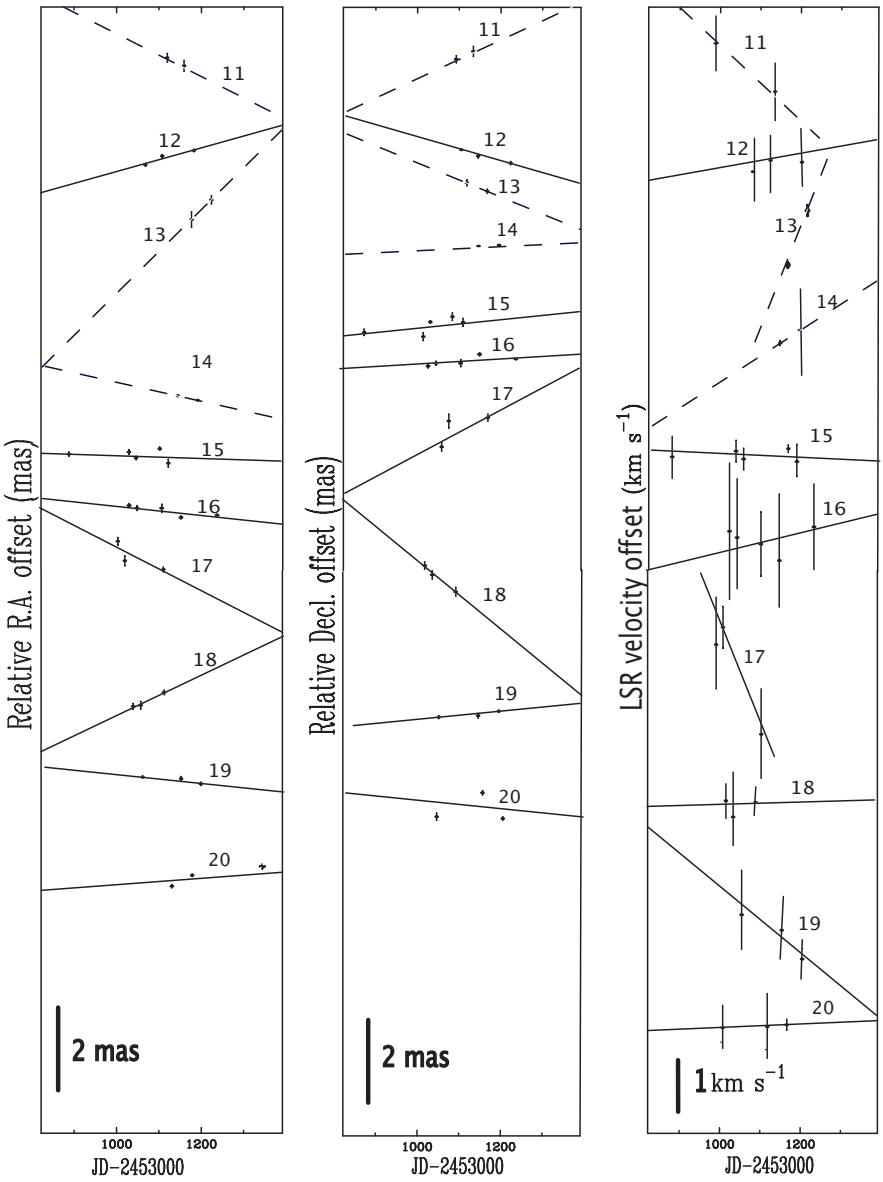

Figure 3.11: H_2O maser relative proper motions in the HW3d (ii) -

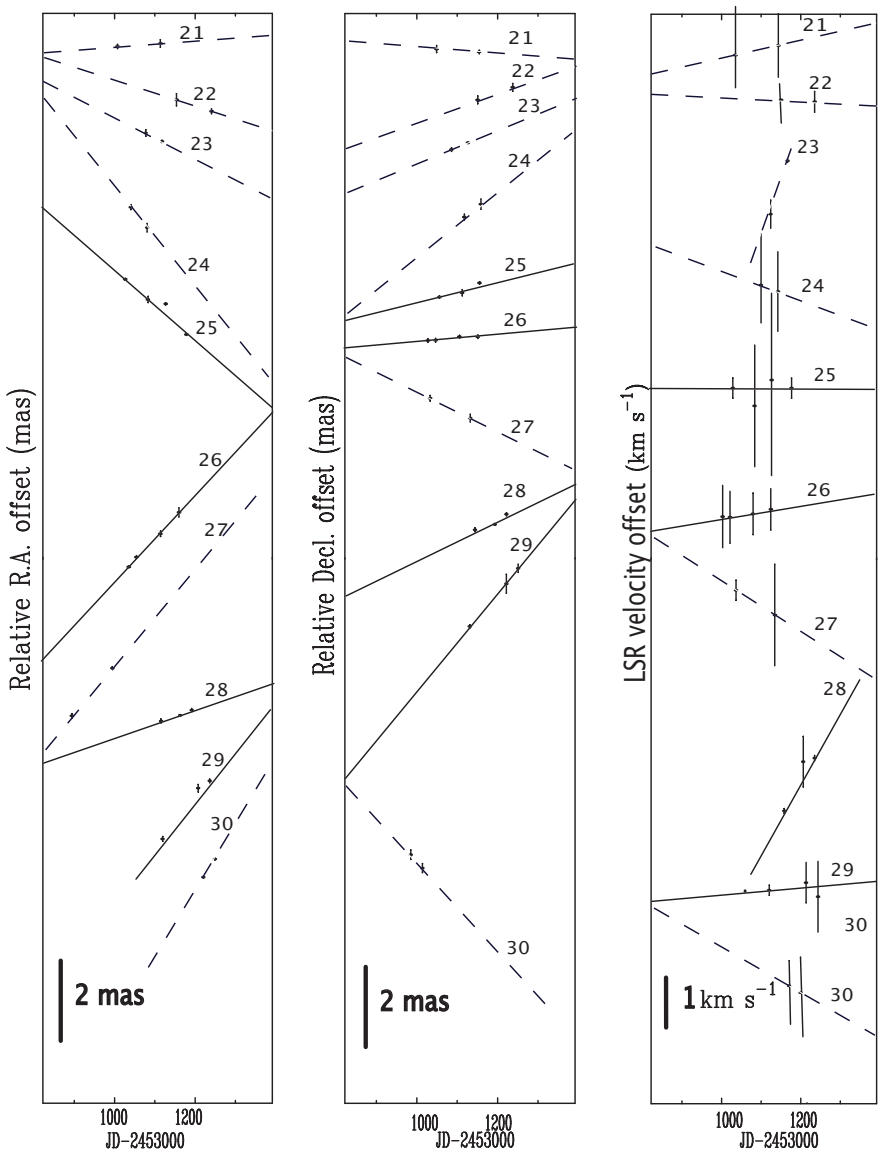

Figure 3.12: H_2O maser relative proper motions in the HW3d (iii) - Variation of the positions and the LSR velocities of maser features whose relative proper motions were measured. The proper motions were typically obtained in 3 or more epochs (continuous lines), those obtained in only 2 epochs (dashed lines) are either very isolated in velocity and/or position. See the main text for details.

ID	R.A. offset	Dec. offset	μ_x	$\sigma\mu_x$	μ_y	$\sigma\mu_y$	V_{LSR}
–	(mas)	(mas)	(mas yr^{-1})	(mas yr^{-1})	(mas yr^{-1})	(mas yr^{-1})	(km s^{-1})
1	−173.61	48.72	3.87	1.03	5.12	0.16	−10.37
2	−172.83	50.24	−3.23	1.84	4.56	0.62	−10.42
3	−172.29	49.61	−1.87	0.36	3.95	0.09	−10.00
4	−3.77	1.52	6.94	0.34	−3.16	0.22	−9.00
5	−2.10	0.66	0.48	0.08	−0.57	0.07	−9.00
6	−1.13	−1.80	−0.78	0.10	−1.91	0.11	−9.51
7	−0.90	0.33	2.92	3.08	0.56	0.80	−7.47
8	−0.58	0.45	3.37	0.25	−2.40	0.25	−16.15
9	−0.36	0.02	0.82	0.18	−0.02	0.18	−11.47
10	−0.30	0.26	4.64	0.66	−3.51	0.41	−20.48
11	−0.27	0.25	−1.59	1.37	1.54	1.21	−0.67
12	−0.21	0.16	0.91	0.12	−0.92	0.12	−9.82
13	−0.91	0.36	3.22	1.46	−1.38	0.58	−8.99
14	−0.11	0.12	−0.72	0.15	0.18	0.15	−9.41
15	0.00	0.00	0.00	0.00	0.00	0.00	−9.93
16	0.06	−0.07	−0.39	0.08	0.22	0.06	−9.24
17	0.11	−0.12	−1.67	0.29	1.77	0.37	−12.58
18	0.13	0.07	1.66	0.40	−2.89	0.63	−9.66
19	0.15	−0.14	−0.35	0.10	0.32	0.10	−10.84
20	0.35	−0.27	0.25	0.24	−0.33	0.19	−4.79
21	0.39	−0.32	0.26	0.39	−0.26	0.35	−1.79
22	1.14	0.74	−1.20	0.68	1.29	0.57	−9.33
23	135.90	−39.14	−1.70	0.70	1.37	0.42	−12.26
24	135.85	−39.03	−4.15	0.98	2.63	1.19	−9.22
25	136.46	−39.36	−3.12	0.07	0.84	0.09	−10.00
26	178.60	−46.23	3.91	0.23	0.32	0.16	−8.39
27	211.62	−81.55	4.18	0.23	−1.74	0.42	−10.63
28	213.08	−81.99	1.15	0.27	1.62	0.27	−12.15
29	213.21	−84.78	4.08	0.21	4.04	0.29	−10.37
30	214.91	−85.27	5.18	0.42	−3.83	1.87	−10.21

Table 3.2: Parameters of H_2O masers associated with HW3d and proper motions measured with VERA. - Parameters of H_2O masers associated with HW3d and proper motions measured with VERA. ID in column 1 refers to the maser feature ID number for identification purposes. The absolute coordinates of the (0,0) position (feature 15, Table 3.2), extrapolated from our astrometric analysis, are RA(J2000) = $22^h56^m18.1753^s$, DEC(J2000) = $+62°01'46.2114''$. + represents detection, while – represents non-detection in the different epochs.

ID	Epoch	Epoch	Epoch	Epoch	Epoch	Epoch	Epoch	Epoch	Epoch
–	1	2	3	4	5	6	7	8	9
1	–	–	–	–	+	–	+	–	–
2	–	–	–	–	–	–	+	+	–
3	–	–	–	–	–	–	+	+	+
4	–	–	+	+	+	–	–	–	–
5	–	–	+	+	–	–	–	+	–
6	+	–	–	–	+	–	–	–	–
7	–	–	–	–	–	–	+	+	–
8	–	–	–	–	–	+	+	+	–
9	–	–	–	+	–	–	+	–	–
10	–	–	–	–	+	+	–	–	–
11	–	–	–	–	+	+	–	–	–
12	–	–	–	–	+	+	–	+	–
13	–	–	–	–	–	+	+	–	–
14	–	–	–	–	–	+	+	–	–
15	+	–	+	+	–	+	–	+	–
16	–	–	+	+	+	+	–	+	–
17	–	–	+	+	–	+	–	–	–
18	–	–	+	+	+	–	–	–	–
19	–	–	–	+	–	+	+	–	–
20	–	–	+	–	–	+	+	–	–
21	–	–	–	+	–	+	–	–	–
22	–	–	–	–	–	+	–	+	–
23	–	–	–	–	+	+	–	–	–
24	–	–	–	–	+	+	–	–	–
25	–	–	–	+	+	+	+	–	–
26	–	–	+	+	+	+	–	–	–
27	–	–	–	+	–	+	–	–	–
28	–	–	–	–	–	+	+	+	–
29	–	–	–	–	+	–	+	+	–
30	–	–	–	–	–	–	+	+	–

Table 3.3: H_2O maser detection at the various epochs of observations with VERA. - H_2O maser detection at the various epochs of observations with VERA. ID in column 1 refers to the maser feature ID number for identification purposes. The absolute coordinates of the (0,0) position (feature 15, same as in Table 3.2), extrapolated from our astrometric analysis, are RA(J2000) = $22^h56^m18.1753^s$, DEC(J2000) = $+62°01'46.2114''$. + represents detection, while – represents non-detection in the different epochs.

3.4 Discussion

3.4.1 Properties of the Outflow

In order to test the originating point of the outflow exciting the surrounding H_2O maser features, we performed the least-squares method for the model-fitting analysis as presented by Imai et al. (2000, 2011). This fundamentally involves the minimizing of the squared sum of the difference between the observed and model velocities, S^2.

$$S^2 = \frac{1}{3N_{\rm m} - N_{\rm p}} \sum_{i}^{N_{\rm m}} \left\{ \frac{[\mu_{ix} - w_{ix}/(a_0 d)]^2}{\sigma^2_{\mu_{ix}}} + \frac{[\mu_{iy} - w_{iy}/(a_0 d)]^2}{\sigma^2_{\mu_{iy}}} + \frac{[u_{iz} - w_{iz}]^2}{\sigma^2_{u_{iz}}} \right\},$$

where $N_{\rm m}$ is the number of maser features with measured proper motions, $N_{\rm p}$ the number of free parameters in the model fitting, $a_0 = 4.74$ km s^{-1} mas^{-1}yr kpc^{-1} a conversion factor from a proper motion to a linear velocity, and d the distance ($\sim$ 700 pc) to the maser source from the Sun, respectively. μ_{ix} and μ_{iy} are the observed proper motion components in the R.A. and declination directions, respectively, $\sigma_{\mu_{ix}}$ and $\sigma_{\mu_{iy}}$ are their uncertainties, u_{iz} the observed LOS velocity, and σ_{iz} its uncertainty. For simplicity we assume a spherically expanding outflow. The modeled velocity vector, $\boldsymbol{w_i}$ (w_{ix}, w_{iy}, w_{iz}), is given as

$$\boldsymbol{w_i} = \boldsymbol{V_0} + V_{\rm exp}(i) \frac{\boldsymbol{r_i}}{r_i}, \tag{3.1}$$

where $\boldsymbol{V_0}(v_{0x}, v_{0y}, v_{0z})$ is the systemic velocity vector of the outflow,

$$\begin{aligned} \boldsymbol{r_i} &= \boldsymbol{x_i} - \boldsymbol{x_0} \\ &\quad (\text{or } r_{ix} = x_i - x_0,\ r_{iy} = y_i - y_0,\ r_{iz} = z_i), \end{aligned} \tag{3.2}$$

$$z_i = \frac{(u_{iz} - v_{0z})(r^2_{ix} + r^2_{iy})}{(u_{ix} - v_{0x}) r_{ix} + (u_{iy} - v_{0y}) r_{iy}}, \tag{3.3}$$

and

$$u_{ix} = \mu_{ix} a_0 d, \quad u_{iy} = \mu_{iy} a_0 d. \tag{3.4}$$

Eq. 3.3 satisfies the following constraint; the obtained position minimizes the value of S^2,

$$\frac{\partial S^2}{\partial z_i} = 0. \tag{3.5}$$

In this model, each maser feature is radially moving from a common originating point of the outflow with an expansion velocity, $V_{\rm exp}(i)$, which is approximated by

$$V_{\rm exp}(i) = \frac{(u_{ix} - v_{0x})r_{ix} + (u_{iy} - v_{0y})r_{iy} + (u_{iz} - v_{0z})r_{iz}}{r_i}. \tag{3.6}$$

The first step of the modeling considers the three dimensional position vectors of the maser features with respect to the originating point of the outflow by assuming that the individual maser features are moving independently and radially from the originating point. The free parameters of the model fitting are the position vector of the originating point (x_0, y_0) and the systemic motion vector of the outflow on the sky ($V_{0\rm x}$, $V_{0\rm y}$). $z_0 \equiv 0$ and $V_{0z} = -12$ km s^{-1} are fixed. Here we consider the possibility of a single driving source of the outflow.

Table 3.3 gives the parameters of the best-fit model. This fitting, considering the errors (within 2 sigma), is fully consistent with the origin of the bipolar outflow being at the position of the C H_2O maser cluster, supporting our interpretation given in §3.3.2 that the C cluster is the main center of activity containing a driving YSO.

	HW3d	HW3d(east)	HW3d(west)
$N_{\rm feature}$	30	13	17
Systemic proper motion:			
V_{0x} (km s^{-1})	−2.5±3.0	−21.8±3.6	11.9±0.1
V_{0y} (km s^{-1})	5.4±2.2	12.7±2.0	−1.2±0.1
Position offset:			
x_0 (arcsec)	0.020±0.010	−0.200±0.014	0.206±0.003
y_0 (arcsec)	−0.017±0.009	0.058±0.009	−0.060±0.004
$\sqrt{S^2}$ [1]	3.3	1.4	2.2

Table 3.4: Parameters of the best fitted expanding-flow models in the region HW3d, HW3d(east) and HW3d(west)

[1] Mean of the root-mean-square residual of the model fitting.

Figure 3.13 shows the distribution of the estimated expansion velocities of the maser features $V_{\rm exp}(i)$, in which the originating point of the outflow is considered to be at

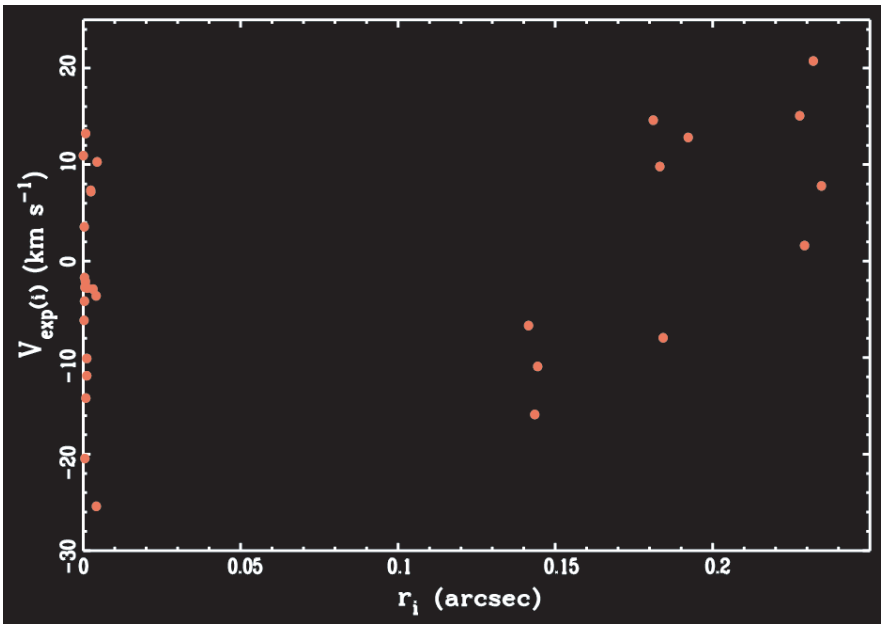

Figure 3.13: Expansion velocities of H_2O maser features - Distribution of the expansion velocities of the individual maser features, that were derived from the model fitting in HW3d (see §3.3.2). The absolute coordinates of the (0,0) position (feature 15, Table 3.2) are RA(J2000) = $22^h56^m18.1753^s$, DEC(J2000) = $+62°01'46.2114''$.

or very close to the position of Feature 15 (0,0) using all the maser features in HW3d (see Imai et al. 2000, 2011). If a single expanding flow exists, the data points should be concentrated on the range of positive expansion velocities. The maser kinematics in Cluster C seems to be significantly contaminated by random motion. It should be noted that this analysis has large uncertainties in the estimated sign of V_{exp} (positive or negative) for the individual maser features close to the estimated position of the originating point because the position estimated from the model fitting using the large scale maser clusters has a large uncertainty (see Table 3.4). Nevertheless, we cannot discard that some of these negative V_{exp} are due to infalling motions. In fact, to produce these infalling motions of $\sim$ 10 km s^{-1} at distances of 0.15″ (105 AU), a central binding mass of $\sim$ 12 $M_{\odot}$ would be necessary, which is not an unlikely value (a B3 star has been proposed to explain the radio continuum emission of HW3d; Garay et al. 1996). Alternatively, we also cannot discard that these masers, specially those at (+135 mas, -39 mas) are excited by a close YSO other than the driving source at the center.

Therefore we considered a second case, the presence of an exciting source in HW3d. This second case assuming the presence of 2 (or multiple) sources involved sorting the maser features into two groups HW3d(east) (13 maser features) and HW3d(west) (17 maser features), and repeating the expansion flow model fitting on both independently. We obtained positive expansion velocities for all the maser features in the HW3d(east) which is in line with the expected result of the model fitting within reasonable error. Similarly in all but 2 maser features in HW3d(west), we also obtained positive expansion velocities (see Figure 3.14). Considering the obtained estimated position of the exciting source, our model fitting supports the possibility of multiple sources above a single-source system.

3.4.2 Position and Velocity Variance/Covariance Matrix Analyses of the HW3d H_2O Maser Spatio-kinematics

We carried out the position and velocity variance/covariance matrix analyses of the H_2O maser spatio-kinematics to test the existence of an outflow in the H_2O maser region. The positional and kinematical essentials were extracted using the position and velocity variance/covariance matrix (PVVCM) diagonalization technique (Bloemhof 1993; 2000) for the whole maser feature proper motions. We estimated the uncertainties associated with the derived eigenvectors and eigenvalues from their standard deviations calculated

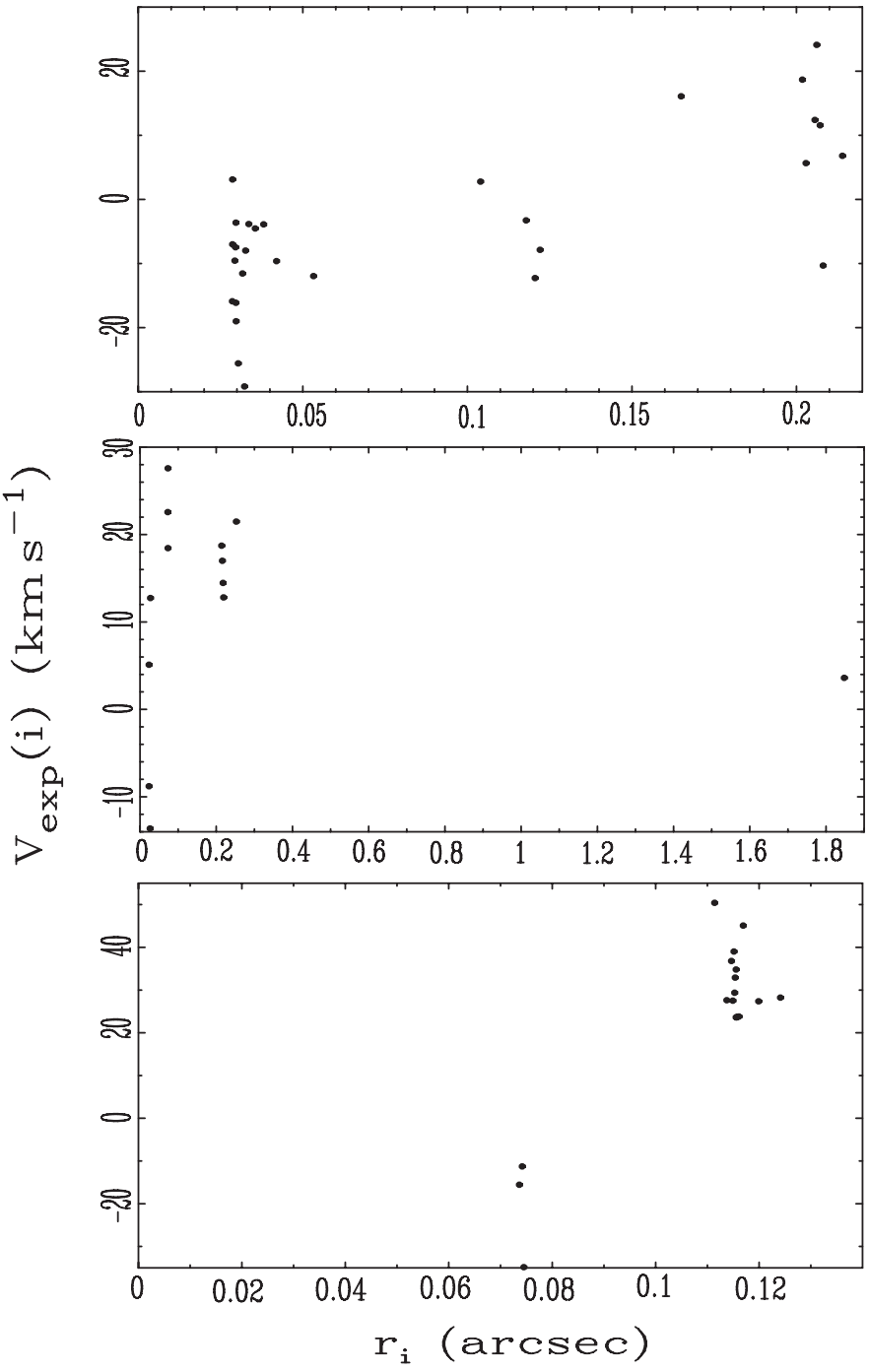

Figure 3.14: Expansion velocities of H_2O maser features in HW3d, HW3d(east), and HW3d(west) - Distribution of the expansion velocities of the individual maser features, that were derived from the model fitting in HW3d (top panel same as in Figure 3.13) using all the masers features(see §3.3.2), HW3d(east) (middle panel) ,HW3d(east) (bottom panel)

from the Monte Carlo simulation for the VVCM diagonalization using velocity vectors randomly distributed around the observed values within their estimated errors (Imai et al. 2006). This technique is not a model fitting approach, having no free parameters. It is a fully objective, analytic tool, generally composed of the following elements;

$$\sigma_{ij} = \frac{1}{N-1}\sum_{n=1}^{N}(v_{i,n} - \bar{v_i})(v_{j,n} - \bar{v_j}), \tag{3.7}$$

where i and j denote the two dimensional space axes in the case of position, or three orthogonal space axes in the case of velocity. n is the n-th maser feature in the collection summing up to N (= 30). The bar indicates averaging over the maser features. The diagonalization of the position variance-covariance matrix (PVCM) gives the essentials of the maser position field, while that of the VVCM gives the essentials of the velocity field. Classification of the spherical symmetry of an outflow into spherical outflow from a cometary or a bipolar outflow can be done using the relative magnitudes of the three principal velocity variances. The direction of the major principal axis gives the outflow axis of a bipolar outflow. PVCM and VVCM provide a robust and objective means of extracting the position and kinematic essentials from maser proper motions, and also support some other spherical symmetric or asymmetric model in deriving the vital clues from masers. The position angles and inclinations are derived from the eigenvectors obtained from the diagonalized matrices. As examples, the diagonalized matrices of one PVCM and one VVCM are shown below while the results are presented in Table 3.4.

We applied Eq. 1 in two spatial dimensions using the position offsets of all the 30 maser features. The x- and y- axes correspond to the Right Ascension and Declination respectively. The diagonalized PVCM in the unit of mas^2 as a 2×2 matrix is:

$$\begin{pmatrix} 11421.79 & -3811.39 \\ -3811.39 & 1308.13 \end{pmatrix} \Longrightarrow \begin{pmatrix} 12697.28 & 0 \\ 0 & 32.64 \end{pmatrix} \tag{3.8}$$

.

The larger eigenvalue of position dispersion is 389 times the smaller one. This indicates a very high collimation with respect to the position dispersion of the masers. The position angle, PA, of the eigenvector corresponding to the larger eigenvalue is 108°.

To verify our interpretation, we also made the 3-dimensional VVCM diagonalization analysis of the H_2O maser proper motions, obtaining the following 3×3 diagonalized matrix in units of km^2s^{-2}:

$$\begin{pmatrix} 85.49 & -35.62 & -7.62 \\ -35.62 & 59.99 & 5.00 \\ -7.62 & 5.00 & 12.50 \end{pmatrix} \Longrightarrow \begin{pmatrix} 111.41 & 0 & 0 \\ 0 & 34.90 & 0 \\ 0 & 0 & 11.66 \end{pmatrix} \tag{3.9}$$

.

The eigenvalues in the diagonalized matrix have one principal velocity variance dominating, 3 times the second largest eigenvalue. The factor of three between the largest eigenvalue with respect to the second one in the VVCM indicates collimation of water maser proper motions. The eigenvector $\nu_{\parallel}$ corresponding to the principal or largest eigenvalue corresponds to the axis of maximum internal velocity dispersion in the outflow. $\nu_{\parallel}$ lies at a position angle of 123°, and it makes a small inclination angle of -5° with the sky plane (the negative sign means that the vector is rising out of the plane, pointing towards the observer). The consistency in the position angles of the largest eigenvalues (108° and 123° for PVCM and VVCM analyses, respectively) within the error estimated from VVCM (see Table 3.4 for a quick summary of the results) indicates the existence of an outflow whose major axis is aligned with the major axes of the PVCM and VVCM.

The ratio of the second largest eigenvalue to the smallest eigenvalue characterizes the degree of transverse asymmetry in the maser outflow kinematics. The corresponding eigenvector to the second largest eigenvalue $\nu_{\perp}$ (connotes a principal axis in the perpendicular plane) gives some significant information about the outflow. The factor of three between the second largest eigenvalue and the smallest one indicates an azimuthally asymmetric collimated structure, and the cross section transverse to the main axis is an ellipsoid elongated in the direction of the eigenvector corresponding to the second largest eigenvalue. Such azimuthal asymmetry is found in the bipolar outflow in HW3d, in which $\nu_{\perp}$ lies at position angle of 33° and makes an inclination angle of 1° with the sky plane, pointing away from the observer.

In the case of the HW3d(east), we obtained the following 2×2 diagonalized matrix for the position dispersion in mas^2;

$$\begin{pmatrix} 9159.06 & -3351.58 \\ -3351.58 & 1290.62 \end{pmatrix} \Longrightarrow \begin{pmatrix} 10393.13 & 0 \\ 0 & 56.55 \end{pmatrix} \tag{3.10}$$

PVCM						
ψ_{max} [mas^2]		ψ_{min} [mas^2]		PA$_{max}$[1] [°]		
12697.28		32.64		108.5		
VVCM						
ψ_{max}	ψ_{mid}	ψ_{min}	PA$_{max}$	PA$_{mid}$[2]	ϕ_{max}[3]	ϕ_{mid}
[km^2 s^{-2}]	[km^2 s^{-2}]	[km^2 s^{-2}]	[°]	[°]	[°]	[°]
111.41	34.90	11.66	123.0±14.5	32.9±19.5	-5.3±2.5	0.9±0.4

Table 3.5: Position and velocity variance/covariance matrix analyses of the HW3d bipolar outflow. Position angle of the largest eigenvalue is represented by (ψ_{max}), while the position angle of the second largest eigenvalue is represented by (ψ_{mid}). ϕ_{max} & ϕ_{mid} represent the inclination angle of ψ_{max} and ψ_{mid} with respect to the sky plane, respectively.

[1]Position angle of the largest eigenvalue, (ψ_{max}). [2]Position angle of the second largest eigenvalue, (ψ_{mid}). [3]ϕ_{max} & ϕ_{mid} represent the inclination angle of ψ_{max} and ψ_{mid} with respect to the sky plane, respectively.

diagonalized matrix.

The diagonalized matrix of the position dispersion of the central cluster shows that the larger eigenvalue is about 184 times greater than the smaller eigenvalue. This indicates a coliimated outflow traced by internal motions of the masers in the HW3d(east) . The position angle, PA, of the eigenvector corresponding to the larger eigenvalue is -69.8°, similar to the PA obtained in the case of entire HW3d region.

We also obtained the following 3×3 VVCM diagonalized matrix in units of km^{2}s^{-2};

$$\begin{pmatrix} 113.28 & -30.92 & -4.14 \\ -30.92 & 51.55 & 0.84 \\ -4.14 & 0.84 & 8.84 \end{pmatrix} \Longrightarrow \begin{pmatrix} 126.25 & 0 & 0 \\ 0 & 38.75 & 0 \\ 0 & 0 & 8.68 \end{pmatrix} \tag{3.11}$$

diagonalized matrix.

Similarly, in the case of the HW3d(east) H_2O maser, the largest eigenvalue was 3 times the second largest eigenvalue. The eigenvector $\nu_{\parallel}$ corresponding to the principal or largest eigenvalue is the VVCM outflow axis which also corresponds to the axis of maximum internal velocity dispersion in the outflow. $\nu_{\parallel}$ lies at a position angle of -67.5°, and it makes a small inclination angle of -2° with the plane of the sky, pointing towards the observer. The corresponding eigenvector $\nu_{\perp}$ of the second largest eigenvalue has a

PA of 22.5° and makes an inclination angle of 1.5° with the sky plane, pointing away from the observer.

In the case of the HW3d(west), we obtained the following 2×2 diagonalized matrix for the position dispersion in mas^2;

$$\begin{pmatrix} 4587.02 & -1312.46 \\ -1312.46 & 375.65 \end{pmatrix} \Longrightarrow \begin{pmatrix} 4962.56 & 0 \\ 0 & 0.11 \end{pmatrix} \tag{3.12}$$

diagonalized matrix.

The diagonalized matrix of the position dispersion of the central cluster shows that the larger eigenvalue is about 4.5×10^4 times greater than the smaller eigenvalue. This indicated a very high coliimated outflow traced by internal motions of the masers in the HW3d(west) position dispersion. The position angle, PA, of the eigenvector corresponding to the larger eigenvalue is -74°, similar to the PA obtained in the case of entire HW3d region and HW3d(east).

We also obtained the following 3×3 VVCM diagonalized matrix in units of km^{2}s^{-2};

$$\begin{pmatrix} 75.89 & -42.74 & -10.61 \\ -42.74 & 76.53 & 8.41 \\ -10.61 & 8.41 & 15.97 \end{pmatrix} \Longrightarrow \begin{pmatrix} 120.68 & 0 & 0 \\ 0 & 33.60 & 0 \\ 0 & 0 & 14.11 \end{pmatrix} \tag{3.13}$$

diagonalized matrix.

Similarly, in the case of the HW3d(east) H_2O maser, the largest eigenvalue was 3.5 times the second largest eigenvalue. The eigenvector $\nu_{\parallel}$ corresponding to the principal or largest eigenvalue is the VVCM outflow axis which also corresponds to the axis of maximum internal velocity dispersion in the outflow. $\nu_{\parallel}$ lies at a position angle of -44.9°, and it makes a small inclination angle of -7.3° with the plane of the sky, pointing towards the observer. The corresponding eigenvector $\nu_{\perp}$ of the second largest eigenvalue has a PA of 44.5° and makes an inclination angle of 4.7° with the sky plane, pointing away from the observer.

In the case of the high velocity dispersion maser cluster (see Figure 3.9), we also made it PVCM and VVCM analysis. We obtained the following 2×2 diagonalized matrix for the position dispersion in mas^2;

$$\begin{pmatrix} 1.12 & -0.26 \\ -0.26 & 0.39 \end{pmatrix} \Longrightarrow \begin{pmatrix} 1.20 & 0 \\ 0 & 0.31 \end{pmatrix} \tag{3.14}$$

diagonalized matrix.

The diagonalized matrix of the position dispersion of the central cluster shows that the larger eigenvalue is about 4 times greater than the smaller eigenvalue. This indicated an outflow traced by internal motions of the masers in the d-cluster position dispersion. The position angle, PA, of the eigenvector corresponding to the larger eigenvalue is -72.5°, similar to the PA obtained in the case of entire HW3d region, HW3d(east) and HW3d(west).

We also obtained the following 3×3 VVCM diagonalized matrix in units of km^2s^{-2};

$$\begin{pmatrix} 62.63 & -33.31 & -13.43 \\ -33.31 & 29.64 & 11.18 \\ -13.43 & 11.18 & 19.16 \end{pmatrix} \Longrightarrow \begin{pmatrix} 87.68 & 0 & 0 \\ 0 & 15.61 & 0 \\ 0 & 0 & 8.14 \end{pmatrix} \tag{3.15}$$

diagonalized matrix.

Similarly, in the case of the HW3d(east) H_2O maser, the largest eigenvalue was 5.5 times the second largest eigenvalue. The eigenvector $\nu_{\parallel}$ corresponding to the principal or largest eigenvalue is the VVCM outflow axis which also corresponds to the axis of maximum internal velocity dispersion in the outflow. $\nu_{\parallel}$ lies at a position angle of -57.7°, and it makes a small inclination angle of 14.2° with the plane of the sky, pointing away from the observer. The corresponding eigenvector $\nu_{\perp}$ of the second largest eigenvalue has a PA of 67° and makes an inclination angle of 66° with the sky plane, pointing away from the observer.

3.4.3 Single Exciting Source Scenario in HW3d

Considering the maser feature proper motion obtained in the entire HW3d region, the symmetry of the collimation and the position of the dynamical center, one may easily be moved to judge the whole region as having one exciting source. In the case that there is only a single exciting source, (owing to the result obtained from the VLA 1.3cm continuum map of 1995 and 2006),then, the shift in the position of the peak of the continuum source must be as a result of the motion of the object relative to the HW2 region. Our estimation of the proper motion velocity per year yielded $\sim$65 km $s^{-1}yr^{-1}$. Such a high velocity is quite unlikely, thus increasing the likelihood of the 2 continuum peaks representing 2 different objects in close proximity, as phenomena common in the Cepheus A HW2 region. In Figure 3.13, against the expected positive

expansion velocities for the individual maser features, we obtained mostly negative velocities which indicates mass infall into the central object, along with some positive expansion velocities which indicates simultaneous mass loss through an outflow. If verified with a high resolution observation toward this source that there is only a single source in the HW3d, then our result will indicate the first observational evidence of mass accretion into a massive young stellar object at very high infall velocities traced by H_2O masers.

3.4.4 Multiple Exciting Sources Scenario in HW3d

A multiple source scenario seems more probable in the HW3d region. Our spatio-kinematics model fitting results of the maser proper motions assuming that 2 sources are present, yield expected positive expansion velocities for all the maser features in the HW3d(east) and all except for 2 proper motions in the HW3d(west). The unexpected high velocity seen in the result of the VLA 1.3cm continuum observation of 1995 and 2006, which tend to support the multiple source scenario may be a the case of the presence of variable intensity continuum sources. Our VVCM objective analysis also backs up the evidence of an outflow in HW3d(east) and HW3d(west). Though subject to verification, we think that the possibility of 2 or more objects in the Hw3d region is higher than just a single source scenario.

3.4.5 Jet Associated Maser Back Flow

Assuming a jet to be responsible for powering the observed outflow in HW3d, then the backward flowing maser proper motions could also be explained by the shock caused by the streaming of the jet. The passage of the jet generates some turbulence in the gaseous materials along its path. Generally, it is expected that the materials that has been kinematically excited by the jet move in the direction of the jet. But due to the supersonic nature of the jet, some of the jet-shock excited gases will deviate from the laminal flow and coil back towards the part of the jet. The coil-back motion towards the path of the jet is here referred to as back-flow motion. Though on a larger scale, similar back-flow can be seen in active galactic nuclei (AGN) (see Antonuccio-Delogu & Silk 2010), and this could be applied in principle to explain the maser proper motions in the opposite direction of the outflow in HW3d. While such a back-flow scenario

may be possible in HW3d, we want to note that our current data is not enough to independently verify it.

3.5 Conclusions

Our VERA proper motion measurements of H_2O masers have shown for the first time outflow activity in Cep A HW3d, implying that it harbors (at least) a YSO driving a high-collimated outflow at a scale of $\sim 0.4''$ ($\sim$ 280 AU), with a velocity of $\sim$ 21 km s^{-1} (with no consideration of the proper motions in the turbulent central maser cluster) and dynamical time-scale of $\sim$ 100 years. The outflow has an opening angle of 30° (see §3.3.2). The internal exciting source is probably a massive YSO (B-early star) to account for both the observed high intensity of the H_2O masers (up to $\sim$ 100 Jy for individual maser features) and the radio continuum emission ($\sim$ 10 mJy at 1.3 cm; e.g., Hughes & MacLeod 1993, Hughes, Cohen, & Garrington 1995, Garay et al. 1996, this paper). These characteristics are also seen in HW2, which has already been identified as a massive YSO (Patel et al. 2005; Torrelles et al. 2011), and indicates that during the process of formation of this likely massive YSO, a "YSO-jet" system has been formed, similar to what happens in the formation of low-mass stars.

However, not all the observed properties of HW3d can be explained with just a single YSO. In fact, the VERA observations show a cluster of H_2O masers located at $\sim$ (+135 mas, –39 mas), with proper motion vectors that do not fit within the bipolar expanding motions outward from the center (§§ 3.3.2, 3.3.3, and Figure 3.9). Another YSO might in principle be responsible for the excitation of the masers in that cluster. In addition, and most importantly, by comparing the HW3d 1.3 continuum emission observed in two epochs (1995 and 2006) with similar angular resolution ($\sim 0.1''$), we see that this source is variable in its total flux density($\sim$ 9 mJy [1995], $\sim$ 6.9 mJy [2006]), and on the other hand that the position of its peak emission has changed by $\sim 0.2''$ between these two epochs. We find that this position shift is highly significant, in particular when considering that the peak emission of the other two nearby objects HW2 and HW3c have not changed in position in these two epochs within $\sim$ 10 mas in right ascension and declination (see Figure 3.8). In the case that there was only a single exciting source, then the shift in the position of the continuum emission could be the result of the proper motion of the YSO. However, this would correspond to a YSO

velocity of ~ 65 km s^{-1}. Such a high velocity for the proper motion of the YSO itself is quite unlikely, thus buttressing the likelihood of the two continuum peaks representing two different YSOs in close proximity and high flux density variability. Alternatively, the change in the peak position could be due to internal proper motions of clumps in the jet with flux density variations. This radio continuum variability of HW3d was also previously reported by Hughes, Cohen, & Garrington (1995), which also invoked the presence of different variable YSOs to explain the main characteristics of the object.

This scenario can be tested with high-angular sensitive EVLA, and SMA (sub)mm observations to trace the dust continuum emission and molecular gas around the possible different YSOs associated with HW3d, and possible proper motions of the radio jet. These observations would also be very valuable to elucidate the nature of the YSO(s) (mass, dust and gas contents), and in particular to detect and study the expected circumstellar disk around the driving source of the compact bipolar outflow observed with VERA. The fact that in Cep A (the second closest high-mass star forming region after Orion) we have two very close "YSO-jet" systems, HW2 and HW3d (separated in the sky by $\sim 3''$, ~ 2100 AU), gives a unique opportunity to study their possible different properties in terms of the mass and evolution of the massive systems.

4

Astrometry and Spatio-kinematical Study of Water Masers Associated with NGC 6334I(N)

Adapted from Chibueze et al., 2013, PASJ, (in prep.)

4.1 Introduction

4.1.1 Overview of NGC 6634 Complex

NGC 6334 is one of the exciting massive star forming regions in the MilkyWay Galaxy. It forms one of the building blocks of the overall structure of our galaxy. In the Milkyway, NGC 6334 and NGC 6357 (northward) show extended structures of HII regions in the optical and infrared band. This is evidence that both are active sites of star formation, especially for high-mass stars able to to ionize their surroundings and form HII regions.

Kraemer & Jackson (1999) reported the mean velocity of the molecular emission against the local standard of rest (V_{LSR}) of NGC 6334 to be - 4 km s^{-1}, while Caswell & Haynes (1987) through radio recombination line obtained the V_{LSR} of NGC 6357 to be - 3.6 km s^{-1}. The similarity in the velocities may suggest that both regions are located at similar distance since they are spatially situated close to each other.

4. ASTROMETRY AND SPATIO-KINEMATICAL STUDY OF WATER MASERS ASSOCIATED WITH NGC 6334I(N)

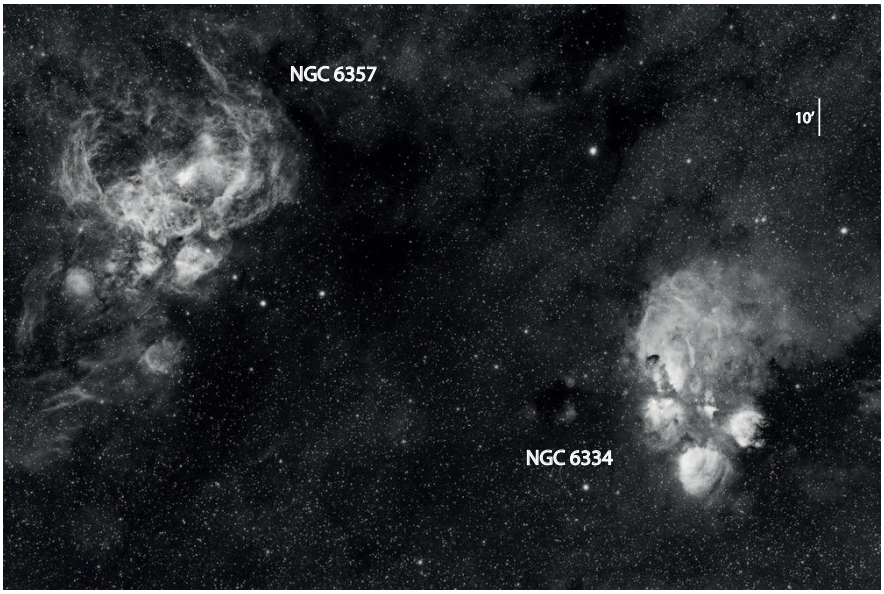

Figure 4.1: H_α image of NGC 6334 and NGC 6357 - Location of NGC 6334 (right) and NGC 6357 (left) close to the galactic equator (Adopted from http://www.astrosurf.com/antilhue/NGC6334NGC6357.htm).

1.2 mm cold dust emission observation of both regions by Russeil et al. (2010) showed that both regions are linked together by a filamentary structure which may be an indication that both regions belong to the same complex.

NGC 6334 is a massive star-forming complex located close to the galactic equator (an optical emission nebula popular called Cat's Paw nebula). The complex extends $32'$ $\times$ $40'$ across the sky. From the Sun, the distance to NGC 6334 complex was reported as 1.62 kpc (Persi & Tapia 2008). Figure 4.1 is an H_α image showing the various active spots in the complex NGC 6334. And Figure 4.2 is the Two Micron All Sky Survey (2MASS) image of NGC 6334 showing NGC 6334I(N) as a dark (less evolved) region than brighter NGC 6334I, both separated by $90''$ but show different characteristics (Beuther et al. 2005).

The positional location of the I and I(N) massive star forming regions in the complex is shown in Figure 4.3. Sandell (2000) reported some similarities in both sources, for example, size of $\sim 10''$ (0.08 pc) at a distance of 1.7 kpc (Neckel 1978), gas masses as $\sim$ 200 $M_\odot$ for NGC 6334I and $\sim$400 $M_\odot$ for NGC 6334I(N), but a difference in their bolometric luminosity, $\sim 2.6 \times 10^5$ $L_\odot$ for NGC 6334I and $\sim 1.9 \times 10^3$ $L_\odot$ for NGC 6334I(N).

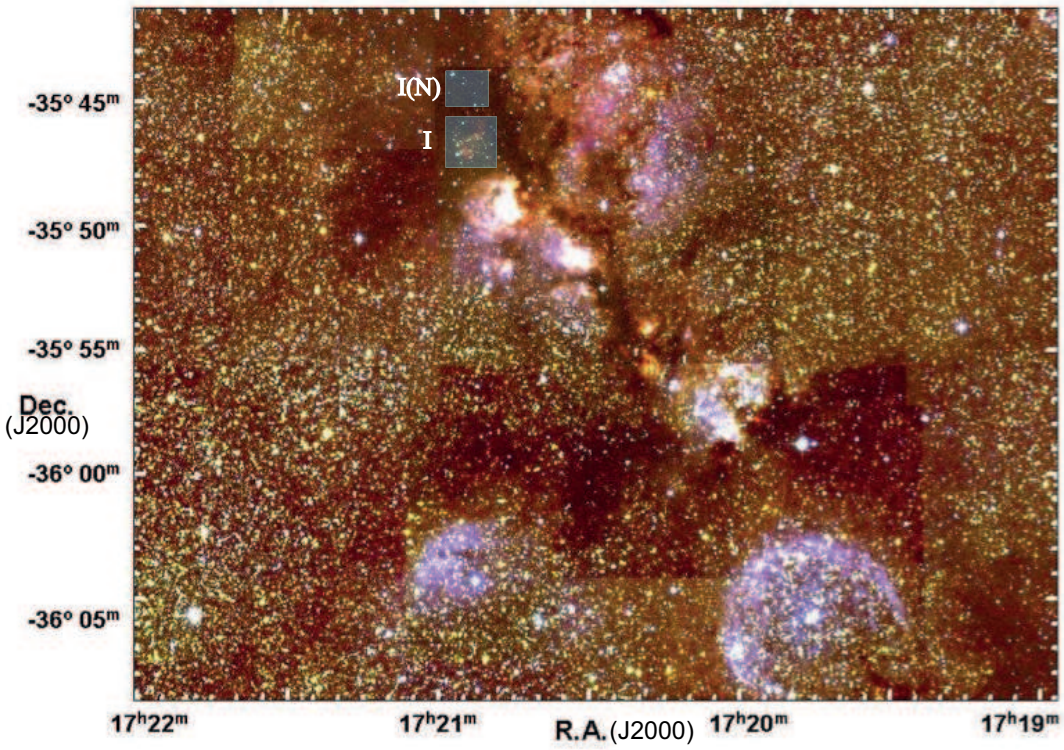

Figure 4.2: Two Micron All Sky Survey (2MASS) J, H, K bands color-composite image of NGC 6334 - The opaque regions show the NGC 6334I and I(N). The I region looks brighter, evidence of being more evolved than the I(N)

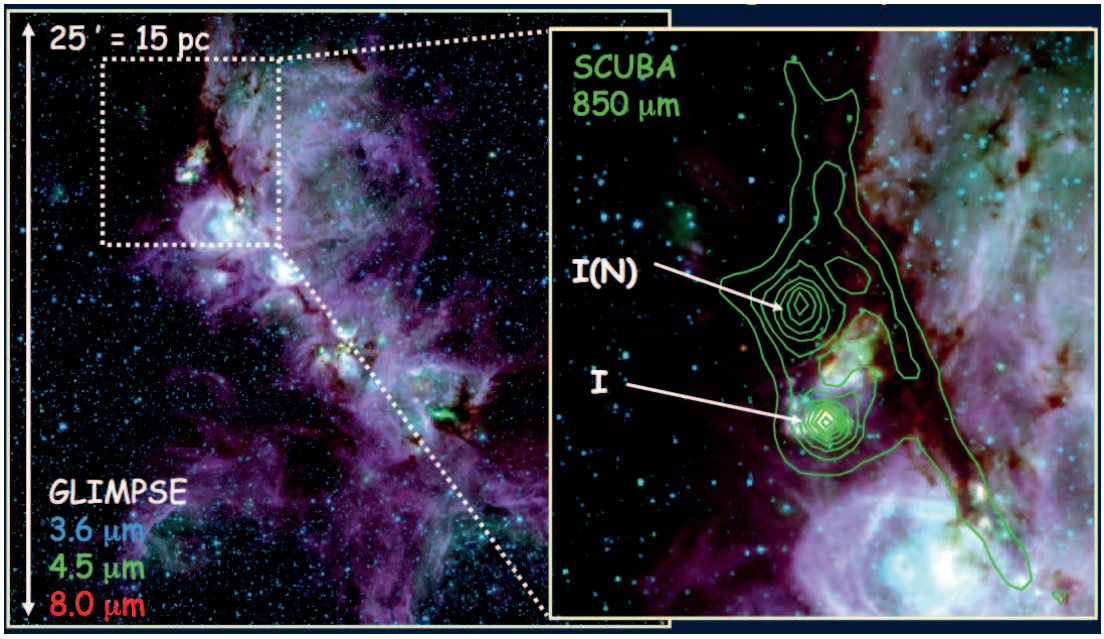

Figure 4.3: Spitzer/IRAC color-composite image of NGC 6334 from the GLIMPSE survey - (Left) GLIMPSE survey image of NGC 6334. The red, green, and blue represent the IRAC band 4 (8 μm), band 2 (4.5 μm), band 1 (3.6 μm), respectively. The right panel shows the location of the NGC 6334I and I(N) regions from SCUBA 850 μm image (green contours) overlaid on the Spitzer/IRAC image (*credit Brogan, C. L.*).

NGC 6334 has also been widely studied in the X-ray band, the first of such studies was done with the *Einstein satellite* by Harris et al. (1990). Ezoe et al. (2006) reported their Chandra observation results which covered the entire region. They successfully extracted the X-ray point sources and also analyzed the extended emissions. Figure 4.4 shows the Ezoe et al. wide-field map of the X-ray emissions in NGC 6334 complex.

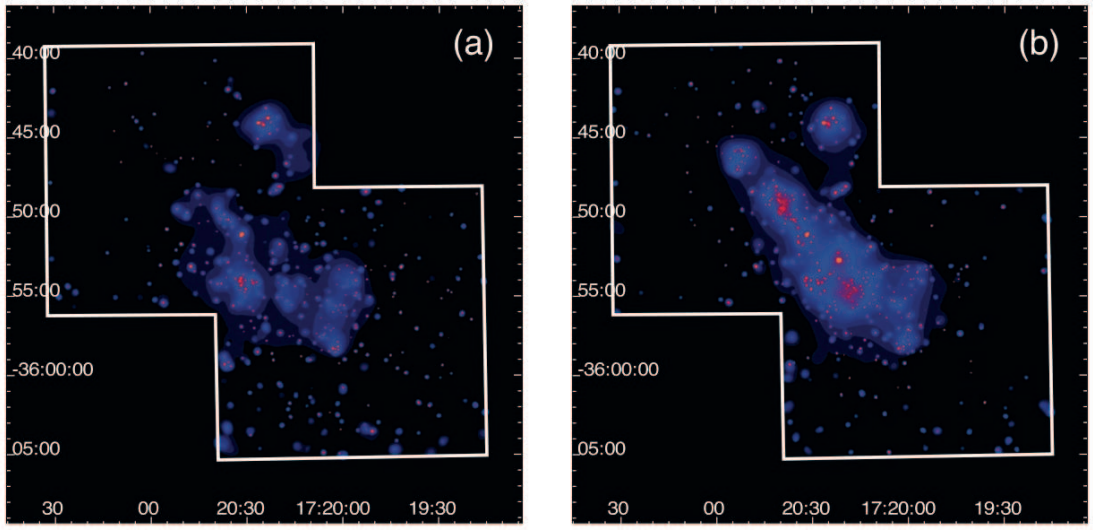

Figure 4.4: 0.5 - 3 keV & 2 - 8 keV smoothed X-ray images - Smoothed X-ray images of NGC 6334 in the 0.5 - 2 keV band (left panel), and the 2 - 8 keV band (Ezoe et al. 2006).

As indicated in the Chapter 1, accurate distance estimation is important to study massive star formation. Therefore, before elaborating the maser proper motions obtained in our JVN multi-epoch observations, we will first discuss the annual parallax and the consequent accurate distance determination using the VERA only subset of our data.

4.1.2 Annual Parallax Measurement of NGC 6334I(N)

Measurement of the distance to a massive star-forming region is vital for studying the physical conditions/properties like luminosity, masses, sizes and the evolution of the young stellar and/or protostellar objects. For instance, the measurement of the relative proper motion of H_2O in such star-forming regions require an idea of the distance to the source, the linear velocities of the proper motion may be wrongly estimated if the

distance value is grossly different from the actual distance. The widely used kinematic distance from the Sun to a source in the Milky Way Galaxy is derived from the radial velocity and the galactic rotation model. There is high risk of significant difference between the kinematic distance and the actual distance to the sources if their motion is much different from the assumed Galactic model due to nearby supernovae or super-bubble, motion of the spiral arm, or the potential of galactic bar.

Annual trigonometric parallax measurement is the most reliable and direct way of obtaining the distance to astronomical sources with high accuracy. With typically 1 mas accuracy, the Hipparcus satellite was able to measure the annual parallax of over 10000 stars (Perryman et al. 1997), making a quite significant contribution to astrometric measurements. Determination of trigonometric parallax and subsequent measurement of the distance with much higher accuracy has become possible with the recent astrometric very long baseline interferometry (VLBI) observation of sources exhibiting emission with high brightness which are provided by maser emissions.

While there may have been cases where parallax and kinematic distances of some sources are similar, some VLBI observations report showing significant difference in these two distances of some sources suggesting large peculiar motions of the source influenced by an expanding super-bubble (Sato et al. 2008), the gravitational perturbations from the galactic bar (Brunthaler et al. 2009), and an expanding arm effect (Sanna et al. 2009).

4.2 Observations and Data Reduction

The VERA observations of the NGC 6334I(N) H_2O masers (6_15–5_23) at a rest frequency of 22.235080 GHz were carried out in 10 epochs spanning about two years. The dates of the observation epochs are between 2010 February 6, and 2012 April 6 (see Table 4.1). All the VERA four stations participated in all the observations epochs giving a maximum baseline length of 2270 km. At some epochs we used Japan VLBI Network (JVN), which is composed of VERA and some other radio telescopes in Japan.

Using the dual-beam feature of the VERA telescopes, the H_2O masers of NGC 6334I(N) and a position reference source J1713−3418 were simultaneously observed. These two sources are spatially separated by 1°.44, hence, it was possible to use the VERA's dual-beam system. At each epoch, the total observation time was about 5 hours, including

the scans on NGC 6334I(N), a bandpass calibrator (NRAO 530), and the position reference source, J1713−3418. The data were recorded onto magnetic tapes at the rate of 1024 Mbps, providing a bandwidth of 256 MHz which were digitized in four quantization levels, and then divided into 16 base-band channels (BBCs) of 16 MHz each. One of the BBCs was assigned to the H_2O maser emission in NGC 6334I(N), while the remaining 15 BBCs were assigned to the continuum emission from the position reference source.

Code	Epoch	Telescope	Astrometry (VERA only)
r10037a	2010 February 6	VERA, NICT, Gifu	No
r10137a	2010 May 17	VERA, NRO	Yes
r10316a	2010 November 12	VERA, NICT	Yes
r11060b	2011 March 1	VERA, NRO	Yes
r11110a	2011 April 20	VERA, NRO	Yes
r11139a	2011 May 19	VERA, NRO	Yes
r11273a	2011 September 30	VERA	Yes
r11299a	2011 October 26	VERA	Yes
r12065a	2012 March 5	VERA, NRO	Yes
r12097b	2012 April 6	VERA, NRO	No

Table 4.1: Observation dates of NGC 6334I(N) with JVN.
JVN observations of NGC 6334I(N) showing the dates of the epochs of observations and usefulness for the annual parallax measurement. VERA represents all the 4 VERA telescopes (Mizusawa, Iriki, Ogasawara, and Ishigakijima), NRO is Nobeyama 45m telescope, NICT is the 34m NICT telescope in Kashima, and Gifu is the 11m Gifu telescope.

The data correlation was made with the Mitaka FX correlator. The accumulation period of the correlation was set to 1 second. The correlation outputs consisted of 512 and 32 spectral channels for the H_2O maser and reference continuum emission, respectively. The H_2O maser spectral resolution was 15.625 kHz, corresponding to a velocity resolution of 0.21 km s^{-1}.

The data reduction was made with the Astronomical Imaging Processing System (AIPS) package, developed by National Radio Astronomy (NRAO). We first recalculated the delay-tracking model in the Mitaka FX correlator using the newly cal-

culated model (Jike et al. 2005; Manabe et al 1991). This is because the current model in the Mitaka FX correlator does not have the sufficiently required accuracy for astrometric measurement. In the recalculation, we adopted the following equatorial coordinates; NGC 6334I(N) as $(\alpha_{J2000}, \delta_{J2000}) = (17^{\rm h}20^{\rm m}55^{\rm s}.192, -35^\circ45'03''.77)$, J1713−3418 $(\alpha_{J2000}, \delta_{J2000}) = (17^{\rm h}13^{\rm m}09^{\rm s}.941507, -34^\circ18'29''.4276)$ and NRAO 530 $(\alpha_{J2000}, \delta_{J2000}) = (17^{\rm h}33^{\rm m}02^{\rm s}.70579, -13^\circ04'49''.54823)$.

Considering the low declination ($\sim -35^\circ$) nature of NGC 6334I(N), the annual parallax measurement poses a big challenge. In a recent work by Kurayama et al. (2011), the annual parallax of MSXDC G034.43+00.24, located near the celestial equator, was successfully measured with VERA. In the data reduction, we have carefully followed the procedures used in Kurayama et al. (2011; see Appendix, with NRAO 530 serving the purpose of J1800+38). In simple terms, this involved amplitude and bandpass calibrations on the H_2O maser source and the position (phase) reference source. The fringe fitting solution of NRAO 530 in the B-beam was applied to J1713−3418 before executing the AIPS task FRING on J1713−3418 whose solution was applied to the target source NGC 6334I(N). The relative instrumental delays between the dual-beam receiving system was also removed (Honma et al. 2008)

Synthesis imaging and deconvolution with CLEAN was done with the AIPS task IMAGR with uniform weighting to achieve the highest spatial resolution. We obtained the maser peak positions and flux densities by carrying out an elliptical Gaussian fitting of the brightness distributions in each maser image cube using the AIPS task SAD.

4.2.1 Single Beam Imaging of H_2O Masers in NGC 6334I(N)

The JVN observations comprised of VERA, Nobeyama 45m, NICT Kashima 34m, Gifu 11m (only the first epoch) telescopes. Table 4.1 shows the various observation epochs and the participating telescopes. The data correlation was made with the Mitaka FX correlator. The accumulation period of the correlation was set to 1 second. The correlation outputs consisted of 512 and 64 spectral channels for the H_2O maser and reference continuum emission, respectively. A velocity spacing of 0.21 km s^{-1} was obtained in each spectral channel for the H_2O maser emission.

The data reduction was made with the National Radio Astronomy Observatory (NRAO) Astronomical Image Processing System (AIPS) package using standard procedures. The instrumental delay calibration was made with the scans on the calibrators.

The fringe fitting and self-calibration procedures were performed for a Doppler velocity channel including a bright maser spot (velocity component) in the SMA1 region of NGC 6334IN. Their solutions were applied to all the data and then the map of the maser clusters were made. The CLEANed image cubes of the maser source were created using the beam that was synthesized from naturally weighted visibilities. The typical size of the synthesized beam was $\sim$ 1.3 mas. The H_2O maser image cubes were made with a cell size of 0.2 mas. Because we carried out self-calibration procedure using a bright maser spot in the SMA1a region, the maser spot positions in the image cubes were measured with respect to the bright maser spot used for self-calibration mentioned above. For the wide-field mapping and objective maser spot identification, we used an automatic pipeline script which runs on the AIPS POPS environment and mainly consists of AIPS tasks and adverbs: IMAGR, IMSTAT, and SAD. The H_2O maser feature identification was done by adopting a signal-to-noise ratio cut-off of $\sim$ 8. From the Gaussian fitting errors, we estimated the accuracies of the relative positions of the maser spots to be 0.01 – 0.20 mas in Right Ascension and 0.02 – 0.30 mas in declination. The individual maser features were defined as clusters of maser spots or velocity components and each feature position was defined from the brightness peak of the feature following the identification method of Imai et al. (2002), also used in Chibueze et al. (2012).

4.3 Results

4.3.1 NGC 6334I(N) Trigonometric Parallax Measurement

We detected two relatively strong H_2O maser features in the NGC 6334I(N) after the phase-reference calibration procedures was carried out. The LSR velocities of these two features are - 7.15 km s^{-1} and - 9.85 km s^{-1}, respectively. The most consistently detected maser feature was the - 9.85 km s^{-1} velocity component, which was detected in 80% of all the observation epoch. Figure 4.5 shows the cross power spectra of the H_2O maser towards NGC 6334I(N). The H_2O maser lines were detected within the LSR velocity range of - 5 km s^{-1} and - 16 km s^{-1} (Figure 4.5).

The annual parallax was obtained to be 0.834 $\pm$ 0.047 mas corresponding to a distance of 1.25 $\pm$ 0.14 kpc. It is important to note that this is yet a preliminary result of the annual parallax measurement, which was done only with the 8 epochs in

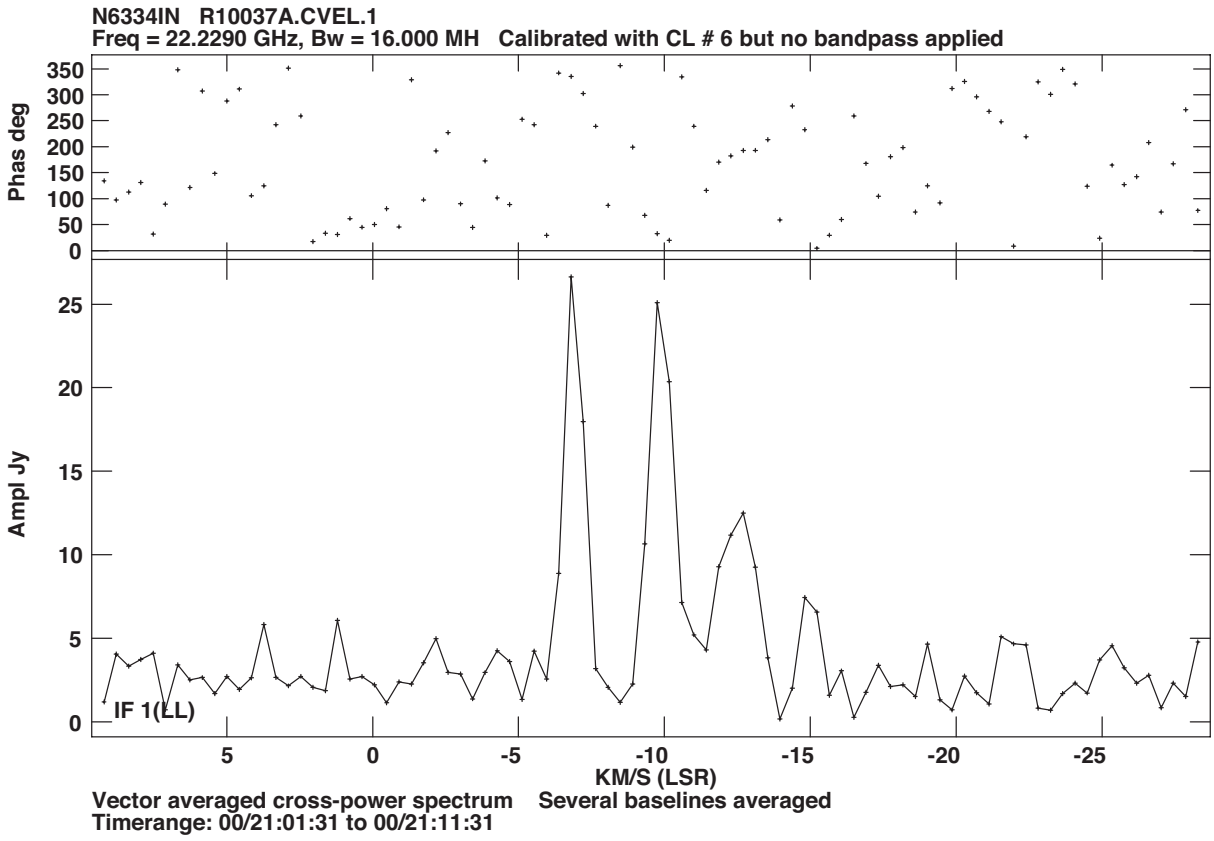

Figure 4.5: NGC 6334I(N) cross power spectra of the H_2O maser lines. - NGC 6334I(N) cross power spectra of the H_2O maser lines at the 2010 May 17 epoch. The -9.85 km s^{-1} velocity component was detected in 8 of the 10 epochs and was used for the annual parallax fitting procedure.

which the maser feature was detected without any problem. We are yet working on the other problematic epochs (low sensitivity due to bad weather conditions, weak and undetected position-reference source J1713-3418).

Figure 4.6 shows the positional motions of the maser feature. It is the convolution of the earth revolution around the Sun, and intrinsic proper motion indicated by the the straight arrow line. It is composed of the annual parallax and the intrinsic linear secular motion of NGC 6334I(N).

4.3.2 H_2O Maser Distribution in NGC 6334I(N)

We detected H_2O maser clusters corresponding to C1 to C11 (maser feature labels see Figure 4.7 right panel spectra), some associated with millimeter objects, others not associated with any millimeter source as previously reported by Brogan et al. (2009). A total of $\sim$ 200 maser features were detected in our observations. Figure 4.7 shows the distribution of the H_2O maser clusters detected in our JVN observation (R10137 epoch). Because the self-calibration procedure, using a bright maser spot in SMA1, was applied in order to detect weak maser spots, all the map origin represents the location of SMA1. We have investigated the correspondence of each maser cluster with the results of Brogan et al. (2009). Figure 4.8 shows the distribution of the H_2O maser clusters in SMA1.

4.3.3 JVN Study of the H_2O Maser Spatio-kinematics in NGC 6334I(N)

The maser features have been carefully registered and identification of the H_2O maser relative proper motions in the SMA1 maser cluster systematically carried out. Maser features coincident in LSR velocity within 1 km s^{-1} and position offset within 2 mas between epochs were used in tracing the proper motions. A larger fraction of the proper motions were traced in 3 or more epochs, while some were traced in just 2 epochs. The proper motions traced in 2 epochs are either clearly isolated in LSR velocity or position or in both. This is to avoid any case of proper motion misidentification by clearly discriminating those associated with extended structures before arriving at the 25 H_2O maser proper motions, we have carefully dropped some maser proper motions with high identification uncertainties. Table 4.2 shows the parameters of all the maser features used tracing the proper motions that will be discussed in the following (sub)section.

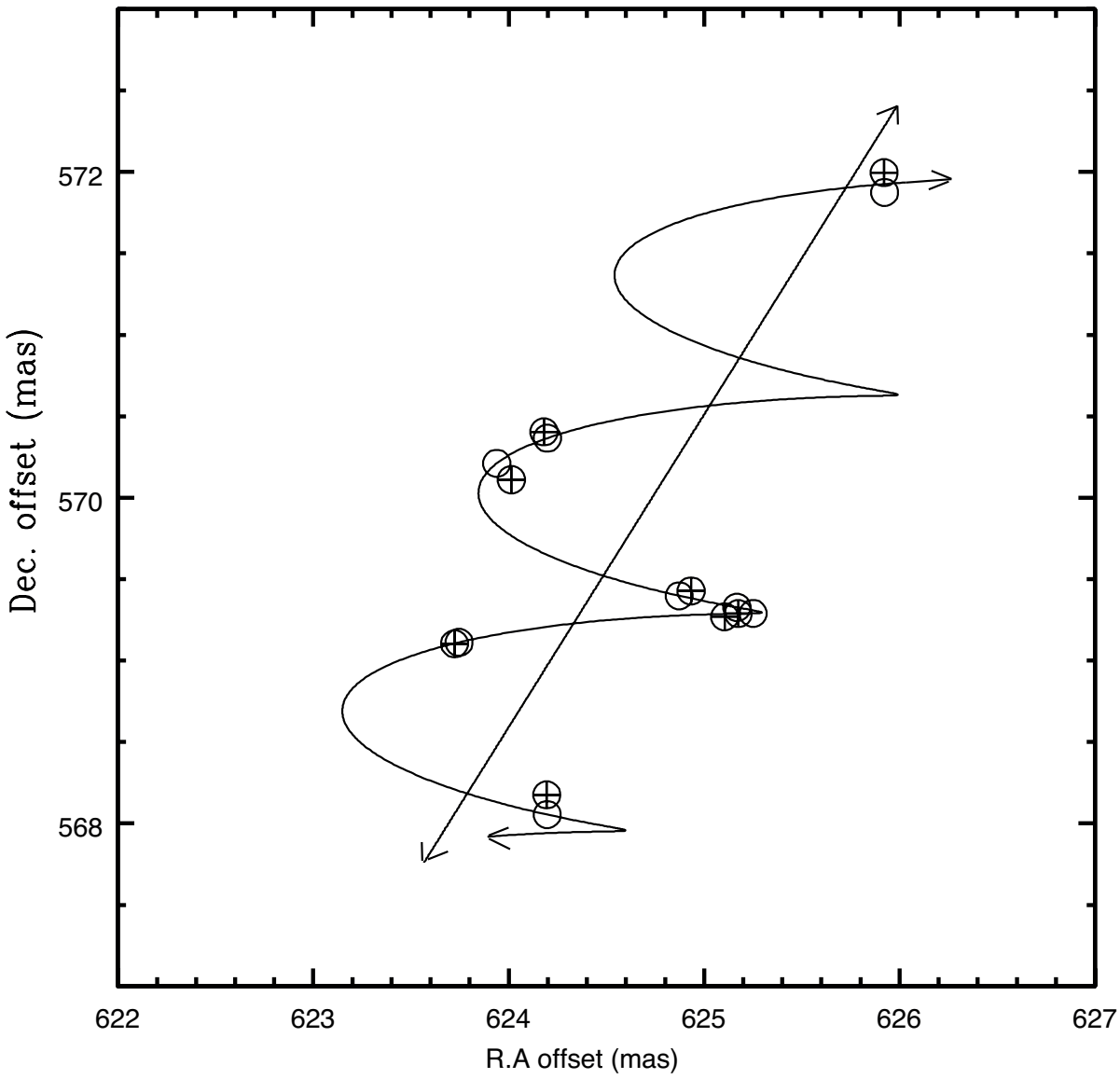

Figure 4.6: Annual parallax fitting result using the - 9.85 km s^{-1} H_2O maser velocity component. - The circled crosses represent the original data, while the open circles represent the model fitting output.

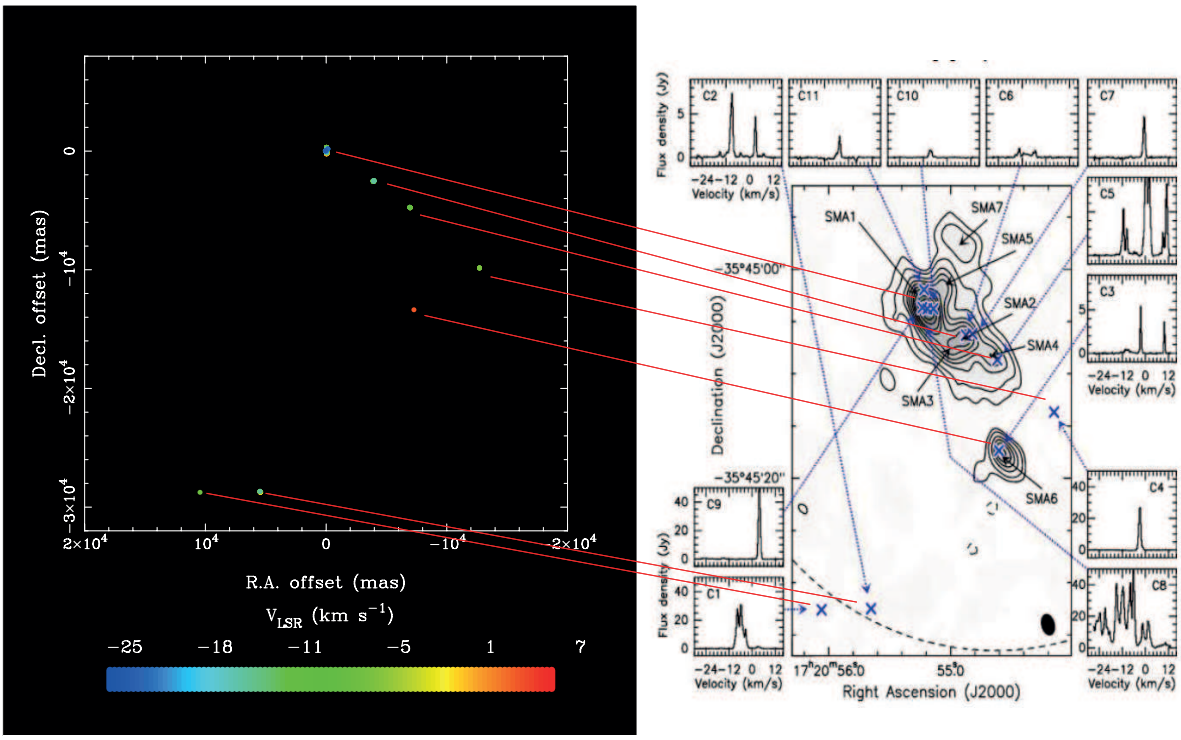

Figure 4.7: H_2O maser map of our R10137 epoch of JVN observations. - H_2O maser map of our R10137 epoch of JVN observations. We evidently detected all the maser clusters obtained with the VLA as reported by Brogan et al. (2009) (right panel).

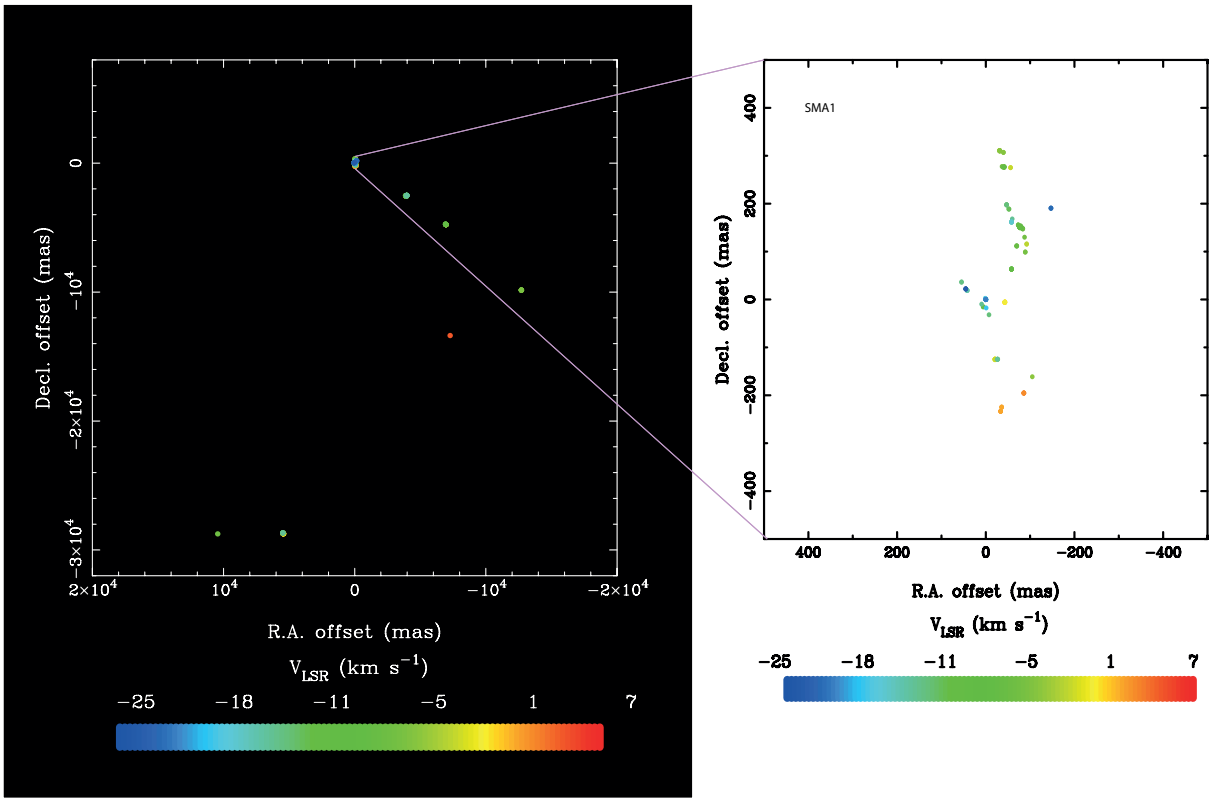

Figure 4.8: H_2O maser distribution in SMA1. - Zoom in of H_2O maser map of our R10137 epoch of JVN observations shown in Figure 4.8 above, showing the distribution of H_2O maser in SMA1 object(s) of NGC 6334IN.

ID	R.A. offset	Dec. offset	μ_x	$\sigma\mu_x$	μ_y	$\sigma\mu_y$	V_{LSR}
–	(mas)	(mas)	(mas yr^{-1})	(mas yr^{-1})	(mas yr^{-1})	(mas yr^{-1})	(km s^{-1})
1	17.17	30.26	-1.41	3.48	0.26	4.25	-16.96
2	17.19	31.41	3.82	1.87	1.00	4.20	-13.67
3	53.52	-191.32	3.85	0.28	-0.53	0.99	-11.47
4	18.32	33.85	2.93	1.95	8.57	4.83	-9.08
5	20.12	32.93	4.98	2.97	10.81	5.19	-7.68
6	56.00	-186.31	0.54	1.38	-7.13	3.17	-6.29
7	-23.40	31.13	35.20	1.86	12.22	5.14	-5.34
8	71.79	64.85	1.48	1.62	6.67	3.19	-0.81
9	5.49	9.26	0.85	0.39	2.81	0.67	-0.32
10	-32.33	233.50	0.53	1.48	8.45	3.45	-0.05
11	-0.18	2.62	1.11	0.05	-1.14	0.07	0.24
12	0.00	0.00	0.00	0.35	0.00	0.42	0.33
13	0.00	0.00	0.00	0.47	0.00	0.53	0.68
14	0.00	0.01	-0.73	0.05	-3.39	0.28	1.82
15	-24.92	-39.57	-1.35	1.66	-1.77	0.74	2.14
16	31.08	-324.22	9.37	0.22	-3.04	1.41	3.19
17	-62.00	-97.46	-2.69	1.53	-14.65	4.35	3.68
18	-26.84	-34.25	7.40	0.19	4.22	0.60	5.09
19	-4.51	-105.95	1.58	2.84	-12.15	5.53	7.18
20	-4.16	-111.88	-5.59	2.94	-2.28	8.39	10.63
21	-5.27	-108.93	-0.81	2.82	-3.51	6.80	11.42
22	-77.29	-88.16	-5.71	1.52	-2.91	4.04	13.16
23	-8.13	-113.02	-1.51	3.67	-11.40	6.17	19.28
24	-6.55	-111.70	-3.19	2.01	-11.48	4.40	21.77
25	-25.30	-108.31	-2.09	2.86	-12.22	4.95	26.66

Table 4.2: Parameters of H_2O masers associated with SMA1 and proper motions measured with JVN. - Parameters of H_2O masers associated with SMA1 and proper motions measured with JVN. ID in column 1 refers to the maser feature ID number for identification purposes.

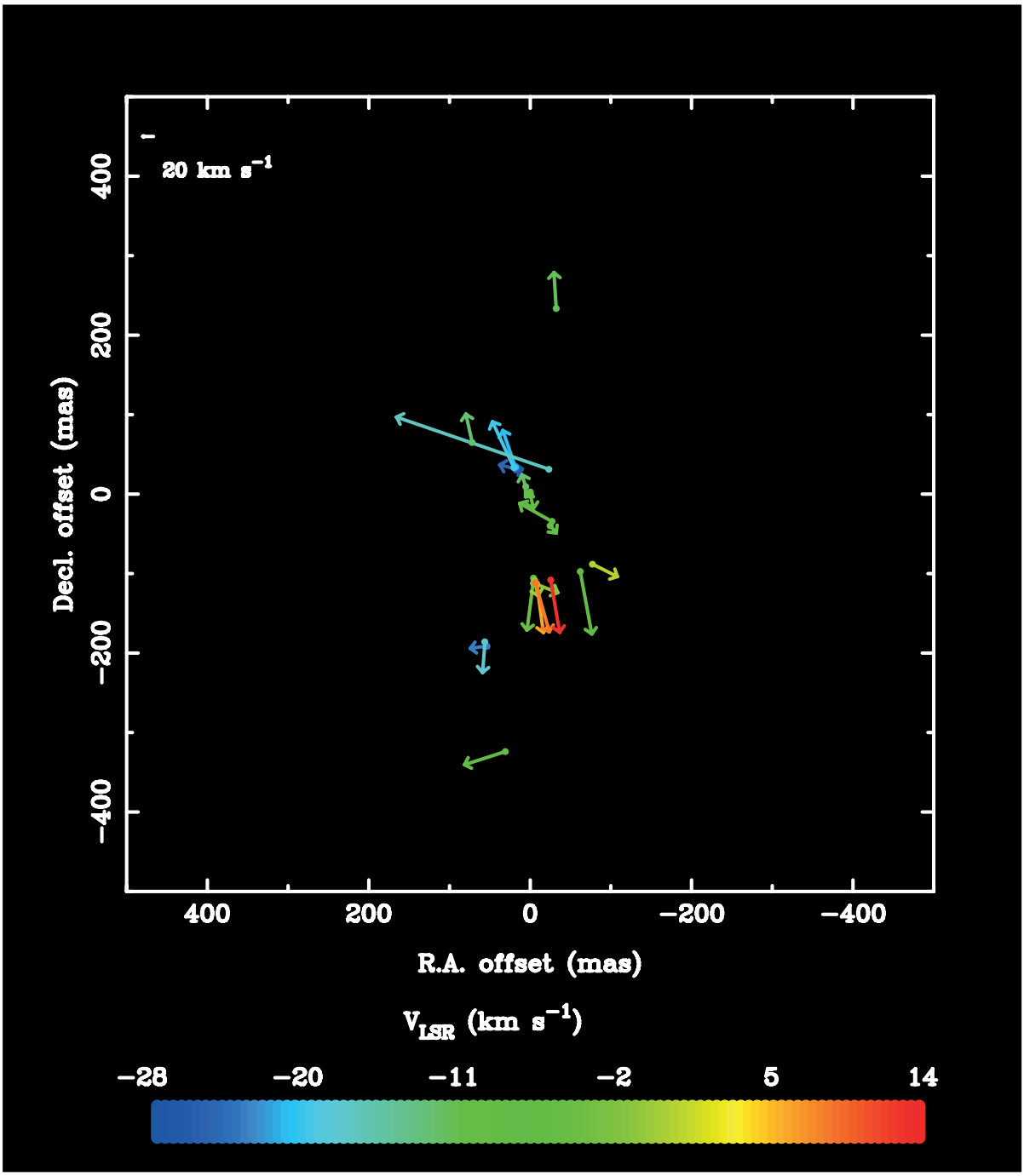

Figure 4.9: H_2O maser proper motions in SMA1 traced in our multi-epoch JVN observations. - H_2O maser proper motions in SMA1 traced in our multi-epoch JVN observations

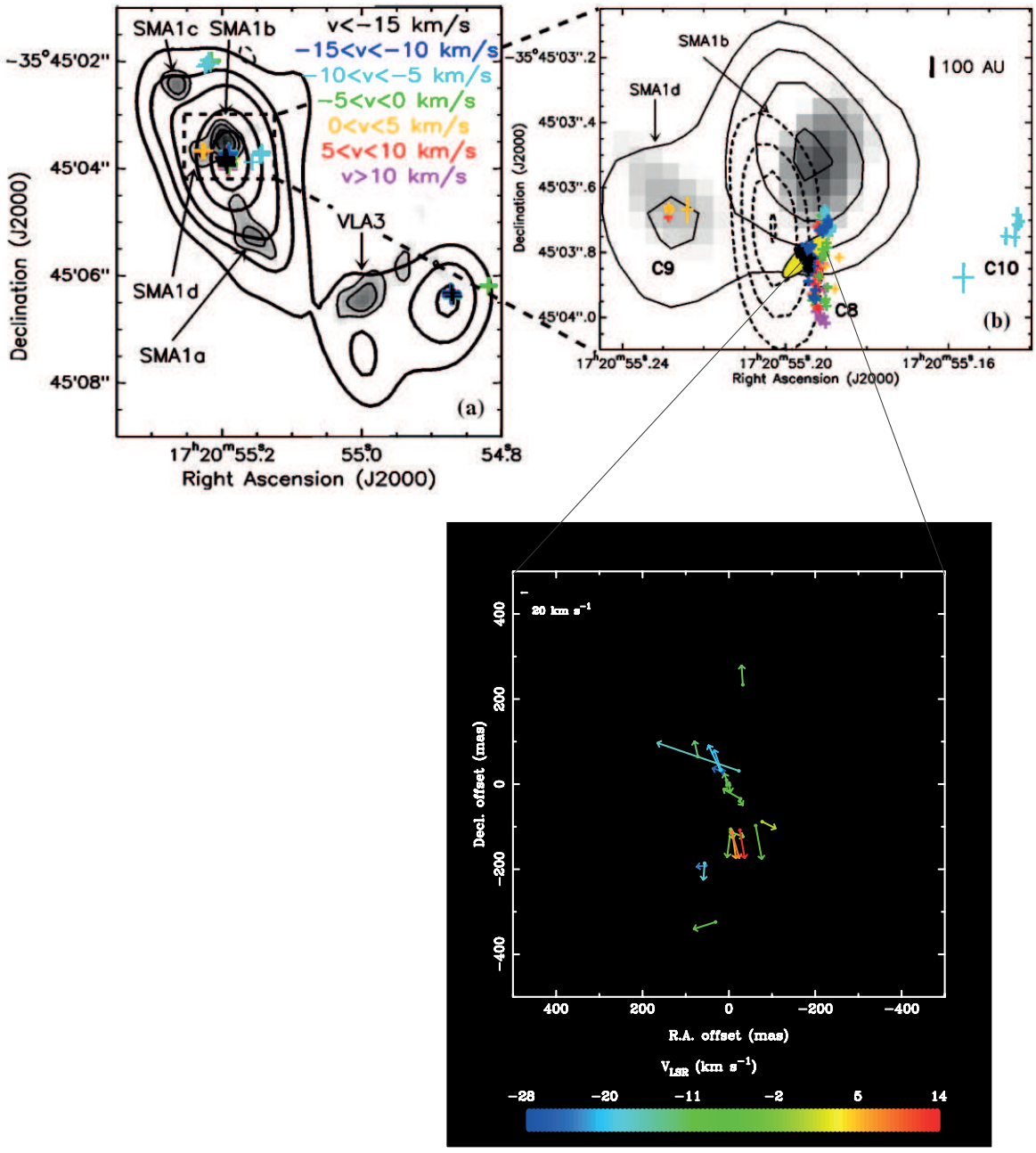

Figure 4.10: Driving source of the bipolar outflow in SMA1. - Driving source of the bipolar outflow in SMA1 object(s) of NGC 6334IN.

In this report we will focus our attention on the H_2O masers in the SMA1 object because we consistently detected a good number of them in all of the epochs. In fact, due to sensitivity issues, the low declination nature of the target source, the effect of the observation weather conditions and the non-participation of the NRO 45m and/or Kashima 34m telescopes in some of the epochs, only the strong masers in SMA1 was detected in such epochs. Therefore, we will center our discussion on the SMA1 masers.

4.4 Discussion

4.4.1 Position and Velocity Variance/Covariance Matrix Analyses of the SMA1 Associated H_2O Maser Spatio-kinematics

As in the case of Cepheus A HW3d (see Chapter 3), we carried out the position and velocity variance/covariance matrix analyses of the H_2O maser spatio-kinematics to test the existence of an outflow in the H_2O maser region. The positional and kinematical essentials were extracted using the position and velocity variance/covariance matrix (PVVCM) diagonalization technique (Bloemhof 1993; 2000) for the whole maser feature proper motions. We estimated the uncertainties associated with the derived eigenvectors and eigenvalues from their standard deviations calculated from the Monte Carlo simulation for the VVCM diagonalization using velocity vectors randomly distributed around the observed values within their estimated errors (Chibueze et al. 2012, Imai et al. 2006). This technique is not a model fitting approach, having no free parameters. It is a fully objective, analytic tool, generally composed of the following elements;

$$\sigma_{ij} = \frac{1}{N-1}\sum_{n=1}^{N}(v_{i,n} - \bar{v_i})(v_{j,n} - \bar{v_j}), \tag{4.1}$$

where i and j denote the two dimensional space axes in the case of position, or three orthogonal space axes in the case of velocity. n is the n-th maser feature in the collection summing up to N (= 30). The bar indicates averaging over the maser features. The diagonalization of the position variance-covariance matrix (PVCM) gives the essentials of the maser position field, while that of the VVCM gives the essentials of the velocity field.

Applying Equation 1 above, we also made the 3-dimensional VVCM diagonalization analysis of the H_2O maser proper motions, obtaining the following 3×3 diagonalized

matrix in units of km^2s^{-2}:

$$\begin{pmatrix} 1954.95 & 977.10 & -159.08 \\ 977.10 & 1773.24 & -276.15 \\ -159.08 & -276.15 & 115.64 \end{pmatrix} \Longrightarrow \begin{pmatrix} 2878.83 & 0 & 0 \\ 0 & 894.16 & 0 \\ 0 & 0 & 70.85 \end{pmatrix} \quad (4.2)$$

.

The eigenvalues in the diagonalized matrix have one dominant principal velocity variance, ~ 3 times the second largest eigenvalue. The factor of three between the largest eigenvalue with respect to the second one in the VVCM indicates collimation of water maser proper motions. The eigenvector $\nu_{\parallel}$ corresponding to the principal or largest eigenvalue corresponds to the axis of maximum internal velocity dispersion in the outflow. $\nu_{\parallel}$ lies at a position angle of 44.4°, and it makes a small inclination angle of -6.3° with the sky plane (the negative sign means that the vector is rising out of the plane, pointing towards the observer).

The ratio of the second largest eigenvalue to the smallest eigenvalue characterizes the degree of transverse asymmetry in the maser outflow kinematics. The corresponding eigenvector to the second largest eigenvalue $\nu_{\perp}$ (connotes a principal axis in the perpendicular plane) gives some significant information about the outflow. The factor of 12 between the second largest eigenvalue and the smallest one indicates an azimuthally asymmetric collimated structure, and the cross section transverse to the main axis is an ellipsoid elongated in the direction of the eigenvector corresponding to the second largest eigenvalue. Such azimuthal asymmetry is found in the bipolar outflow in SMA1, in which $\nu_{\perp}$ lies at position angle of 44.7° and makes an inclination angle of -6.7° with the sky plane, pointing towards the observer.

Table 4.3 shows the results of the VVCM and the PVCM analyses of the maser parameters obtained from SMA1 associated H_2O maser features.

4.4.2 Bipolar Outflow Powered by a Massive YSO in SMA1 Object

The astrometric analysis discussed in the §4.4 to 4.5 was used to determine the absolute positions of the masers for the purpose of making a comparative study of the proper motions with continuum emissions from the region. The traced maser proper motions extended ~ 500 mas with a northeast to southwest alignment. The blue shifted maser features are mostly moving in the northeast direction while the redshift maser features move in the southwest direction (see Figure 4.8). SMA1 is known to have 4 components

PVCM						
ψ_{max} [mas^2]		ψ_{min} [mas^2]		PA$_{max}$[1] [°]		
11689.92		1104.00		-2.7		
VVCM						
ψ_{max}	ψ_{mid}	ψ_{min}	PA$_{max}$	PA$_{mid}$[2]	ϕ_{max}[3]	ϕ_{mid}
[km^2 s^{-2}]	[km^2 s^{-2}]	[km^2 s^{-2}]	[°]	[°]	[°]	[°]
2878.83	894.16	70.85	44.4±6.7	44.7±4.9	-6.3±0.6	-6.7±5.2

Table 4.3: Position and velocity variance/covariance matrix analyses of the SMA1 bipolar outflow. Position angle of the largest eigenvalue is represented by (ψ_{max}), while the position angle of the second largest eigenvalue is represented by (ψ_{mid}). ϕ_{max} & ϕ_{mid} represent the inclination angle of ψ_{max} and ψ_{mid} with respect to the sky plane, respectively.

[1]Position angle of the largest eigenvalue, (ψ_{max}). [2]Position angle of the second largest eigenvalue, (ψ_{mid}). [3]ϕ_{max} & ϕ_{mid} represent the inclination angle of ψ_{max} and ψ_{mid} with respect to the sky plane, respectively.

SMA1a, b, c, and d resolved with the VLA (Rodríguez et al. 2007). The structure of the maser proper motions trace a bipolar outflow, and the typical proper motion velocity is 5 mas yr^{-1}. Brogan et al. (2009) suggested that the SMA1 may be housing an accreting ball with some signs of infall into the object, our detection of H_2O bipolar outflow suggest that a disk-YSO exist in SMA1 and could likely be associated with the SMA1b component (see Figure 4.9).

4.5 Conclusions

We made a multi-epoch JVN (including VERA) observations towards NGC 6334IN at $\sim$ 22 GHz, with the aim of determining its parallax distance and studying the maser 3-dimensional (3D) spatio-kinematics as a way of unveiling the massive star formation processes in the region.

We determined the annual parallax to be 0.834 ± 0.047 mas corresponding to a distance of 1.25 ± 0.14 kpc.

With focus on the SMA1, we measured, for the first time, the proper motions of 25 maser features. The structure of the maser proper motions trace a bipolar outflow, and the typical proper motion velocity is 5 mas yr^{-1}. Brogan et al. (2009) suggested that the SMA1 may be housing an accreting ball with some signs of infall into the object,

our detection of H_2O bipolar outflow suggest that a disk-YSO exist in SMA1 and could likely be associated with the SMA1b component (see Figure 4.9 & 4.10). While making effort to study the proper motion in other maser clusters in the region, we are exploring archive data from other observational wavelengths for more information about the exciting sources in the region.

4. ASTROMETRY AND SPATIO-KINEMATICAL STUDY OF WATER MASERS ASSOCIATED WITH NGC 6334I(N)

5

High Angular Resolution Sub-millimeter Array (SMA) Study of SM2 Object of NGC 6334I(N)

Adapted from Chibueze et al., 2013, ApJ, (in prep.)

5.1 Introduction

High-resolution sub & millimeter observation of the continuum and line emissions is indispensable in the understanding of massive star formation. Dust, thermal gas, and maser studies offer a spatially high dynamic-range view of massive star formation processes. In chapter 4, we explored the H_2O maser activities in NGC 6334I(N). Evidently, association/absence and kinematics of H_2O maser trace evolution of sites of star formation, and can be used in exploring the evolutionary sequence of high-mass stars. We would run through a brief introduction of the region, the recent sub & mm observation results in the region and then delve straight into our main results.

NGC 6334 provides a good laboratory for the study of massive star formation. It is an excellent site for studying the evolutionary sequence of massive stars as it houses high-mass stars of various evolutionary phases. The presence of different sizes of H II regions are clear evidence of the varying formation stages of the massive stars in the

regions. Persi & Tapia (2008) estimated the distance to NGC 6334 to be 1.6 kpc, which is 100 pc lesser than the 1.7 kpc suggested by Neckel (1978). However, our ongoing very long baseline (VLBI) water (H_2O) maser annual parallax suggests that distance to NGC 6334, particularly the I(N) region may be $\sim$ 30% less than the above reported values.

The I(N) region was first reported by Cheung et a. (1978) and subsequently by Gezari (1982). Since then it has been studied at various wavelengths. H_2O as well as class I and II methanol (CH_3OH) are good tracers of massive star formation activities, and these masers have been detected in the I(N) (Brogan et al. 2009, Kogan & Slysh 1998, Walsh et al. 1998). Hunter et al. 2006 and Brogan et al. 2009 presented strong evidence that the I(N) is a cluster of compact cores through their millimeter dust continuum observations with SMA1 as the most prominent of the resolved cores. Rodríguez et al. (2007) resolved SMA1 into 4 components with their very large array (VLA) 7 mm continuum observations.

This chapter focuses on an object in the south-west of NGC 6334I(N) named SM2. It is important to note that SM2 is not the same as SMA2 (names after SMA by Hunter et al. 2006). SM2 was first detected in by Sandell (2000) in 1000 μm dust emission observations of NGC 6334I and I(N) regions using the James Clerk-Maxwell Telescope (JCMT). It has an estimated mass of 70 M $\odot$. Brogan et al. (2009) detected two H_2O maser clusters (C1 and C2) at RA(J2000) = $17^h20^m56.058^s$, DEC(J2000) = -35°45′32.59″ and RA(J2000) = $17^h20^m55.650^s$, DEC(J2000) = -35°45′32.48″. Megeath & Tieftrunl (1999) reported two outflows, one of them found around SM2, C1 & C2. Brogan and collaborators suggested the outflow to be the most plausible explanation of the widespread spatial distribution of the 44 GHz CH_3OH observed in the region. Interestingly, SM2 is associated with an X-ray source reported by Feigelson et al. (2009), which led to the suggestions that SM2 may be a cluster of YSOs because of the existence of X-ray and the estimated central luminosity which is greater than the value obtained from the far-IR SED (Brogan 2009). However, there are some recent reports of class 0 YSOs with H_2O masers, associated with X-ray sources (Kamezaki et al. 2013).

In this work, we present the results of the sub-millimeter array (SMA) continuum and line observations with the beam centered on SM2.

5.2 Observations and Data Reduction

NGC6334I(N)-SM2 was observed by the SMA with eight antennas in the compact configuration on 23 April 2011 in excellent weather conditions for the 1.3 mm band. The 225 GHz zenith opacity measured by the tipping radiometer at the nearby Caltech Submillimeter Observatory ranged from 0.04 to 0.06, and the 33 m baseline of the SMA atmospheric phase monitor (Kimberk et al. 2012) showed a 32-second phase rms of $\sim 0.4^{\circ}$. We used the single polarization, double bandwidth observing mode with an LO of 224.8417 GHz, yielding 4 GHz of spectral coverage in both lower sideband (216.87-220.84 GHz) and upper sideband (228.84-232.82 GHz). The correlator channel spacing was 0.8125 MHz ($\sim$ 1.1 km s^{-1}). The target field (J2000 phase center = $17^{\rm h}2055^{\rm s}.71$, -35°45′34″.1) was observed from 02:30 to 05:00 HST interleaved with the phase calibrator J1733-130 in a 13 minute cycle. A secondary phase calibrator (J1924-292) was observed every other cycle. The flux calibrator (Titan) was observed at the beginning of the track and the bandpass calibrator (3C454.3) was observed at the end. We first applied the system temperature corrections in MIRIAD (Sault et al. 1995), then loaded the data into CASA (Petry et al. 2012, McMullin et al.2007) for subsequent calibration and imaging. In our imaging, we used Briggs weighting with the robust parameter of 0.5 producing a synthesized beam of $1''.6 \times 0''.9$. The primary beam of the SMA at this frequency range is $\sim 54''$. For the details of the CASA data calibration and imaging tasks and parameters used, see the Appendix in §8.3 of the last chapter.

5.3 Results

In order to clearly show the significance of our new results, it is important to briefly flash back on the past results. Figure 4.7 (right panel) shows the naturally weighted SMA 1.3 mm continuum emission reported by Brogan et al. (2009) (a completely re-reduced continuum image of Hunter et al. 2006, corrected for a half-channel error in SMA velocity labeling identified after publication of the data in 2007). The positions of the H_2O maser clusters obtained with the VLA as shown in blue crosses. SMA1-7 were detected as shown in the figure, most of which are associated with H_2O maser emissions labeled as cluster C1-11 (see Table 5.1 for the detailed positions and properties of the H_2O maser clusters). It is important to note that 3 (C1, C2, and C4) out of the 11

maser clusters were not associated with any 1.3 mm continuum sources, and that C2 cluster position corresponds to the SM2 object first detected by Sandell (2000) using the JCMT at 1100 μm. This implies that SM2 (initially at a cold core phase) may not have been detected because of its location at the edge of the primary beam of Brogan et al. (2009) and Hunter et al. (2006) observations, or it was not evolved enough to be detected.

Cluster ID	RA (J2000)	Dec (J2000)	Associated mm source (offset)	Peak Intensity (Jy beam^{-1})	Peak Velocity (km s^{-1})	Velocity Range (km s^{-1})
1	$17^h20^m56.058^s$	-35°45′32″.59	SM2 (4.50″)	38.3	-6.0	+5.2 to -16.2
2	$17^h20^m55.650^s$	-35°45′32″.48	SM2 (1.78″)	9.2	-9.0	+7.2 to -15.6
3	$17^h20^m54.600^s$	-35°45′17″.27	SMA6 (0.67″)	8.8	-2.2	+10.4 to -12.6
4	$17^h20^m54.152^s$	-35°45′13″.66	–	29.0	-2.7	-0.7 to -4.4
5	$17^h20^m54.618^s$	-35°45′08″.65	SMA4 (2.11″)	17.7	-0.2	+12.4 to -12.9
6	$17^h20^m54.870^s$	-35°45′06″.32	SMA2 (0.55″)	2.7	-13.3	-4.7 to -15.6
7	$17^h20^m54.819^s$	-35°45′06″.18	SMA2 (1.11″)	5.3	-0.7	+0.2 to -1.7
8	$17^h20^m55.192^s$	-35°45′03″.77	SMA1b (0.24″)	78.1	-6.3	+13.1 to -26.8
9	$17^h20^m55.228^s$	-35°45′03″.66	SMA1d (0.02″)	75.7	-3.9	+5.2 to +2.2
10	$17^h20^m55.147^s$	-35°45′03″.78	SMA1 (0.53″)	3.4	-8.6	-7.7 to -9.6
11	$17^h20^m55.215^s$	-35°45′02″.02	SMA1 (1.96″)	5.5	-4.4	-3.7 to -6.3

Table 5.1: Water Maser Clusters Detected in NGC 6334I(N) with VLA at $\sim$ 22 GHz.
Water Maser Clusters Detected in NGC 6334I(N) with VLA at $\sim$ 22 GHz.

Figure 5.1 shows the naturally weighted 1.3 mm continuum emission of SM2, observed at the center of the primary beam. We successfully detected the compact continuum of SM2, and also another compact object southwest of SM2. Our results when compared with the results of Brogan et al. (2009) could be helpful in tracing the star formation phase at which H_2O maser emissions are pumped, and this is most likely to be prior to the hot core phase. Unresolved mm object cluster SM1-5,7 and distinctively resolved SMA6 object were detected. Prior to focusing attention on the SM2, it would be nice to briefly describe the properties of the SMA sources in the region.

5.3.1 Properties of the SMA Objects in the Region

While our recently observation of NGC 6334IN region detected the SMA1-7, the center of the primary beam of our observations focused on the SM2 object and the SMA1-7 objects are near the edge of the primary beam reducing the sensitivity. Therefore most of the description of the SMA sources below are based on previously published results,

but the SM2 properties are based on our new results. **SMA1** is the most evolved object in the I(N) region, the rotational temperature of the SMA1 hot core is 189 ± 19 K, associated with a forest of mm molecular line emissions. (Brogan et al. 2009; Hunter et al. 2006; Sandell et al. 2000). Its status as the most evolved source in the region is evident in the size of its millimeter continuum emissions and its association with the brightest H_2O maser cluster in the region. It is also associated with mm molecular outflows. Rodríguez et al. (2007) resolved SMA1 into multiple components (sources) with VLA at 7 mm, and the sources are named as SMA1a, SMA1b, SMA1c, and SMA1d by Brogan and collaborators. SMA1b and SMA1d may be thought to be the same source based on the 7 mm image, which only shows SMA1d to be an eastern elongation from SMA1b, and separated by $\sim 0''.45$ ($\sim$ 800 AU). SMA1d has also been detected at 3.6 cm (Carral et al. 2002) and is shown to be clearly distinct from the VLA 1.3 cm image (see Figure 4.7 right panel). Table 1 of Brogan et al. 2009 shows the observed properties of the compact continuum sources at various wavelengths.

SMA2 located southwest of SMA1 is a less evolved source compared to SMA1. SMA2 is a weak hot core with a rotational temperature of 154 ± 14 K. Like the SMA1 it housed several mm molecular lines. It also has a pole-on outflow evident in its blue shifted H_2O masers and its H−2CO emission. SMA4 and SMA6 share some similar properties as SMA1 and SMA2, but the SMA3 and SMA7 needs more observational data in order to classify and explore their properties (see details of the properties of SMA1-7 in Brogan et al. 2009, 2013).

5.3.2 Dust Continuum of the SM2 Object

SM2 source is the central focus of our SMA observations taken 2011 April 23. Previous mm observations toward this I(N) did not detect this object and the most important result presented in this chapter is the exploration of the mm continuum and molecular lines detected in SM2. Brogan et al. 2009 suggested that the 22 GHz H_2O maser cluster C2 is associated with no 1.3 mm continuum source. We have resolved the SM2 in our new observations, detecting its continuum and line emissions. This is an indication that H_2O masers are emitted at an early phase of star formation, prior to the formation of the hot core. A hot core is an early evolutionary phase of a massive star when a significant increase in core temperature develops and thermal lines are emitted. The compact continuum of SM2 source at 1.3 mm has a peak intensity of $\sim$

1.7 Jy, and shows a slight northeast-southwest elongation. The continuum elongation aligns well with the distribution of its associated H_2O maser features detected with the Japanese VLBI Network (JVN). It also aligned well with the H_2CO emissions for the source which traces mm molecular outflow from the hot core.

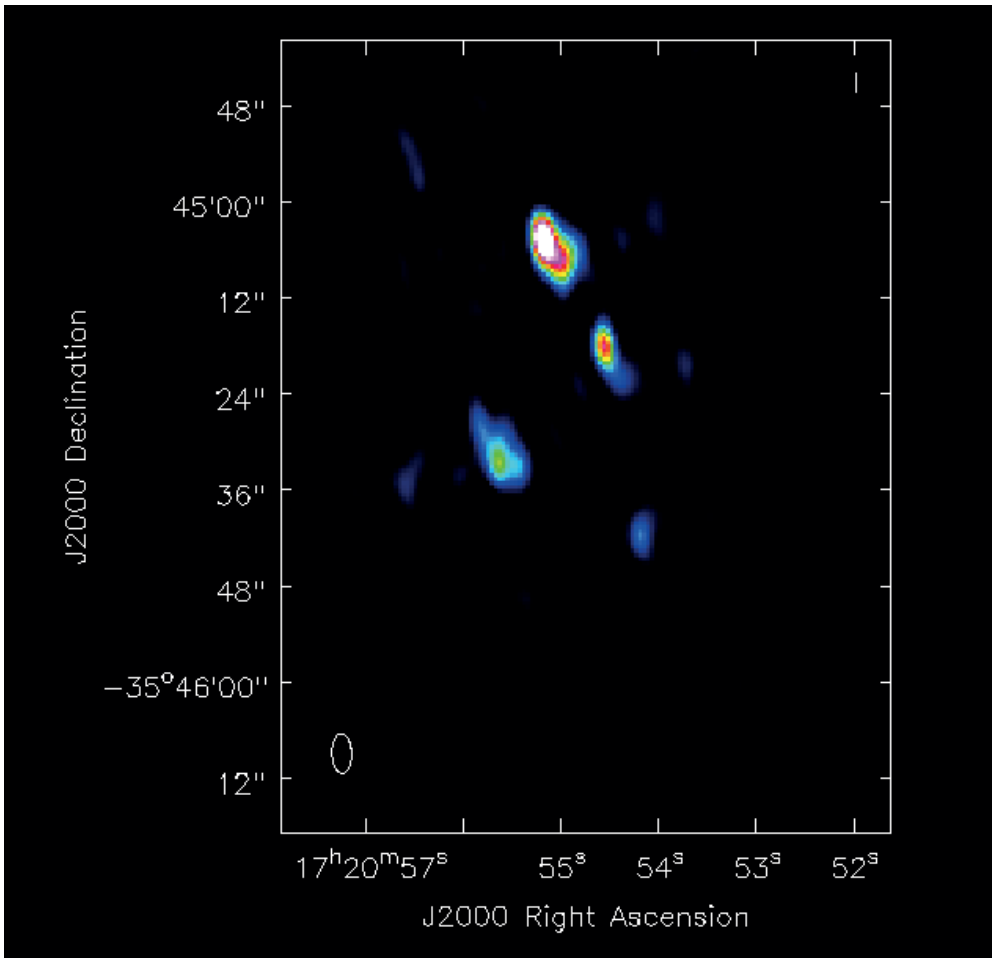

Figure 5.1: Compact 1.3 mm emission of the NGC 6334I(N) - Compact 1.3 mm continuum emission of NGC 6334I(N) SM2 hot core detected with the SMA.

5.3.3 SM2 Compact Molecular Line Emissions

Using the Spatalogue and the JPL line catalog, we have identified a good number of compact molecular lines in the SM2 object. Although the emissions from higher excitation lines are concentrated towards the SMA1-6, our focus would be on the mm

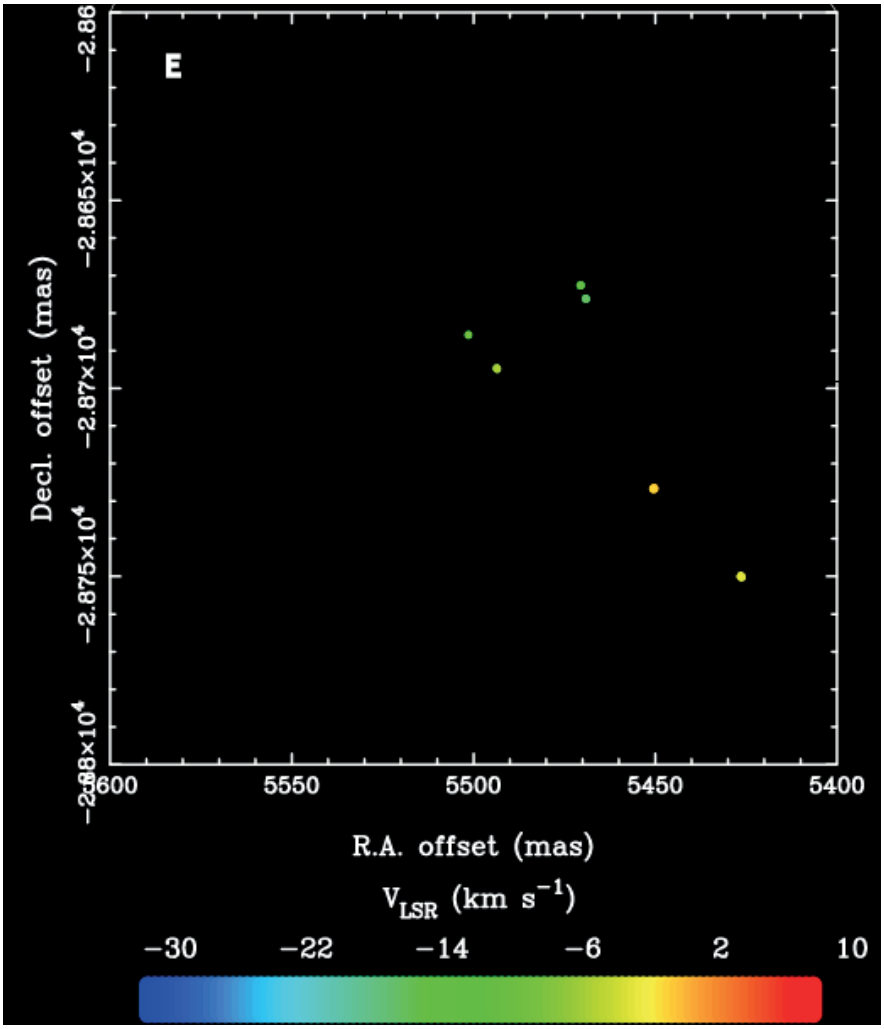

Figure 5.2: SM2 associated H_2O maser features detected with the JVN - SM2 associated H_2O maser features detected with the JVN. The H_2O maser features are distributed in a linear pattern, which aligns with the slight elongated structure seen in the continuum emission of SM2.

line emissions from SM2. For the discussions of the millimeter line properties of SMA1-6, see Brogan et al. (2009)

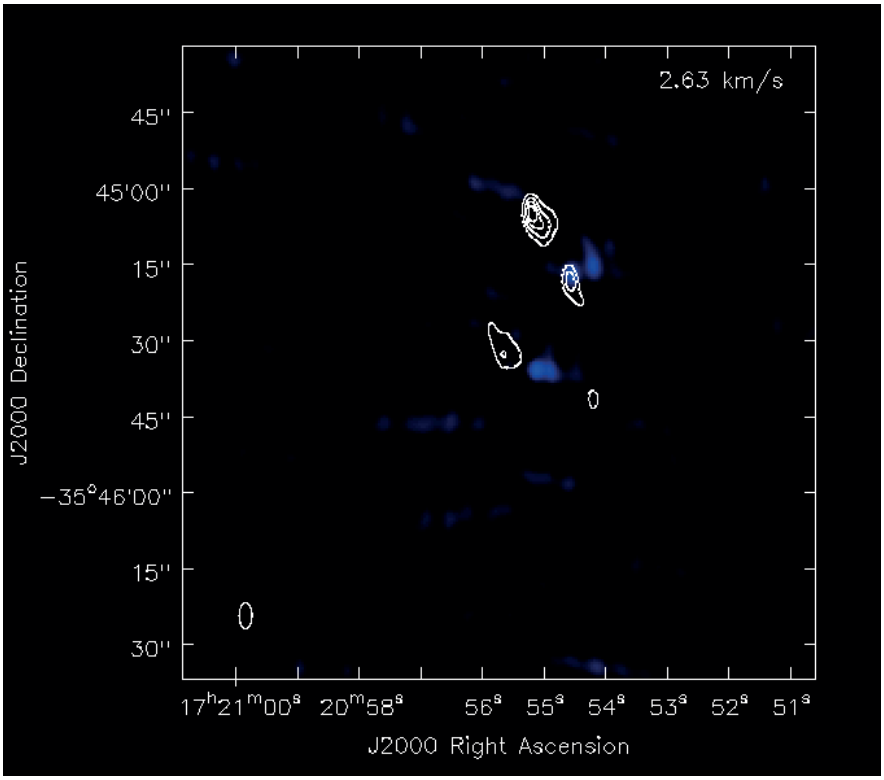

Figure 5.3: SM2 ^{13}CO millimeter line 2.63 km s^{-1} channel image - SM2 ^{13}CO millimeter line 2.63 km s^{-1} channel image, superimposed on the NGC 6334I(N) continuum contour (white contour) map.

The ^{13}CO did not coincide with the continuum cored detected in NGC 6334I(N). The line profile are complex and were strongly self-absorbed. They look very much associated with the weaker compact continuum emission northwest of the SM2.

As in the case of the ^{13}CO line, C^{18}O line was also strongly self-absorbed. They trace high density gas and these seem to be mostly associate with the SMA6, SM2, and the weaker compact continuum emission northwest of the SM2.

5.3.4 SM2 Extended Millimeter Line Emissions

H_2CO looks the most spatially extended millimeter line of SM2 spanning a velocity range $>$ 20 km s^{-1}. It traces a bipolar molecular outflow from the SM2 young stellar

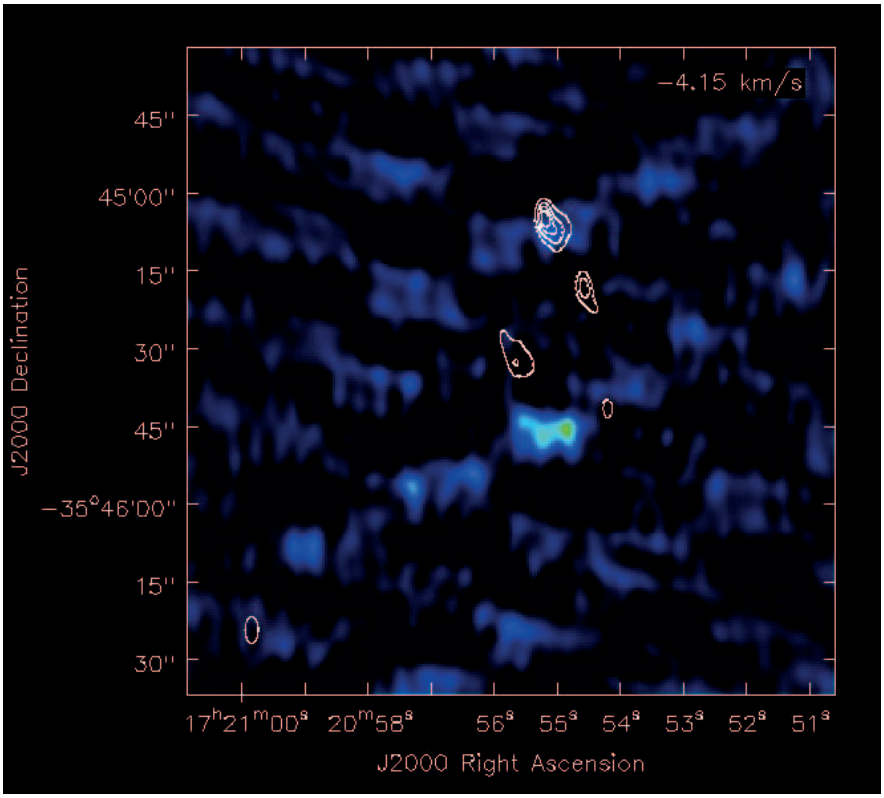

Figure 5.4: SM2 ^{13}CO millimeter line - 4.15 km s^{-1} channel image - SM2 ^{13}CO millimeter line 2.63 km s^{-1} channel image, superimposed on the NGC 6334I(N) continuum contour (white contour) map.

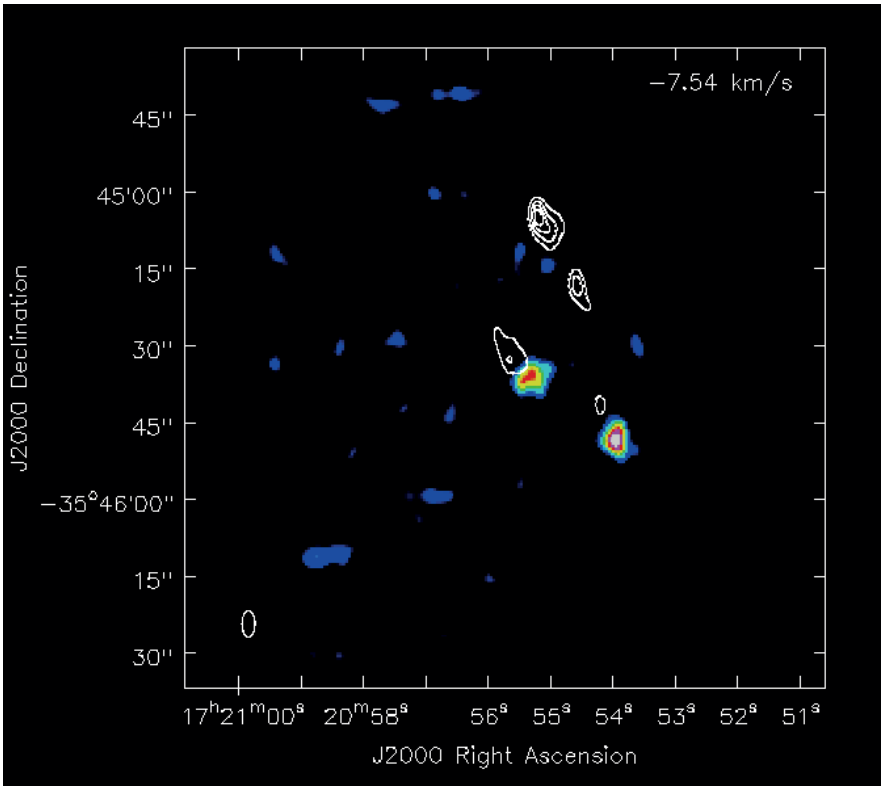

Figure 5.5: SM2 $C^{18}O$ millimeter line - 7.54 km s^{-1} channel image - SM2 $C^{18}O$ millimeter line 2.63 km s^{-1} channel image, superimposed on the NGC 6334I(N) continuum contour (white contour) map.

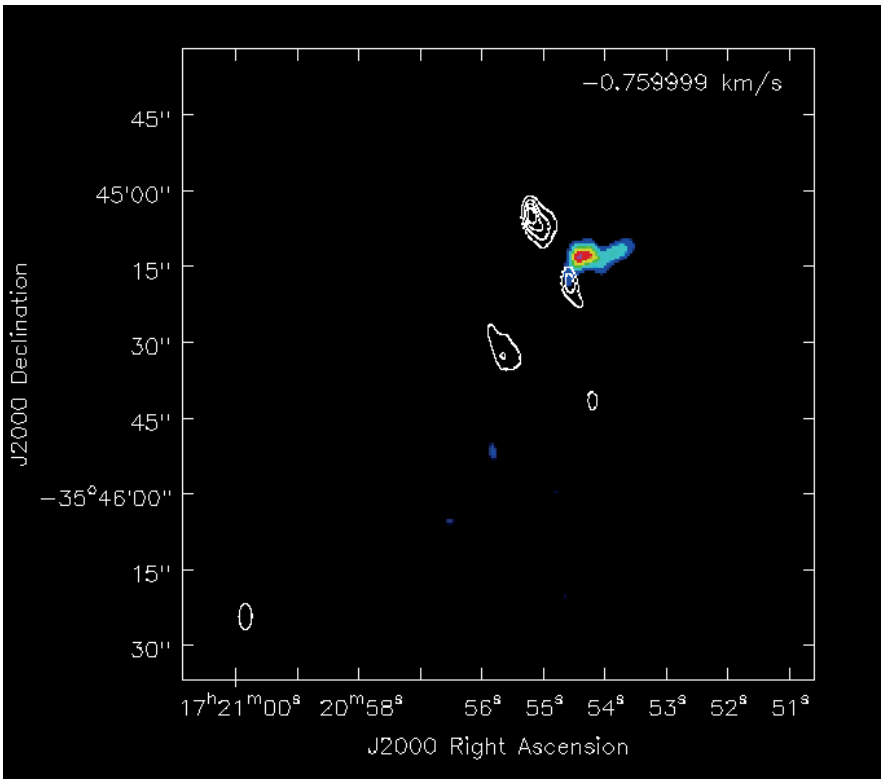

Figure 5.6: SM2 $C^{18}O$ millimeter line - 0.76 km s^{-1} channel image - SM2 $C^{18}O$ millimeter line 2.63 km s^{-1} channel image, superimposed on the NGC 6334I(N) continuum contour (white contour) map.

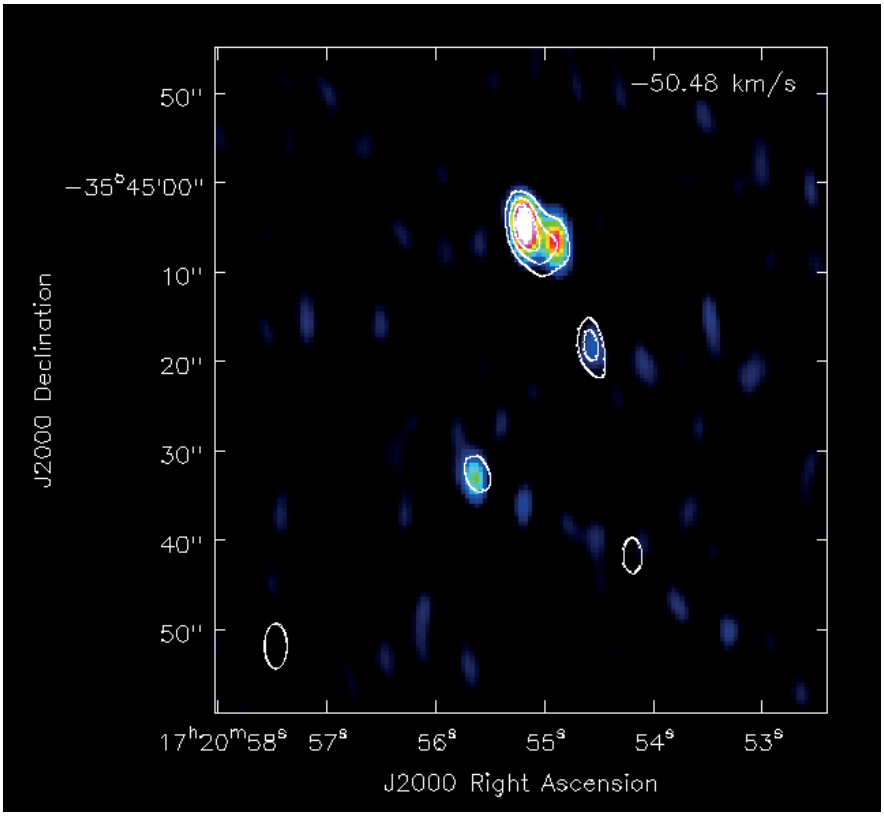

Figure 5.7: Compact CH_3CN millimeter line - 50.48 km s^{-1} channel map of the SM2 - Compact CH_3CN millimeter line - 50.48 km s^{-1} channel map of the SM2, superimposed on the NGC 6334I(N) continuum contour (white contour) map.

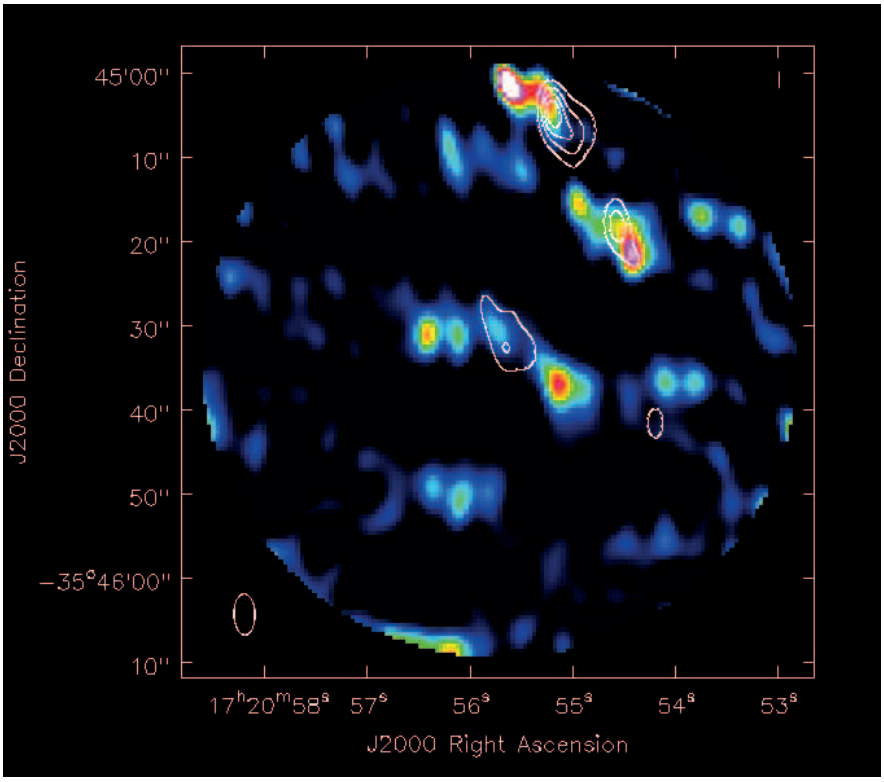

Figure 5.8: Compact CH_3OH millimeter line moment zero map of the SM2 - Compact CH_3OH millimeter line moment zero map of the SM2, superimposed on the NGC 6334I(N) continuum contour (white contour) map. The structure of the CH^3OH line map suggests it to be tracing molecular outflow from SM2.

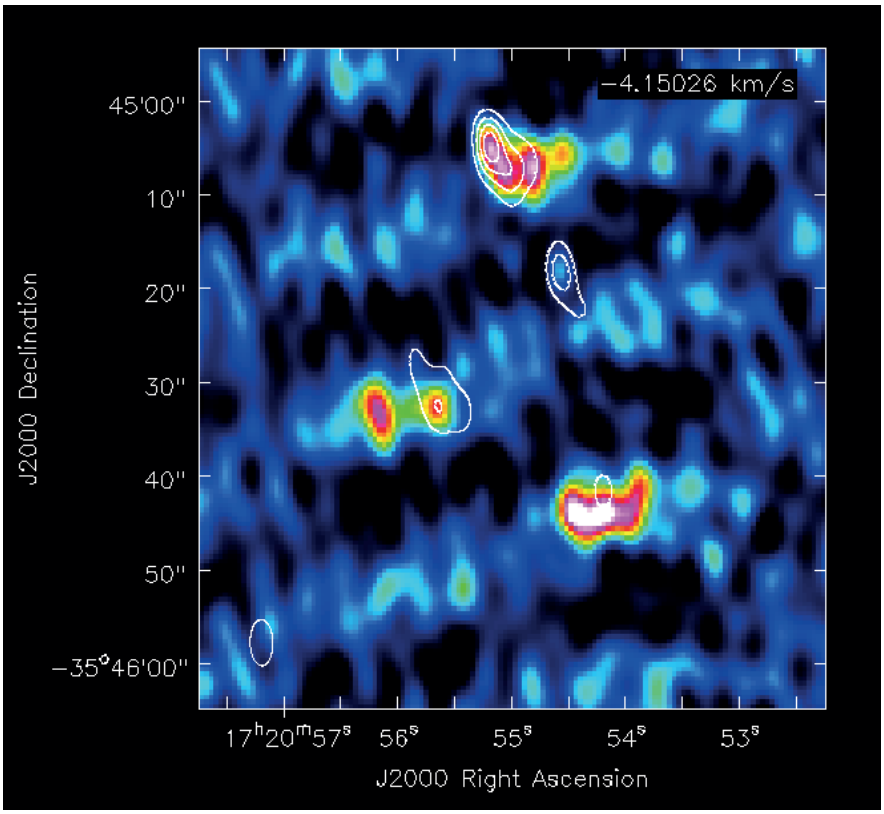

Figure 5.9: Compact CS millimeter line - 4.15 km s^{-1} channel map of the SM2 - Compact CS millimeter line - 4.15 km s^{-1} channel map of the SM2, superimposed on the NGC 6334I(N) continuum contour (white contour) map.

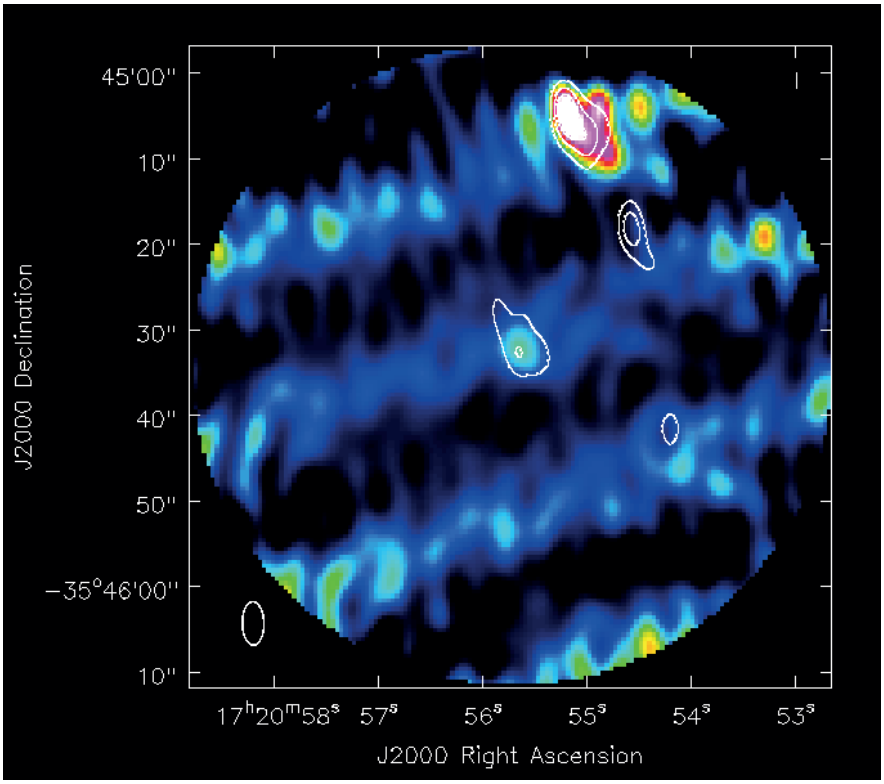

Figure 5.10: Compact DCN millimeter line - 4.15 km s^{-1} channel map of the SM2 - Compact DCN millimeter line - 4.15 km s^{-1} channel map of the SM2, superimposed on the NGC 6334I(N) continuum contour (white contour) map.

object. Figures 5.11, 5.12, and 5.13 show the image of the H_2CO line at -1.89, 0.37, and -0.76 20 km s^{-1} velocity channels. SM2 is evidently the characteristic center of the bipolar outflow traced by the H_2CO emissions. The alignment of the H_2CO outflow agree with the distribution of H_2O masers in SM2 detected in our JVN observations (see Figure 5.3). SM2 should be a young stellar object in order to exhibit outflows as traced by thermal millimeter molecular lines. This is an evidence that SM2 is not a mere clump of an ejection from a nearby high-mass star, nor a shock effect of surrounding environment.

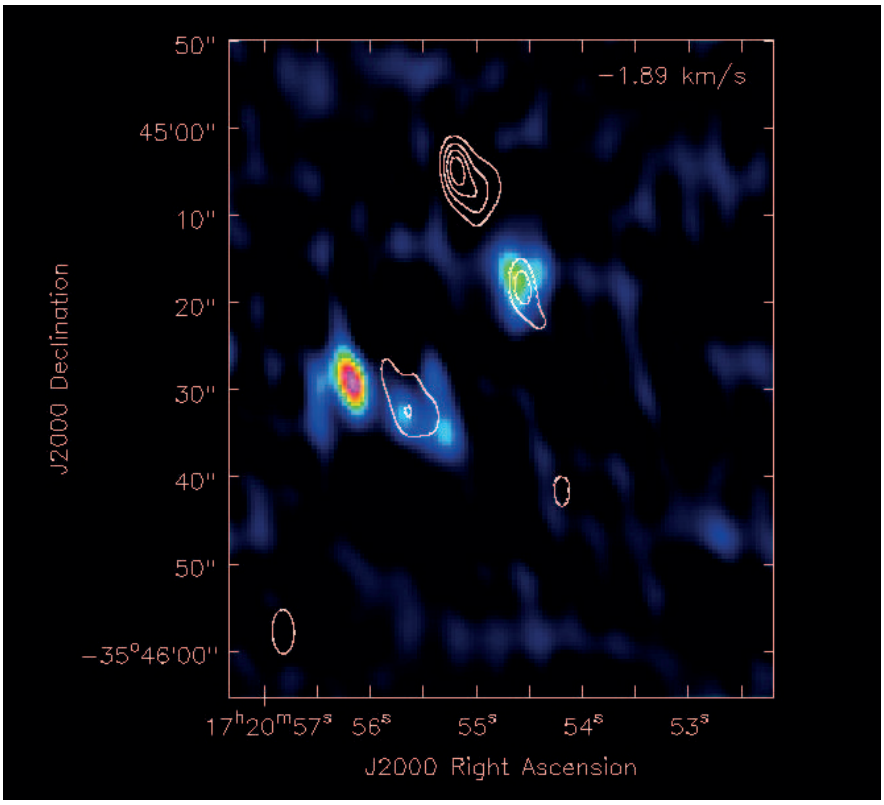

Figure 5.11: Compact H_2CO millimeter line - 1.89 km s^{-1} channel map of the SM2 - Compact H_2CO millimeter line - 1.89 km s^{-1} channel map of the SM2, superimposed on the NGC 6334I(N) continuum contour (white contour) map. H_2CO traces molecular outflow from SM2.

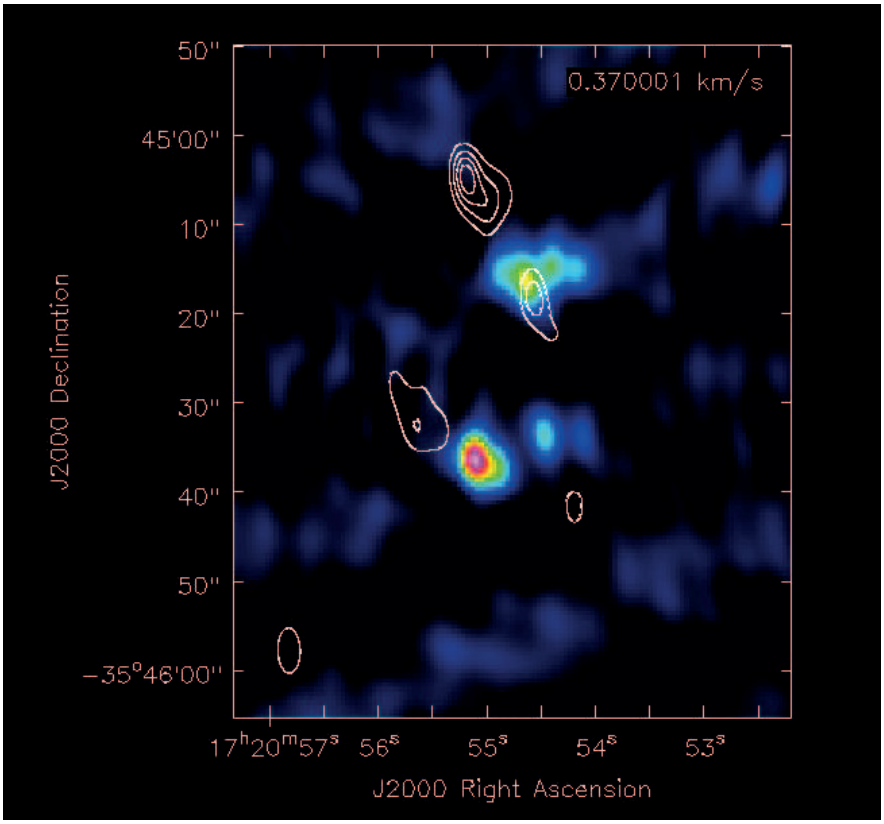

Figure 5.12: Compact H_2CO millimeter line 0.37 km s^{-1} channel map of the SM2 - Compact H_2CO millimeter line 0.37 km s^{-1} channel map of the SM2, superimposed on the NGC 6334I(N) continuum contour (white contour) map

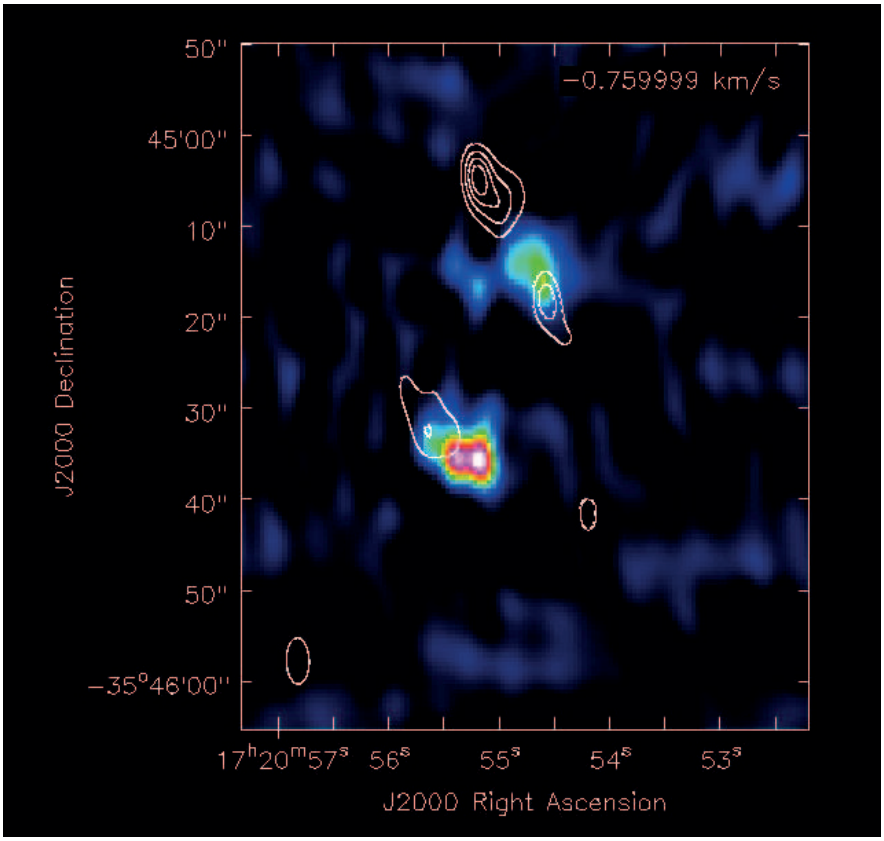

Figure 5.13: Compact H_2CO millimeter line - 0.76 km s^{-1} channel map of the SM2 - Compact H_2CO millimeter line - 0.76 km s^{-1} channel map of the SM2, superimposed on the NGC 6334I(N) continuum contour (white contour) map

5.4 Discussion

5.4.1 Hot Core Temperature Estimation from the Line Emission

It is important to measure the gas temperature of a core in order to accurately classify it. The multiple component methyl cyanide (CH_3CN) line is suitable for this purpose (Pankonin et al. 2001). Assuming double-component local thermodynamical equilibrium and the same excitation conditions of all the K components and isotope effects, we obtained the best-fit result of the methyl cyanide CH_3CN spectrum. The fitting result yielded a hot core temperature of 60 $\pm$ 10 K.

5.4.2 H_2O Maser Emission and the Evolution of a Hot Core

It is a common knowledge the H_2O masers are emitted early in the formation phases of massive stars. H_2O masers also trace activities in later phases like wide-angle outflow (e.g. Cep A HW2 reported in Torrelles et al. 2011). Comparing our results with those of Sandell (2000) and Brogran et al. (2009), we can constrain the 'early' further. Sandell (2000) reported cold sub millimeter emissions from SM2, suggesting it to be a cold core (the core which forms after a dense molecular cloud gravitationally collapses). Based on the work of Brogan and collaborators, the SM2 was not detected at 1.3mm with the SMA but was clearly associated with H_2O masers detected with the VLA at $\sim$ 22 GHz. Their results implied that a hot core had not developed in SM2 but H_2O masers were already emitted. Subsequently, we detected the millimeter continuum and lines of SM2 characterizing it to be a hot core at 60 K. Piecing together the components of the resulting puzzle, we arrive at the conclusion that H_2O masers around massive young stellar objects are pumped earlier before the formation of hot cores. This implied that between the formation of cold cores and its evolution to a hot core, conditions for masers emissions are reached and H_2O masers are pumped. This new body of knowledge will be useful in our exploration of massive star formation.

5.5 Conclusions & Summary

We conducted SMA observations at 1.3 mm centered on the SM2 object of NGC 6334IN. For the first time we detected the thermal dust continuum emission from this object,

along with a forest of millimeter lines. Using the methyl cyanide (CH_3CN) multi-component line, we did Gaussian fitting and obtained the excitation temperature of the SM2 object to be 60 K. This is an indication that SM2 is a hot core. Sandell (2000) detected SM2 with JCMT as a cold core, Hunter et al. (2006) and Brogan et al. (2009) failed to resolve the source at 1.3 mm, but detected the H_2O masers associated with it. Comparing this with our results, we concluded that between the formation of cold cores and its evolution to a hot core, conditions for masers emissions are reached and H_2O masers are pumped.

6

Spontaneous Star Formation in the Dense Molecular Cloud Associated with the Monkey Head Nebula

6.1 Introduction of the Gemini OB1 Molecular Cloud

The formation of a high-mass star leads to the ionization of its immediate surrounding and the formation of a H II region. There are many investigations on the interactions between H II regions and nearby molecular clouds. One of the classical works suggested a sequential star formation process triggered by the interstellar shock induced by the expanding H II region, to explain the formation of OB associations (Elmegreen & Lada 1977). In their work, they investigated the gravitational stability of the very dense layer of neutral gas between the ionization and shock fronts, with the aim of exploring the star formation possibilities in the layer. They referred to this layer as the cooled, post-shock layer of density $\sim 10^5$ cm^{-3}. The shock temperature of the layer will be 100 K and will radiatively cool rapidly (Aannestad 1973). The cooled molecular hydrogen, H_2, will subsequently undergo collision-based dissociation. Gravitational instability builds up in the shocked layer after $\sim 2 - 3 \times 10^6$ years (the time it takes the shock to travel 10 – 20 pc in distance) and then collapse to form stars. Based on the protostellar mass function proportionality dependence on temperature (Silk 1976), they argued that

the stars born out of the collapse would be more massive than the stars formed in the non-shocked, more remote part of the same molecular cloud. A group of OB stars are formed in the shocked layer, and the sequential process continues as the newly formed OB stars reach their main sequence phase and release ionization-shock fronts into the remaining uncollapsed molecular cloud, thus, initiating another cycle of OB star formation.

While there are some observational evidence of low and intermediate-mass star formation triggered by the influence on an expanding H II region (Deharveng et al. 2009, Koenig et al. 2008). Only a few massive stars are suggested to have formed through such a triggered process. Assuming that the Midcourse Space Experiment (MSX) identified associated embedded clusters are second generation clusters, Deharveng et al. (2005) suggested Sh 104, Sh 217 and RCW 79 to be triggering the formation of high-mass stars due to the presence of ultra compact H II regions. Thompson et al. (2012) suggested that only about 14% of the massive stars in the Milky Way could have triggered, in effect, the remaining 86% were formed through a different scenario. They also identified the phenomenological problem associated with triggered star formation studies, which is preconceived expectation that the identified young stellar objects have formed through a triggered process.

However, there are no clear observational evidence of this scenario. This is due to difficulty involved in deriving the star formation history in a single star-forming region.

NGC 2175 is a famous OB star cluster. Its central star is HD 42088 of spectral type O6.5V (Conti & Alschuler 1971, Walborn 1972), and likely a part of the Gemini OB1 (Gem OB1) association and the main ionizing star of the H II region, S252. S252 H II region was catalogued by Sharpless (1959, Westerhout 1958) and also known as the Monkey head nebula (MHN). It is located in an OB association, Gem OB1 (Morgan et al. 1953) and is suggested to be a prototypical site of sequential star formation (Efremov 1995). Its distance is estimated to be 2.1 kpc using the annual parallax method.(Reid et al. 2009). There are clear evidence of star formation activities in this region. Carpenter et al. (1995b) found that 8 of 11 dense molecular gas clumps are associated IRAS point sources and star clusters were found in some clumps through their near infrared survey. Using Spitzer IRAC and Flamingos near infrared data, Chavarria et al. (2008) identified 510 young stellar objects (YSOs) in S254 – S258 complex. They discovered 6 unknown clusters in that complex and also found that

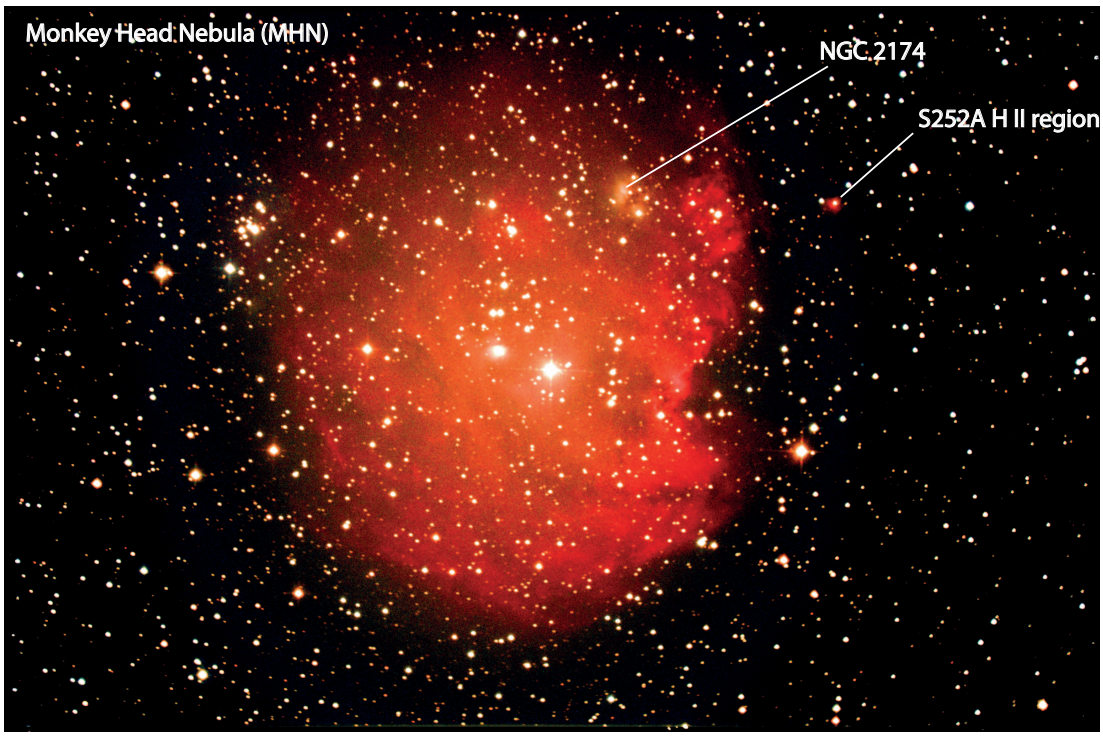

Figure 6.1: The Monkey Head Nebula - Optical image of the MHN showing the location of NGC 2174 and S252A compact H II region.

80% of the IR- excess sources are located in these clusters while the remaining 20% are distributed in a more isolated component.

The morphology of molecular cloud suggests that there is interaction between the H II region and molecular gas. Carpenter et al. (1995a) made maps in ^{12}CO and ^{13}CO lines of the Gem OB1 region with the Five College Radio Astronomy Observatory (FCRAO) 14 m telescope. Along the western edge of S252, a molecular cloud with large column density is seen in their ^{13}CO map (see Figure 6.6). In addition, they found a lot of arcs and ring like filaments, which suggests that the molecular gas may have been swept up due to expanding H II regions and wind blown bubbles. Most of the arcs and filaments show high column density ($> 10^{22}$ cm^{-2}) and a typical temperature range of 10 – 20 K.

However, to study the interaction between the H II region and the molecular cloud, investigation of the distribution of the dense gas and of the gas temperature is vital. NH_3 lines prove to be useful for investigating the physical conditions of a molecular cloud. Although Wu et al. (2010) made NH_3 line observations towards this cloud with the Effersberg 100 m telescope, they show the temperatures at three NH_3 peaks only. Therefore, we made the mapping observations in NH_3 (1,1), (2,2), and (3,3) lines and estimated the distribution of the gas kinetic temperature over the cloud. We also made observations in radio continuum in order to explore the true distribution of ionized gas free from dust extinction.

6.2 Observations

6.2.1 NH_3 Observations

In order to figure out the distribution of the dense molecular gas and its temperature, we carried out the NH_3 observations using the 34 m telescope at Kashima Space Research Center of National Institute for Communication Technology (NICT) between October 2008 and December 2010. The simultaneous observations were done in the NH_3 (J,K) = (1,1), (2,2), and (3,3) lines, whose frequencies are 23.694495 GHz, 23.722633 GHz, and 23.870129 GHz, respectively. The telescope beam size is $1'.6$. We observed 160 positions with a $1'$ grid along the equatorial coordinates over the cloud. The pointing accuracy was checked using several H_2O maser sources at 22.235080 GHz and was better than $0'.2$. We used an 8192-channel FX-type spectrometer with 256 MHz bandwidth

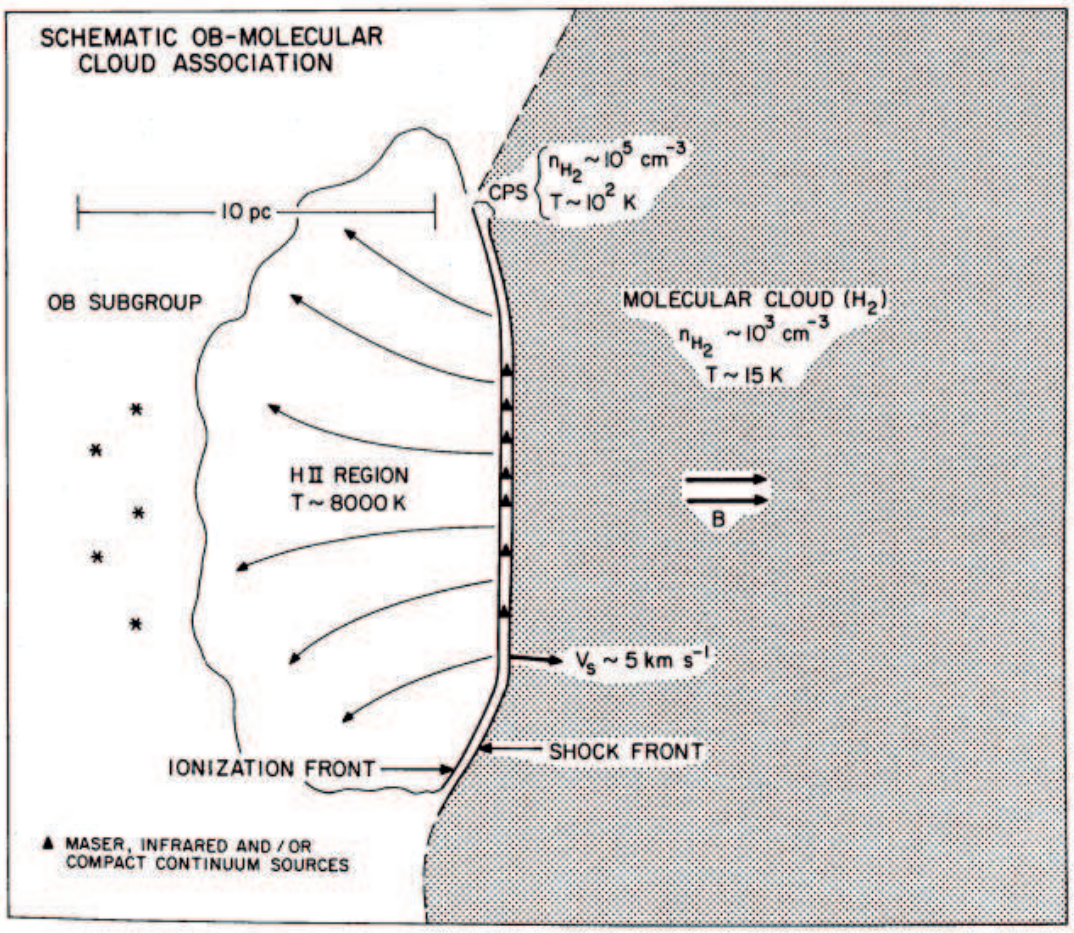

Figure 6.2: Schematic diagram of the sequential star formation scenario - Schematic diagram of the sequential star formation scenario proposed by Elmegreen & Lada (1977).

and 31.25 kHz resolution, corresponding to 3200 km s^{-1} and 0.39 km s^{-1}, respectively. All spectra were obtained with the position switch between the target source and a reference position. The reference position, where no ^{13}CO or NH_3 is detected, is $(\alpha,\delta)_{J2000}$ = ($06^h08^m26.27^s$, $20°51'10.7''$). The system noise temperature was between 170 and 350 K. We integrated longer than 20 minutes at each position. The main beam efficiency, η_{MB}, at this frequency is 0.50 ± 0.02. The resultant noise level in terms of the main beam temperature is about 0.1 K in $T_{MB} = T_A / \eta_{MB}$, where T_A is the antenna temperature corrected for the atmospheric extinction using the chopper wheel method (Kutner & Ulich 1981). We reduced the data using a software package named UltraSTAR developed by a radio astronomy group at the University of Tokyo (Nakajima et al. 2007). We applied a linear baseline to subtract the all spectra.

Figure 6.3: 34 m NICT Kashima radio telescope - Image of the 34 m NICT Kashima radio telescope used for the NH_3 mapping observations.

6.2.2 Radio Continuum Observations

The true distribution of ionized gases in H II regions can be obtained through radio continuum observations, which are not affected by dust extinction. Although the Monkey Head Nebula is visible in optical images, it might be strongly obscured by the

local dense gas. In such cases, we cannot easily conclude that the dense gas directly interacts with the ionized gas. We obtained a 1.4 GHz (20 cm) radio continuum map of the region from the NRAO/VLA Sky Survey (NVSS) with a resolution of 45″ (see http://www.cv.nrao.edu/nvss/postage.shtml). Because the NVSS map was obtained by VLA interferometric observation, the likelihood of resolving out the diffused component of MHN is very high. We, therefore, made observations at 8.4 GHz of the Monkey Head Nebula with the 32 m telescope operated by Yamaguchi University. The telescope beam size is 4′, and its main beam efficiency at 8.4 GHz is 0.70 ± 0.04. The system noise temperature was between $\sim$ 70 K, and the resultant noise level in terms of the main beam temperature is 0.04 K.

The observation was performed on January 17, 2010, over an area of 2° x 2° centering on the H II region. The raster-scan method was used: the telescope moved smoothly at fixed speed in the declination direction, and antenna temperature was measured continuously. The grid of the data was 1′ both in right ascension and declination. Since FWHM of the beam is 4.2′, it is oversampling enough and the data can be smoothed during the data analysis. The observing bandwidth was 400 MHz centered on 8380 MHz. Both left hand circular polarization (LHCP) and right hand circular polarization (RHCP) were used simultaneously. For the calibration of the flux density and the observing position, a calibrator source 3C138, $(\alpha,\delta)_{J2000}$ = ($05^h21^m09.886^s$, 16°38′22.051″) of flux 2.44 Jy at 8.4 GHz was observed with the same observation system just before observation of the H II region. The calibrator was observed for 36 minutes, followed by the observation of the H II region for 2 hours. Only the declination scan was performed due to the limited observing time. The system temperature was 50 K for LHCP and 45 K for RHCP. The observation weather was fine and wind was weak. The obtained data was analyzed using a software developed locally. In order to reduce a scanning noise, the PRESS method of Sofue & Reich (1979) was used.

6.3 Results

6.3.1 Distribution of NH_3 Gas

We observed the NH_3 lines at 160 positions in the mapping area. The NH_3 (1,1), and (2,2) were detected at 87, and 33 positions, respectively, with a signal-to-noise ratio >

3. Figure 6.4 shows the typical profiles. Both the main and satellite lines of (1,1) transition were detected at some positions, while only the main lines of (2,2) were mostly detected. NH_3 (3,3) was not detected at any position, and it will not be considered in this chapter.

In Table 6.1, we show the main beam brightness temperature T_{MB}, the peak velocity v_{LSR}, and the line width δv at the 4 positions (a, b, c, and d) shown in Figure 6.5, whose spectra are shown in Figure 6.4. The radial velocities of the NH_3 lines are between 7.4 and 8.9 km s^{-1}, which is near that of the MHN, obtained from the Hα observations (Fountain et al. 1983).

ID	RA(J2000)	Dec.(J2000)	Rotational transition *(J,K)*	T_{MB} (K)	v_{LSR} (km s^{-1})	Δv (km s^{-1})
a	$06^h\ 08^m\ 43.48^s$	$+20^\circ\ 38'\ 10.7''$	(1,1)	1.0±0.1	8.0±0.1	2.7±0.2
			(2,2)	0.4±0.1	8.3±0.2	3.1±0.5
			(3,3)	0.2±0.1	7.8±0.6	4.9±2.0
b	$06^h\ 08^m\ 30.57^s$	$+20^\circ\ 39'\ 10.7''$	(1,1)	0.3±0.1	8.5±0.1	2.3±0.3
			(2,2)	0.2±0.1	9.0±0.5	4.3±1.4
			(3,3)	...	...	...
c	$06^h\ 08^m\ 52.09^s$	$+20^\circ\ 30'\ 10.7''$	(1,1)	0.7±0.1	8.2±0.1	1.7±0.2
			(2,2)	0.2±0.1	8.3±0.1	1.9±0.3
			(3,3)	...	...	...
d	$06^h\ 07^m\ 47.54^s$	$+20^\circ\ 39'\ 10.7''$	(1,1)	0.4±0.1	7.4±0.1	1.4±0.3
			(3,3)	...	...	...
			(3,3)	...	...	...

Table 6.1: Typical NH_3 Spectra Parameters

Figure 6.5 shows the integrated intensity map of the main hyperfine component of the NH_3 line over v_{LSR} = 4 – 13 km s^{-1}. It extends over 10 pc around the northwest to southeast of the MHN (Figure 6.5 right panel). Figure 6.6 shows the integrated intensity map in the NH_3 (1,1) line superposed on the ^{13}CO (green contour; Carpenter et al. 1995a) and CS maps (blue contour; Carpenter et al. 1995b), respectively. The NH_3 emission well traces the dense molecular gas. Figure 6.7 shows the velocity channel

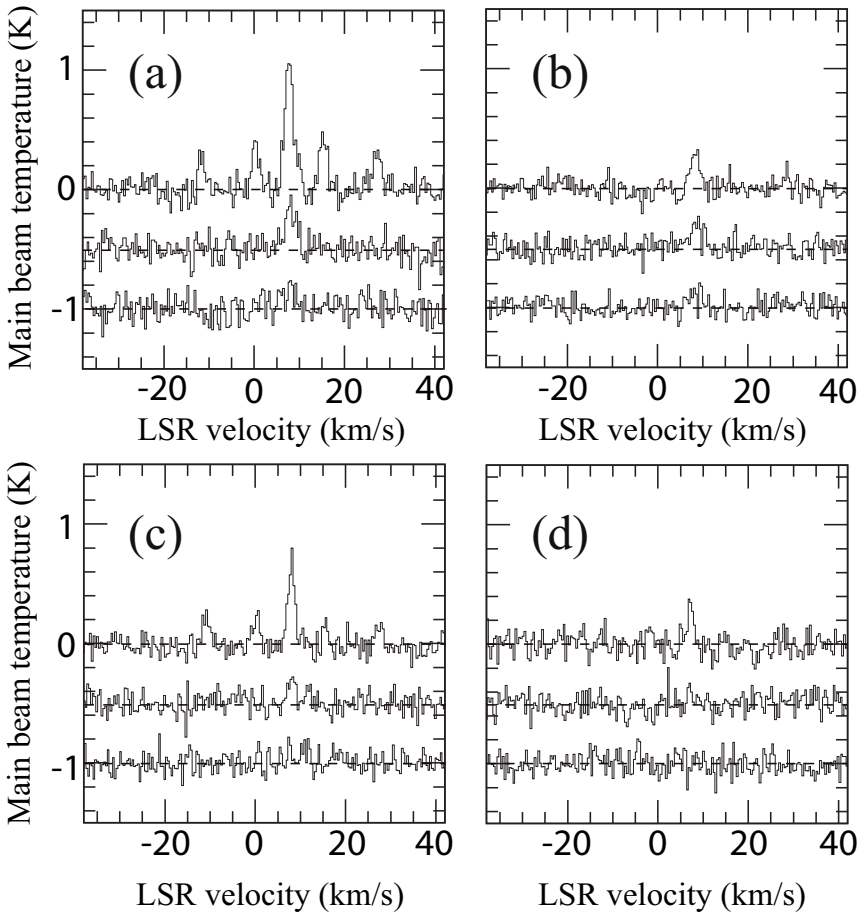

Figure 6.4: NH_3 Spectral - Typical spectra in the NH_3 (J,K) = (1,1) (top spectra), (2,2) (middle spectra), and (3,3) (bottom spectra) lines. (1,1) and (2,2) transitions were detected at some positions like (a, b & c). Only the (1,1) transition was detected at some other positions. Two pairs of satellite lines of the (1,1), the inner (satellite lines closest to, and on the both sides of the main line) and the outer (satellite lines farther away from, and on the both sides of the main line), were detected in some of the positions and weak in other positions.

maps between v_{LSR} = 6 – 11 km s^{-1} by 1 km s^{-1} step. It shows two core components are at 8 km s^{-1}.

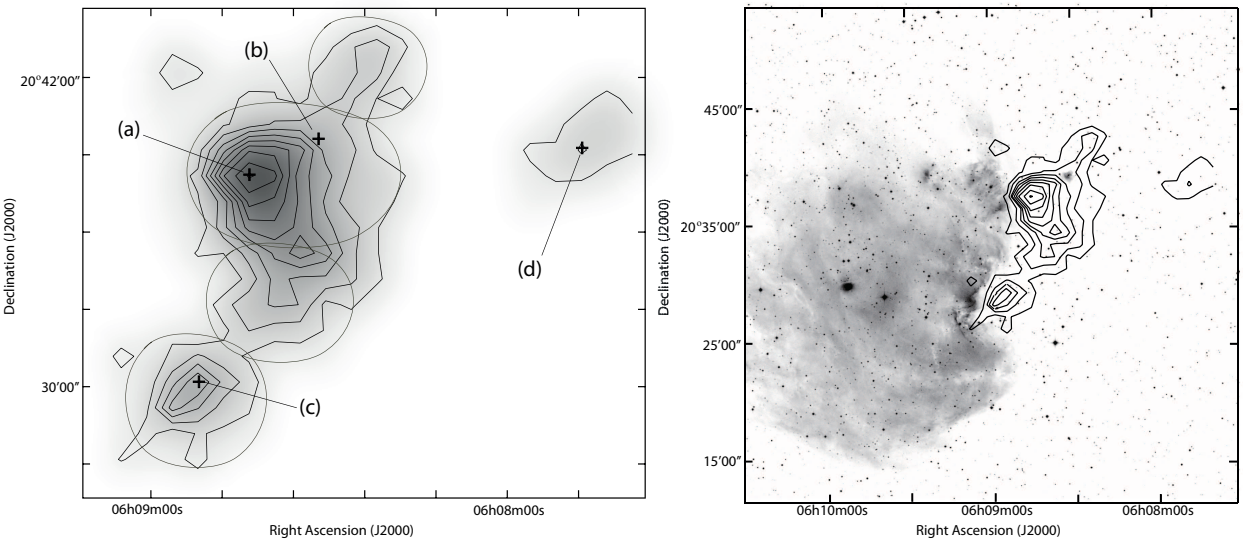

Figure 6.5: NH_3 Integrated Intensity Map - (Left) Integrated intensity map of the main hyperfine component of the NH_3 (1,1) line. Both the lowest contour line and the contour interval are 0.3 K km s^{-1}. (a), (b), (c) and (d) represent the positions where the spectra of Figure 6.4 was obtained. The inscribed gray-circled areas indicate the division of the molecular cloud into 4 parts for deriving its virial mass. (Right) NH_3 gas distribution along the edge of the ionized gas in the H II region of the MHN (Hα image).

Our radio continuum map of the H II region at 8.4 GHz shows similar morphology with the DSS image. The white contour map overlaid on our 8.4 GHz map (Figure 6.8) is the Very Large Array (VLA) map at 1.4 GHz from the NRAO/VLA Sky Survey (NVSS) . Obviously the VLA map misses the diffuse emission. The total extent of the radio continuum at 8.4 GHz is similar to that in the optical image (see Figure 6.5). It means that the optical image is little obscured even at the edge of the dense molecular cloud seen in NH_3 and well traces the whole extent of the H II region.

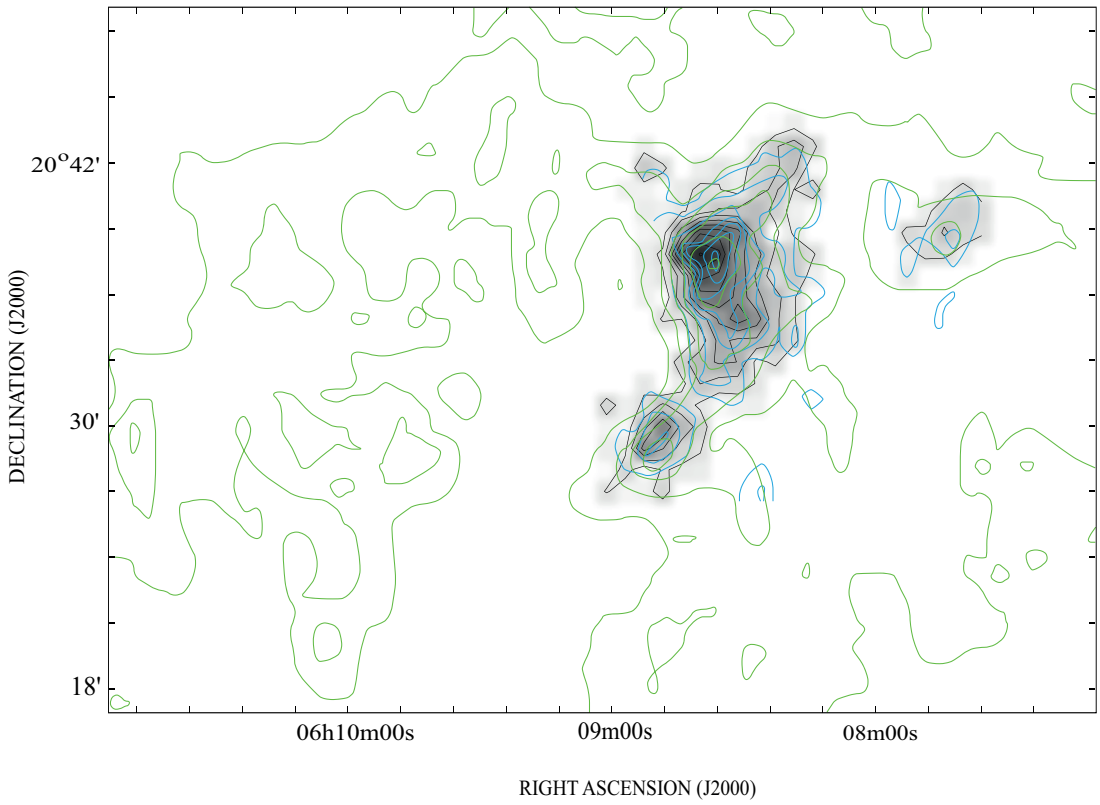

Figure 6.6: NH_3 integrated intensity map with $^{13}CO(J = 1 - 0)$ and CS maps - NH_3 (1,1)integrated intensity map (shown in Figure 6.5) overlaid on the $^{13}CO(J = 1 - 0)$ and CS map (Carpenter et al.1995a). The black contours correspond to the NH_3 (1,1)integrated intensity map, while the green and blue contours correspond to the $^{13}CO(J = 1 - 0)$ and CS maps, respectively.

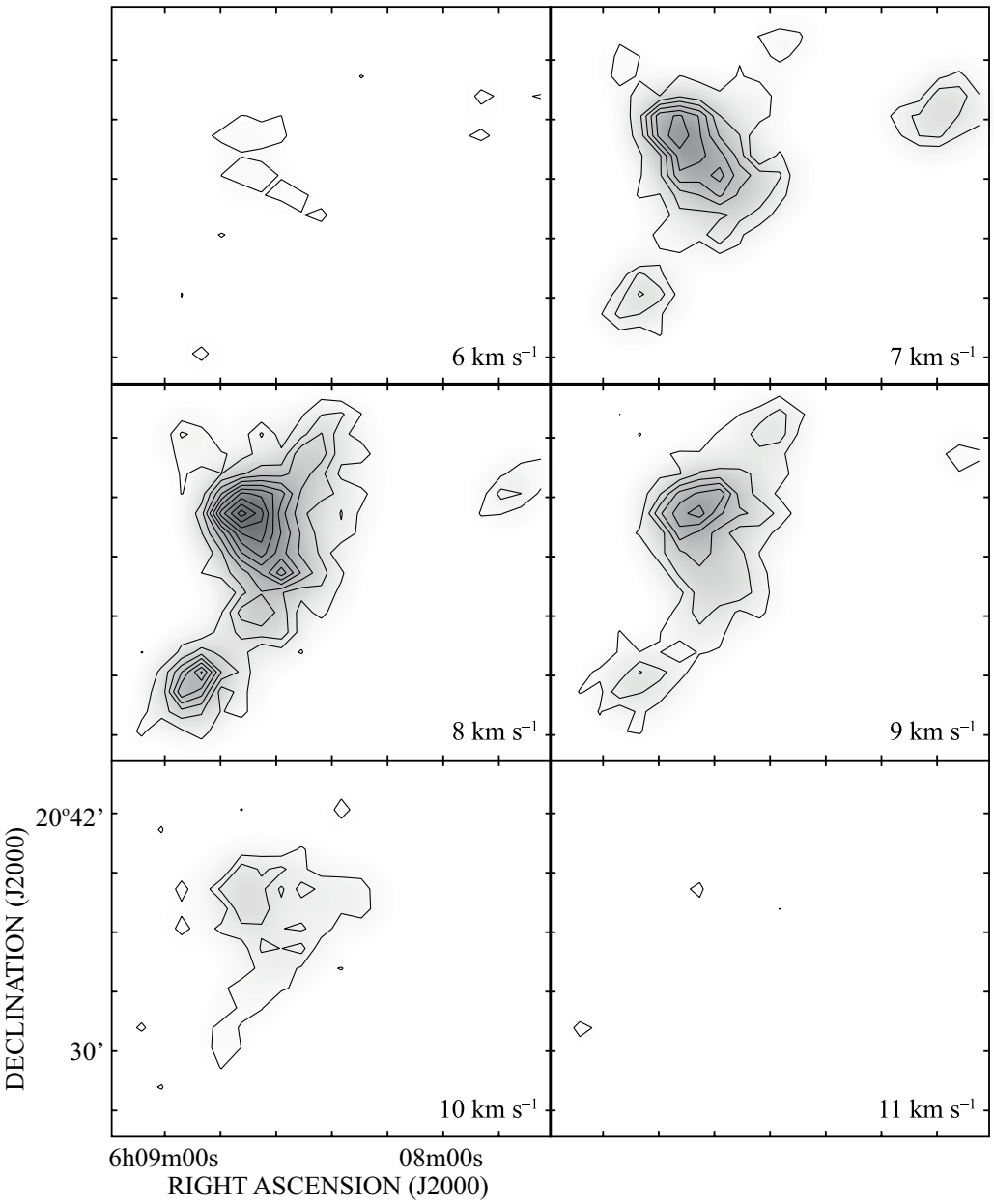

Figure 6.7: NH_3 channel map - NH_3(1,1) channel map. The lowest contour line is 0.1 K and the contour interval is 0.1 K in T_{MB}. The center velocity of each panel is shown at the bottom-right corner.

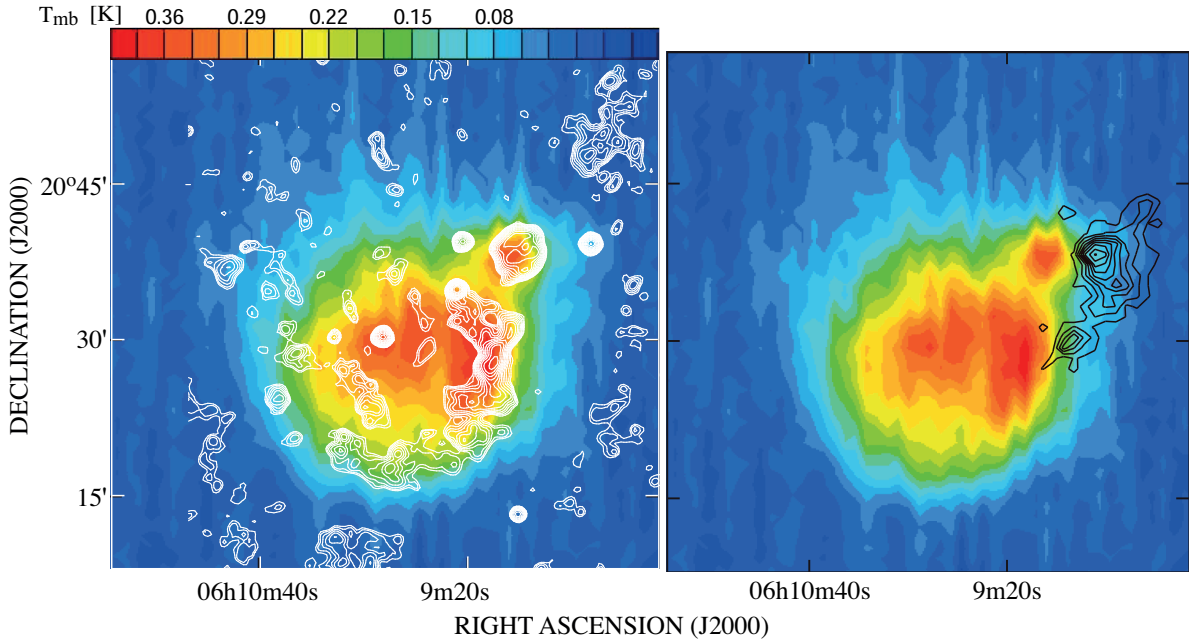

Figure 6.8: 8.4 GHz continuum map of the Monkey Head Nebula - The radio continuum map obtained with the Yamaguchi 32m telescope at 8.4 GHz in pseudo color. The color bar is shown on top of the map. The emission originates from the ionized gas in the H II region. The radio continuum emission map obtained with VLA at 1.4 GHz shown by white contours on our pseudo-colored continuum map (left). The relative position of NH_3 (1,1) map shown in black contours can be seen on the right panel.

6.3.2 Temperature Distribution in the Gem OB1 Dense Molecular Cloud

The gas kinetic temperature is important to discuss physical state of a molecular cloud. The molecular cloud we observed is located at the edge of an extended H II region. Hence, there should be variation in the gas temperature from place to place, if the H II region affects the molecular cloud.

To estimate the gas kinetic temperature, we should know the optical depth for each line of sight, which can be derived from the line intensity ratios of main and satellite lines. However, we can derive the optical depth only at some positions for the (1,1) line as shown in the previous sub-section. Therefore, we assume the optical depth is the same at all positions and $\tau = 0.9$. Figure 6.9 shows the correlation between the NH_3 (1,1) and the satellite lines, and it fittings shows τ to be typically 0.9.

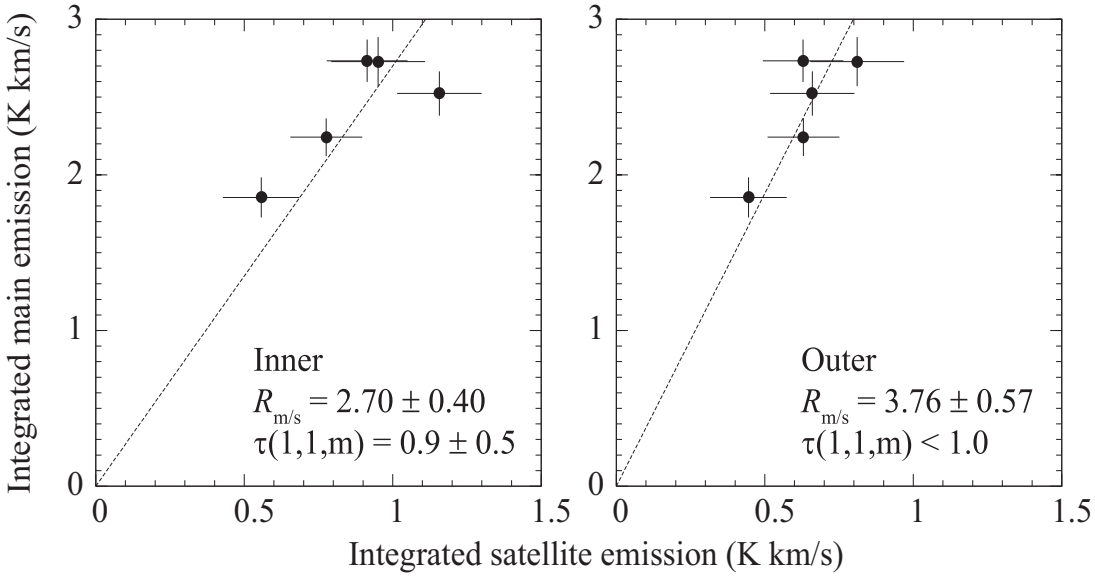

Figure 6.9: NH_3 (1,1) main line and satellite lines correlation - NH_3(1,1) correlation between the main lines and the inner and outer satellite lines (see Figure 6.4). $R_{m/s}$ is the integrated intensity ratio of the (1,1) main line to the inner and outer satellite lines.

The rotational temperature of NH_3, T_{rot}, is estimated using the intensity ratio of the (2,2) line to the (1,1) line with the estimated optical depth through the equation (1).

$$T_{\rm rot} = -41.5 \Big/ \ln\left(\frac{-0.282}{\tau} \times \ln\left[1 - \frac{T_{\rm MB}(2,2)}{T_{\rm MB}(1,1)} \times \{1 - \exp[-\tau]\}\right]\right) \quad (6.1)$$

where τ is the optical depth of the (1,1) main line, $T_{\rm MB}$(2,2) and $T_{\rm MB}$(1,1)are the brightness temperatures of the (1,1) and (2,2) main lines, respectively. We used the main beam brightness temperature as the brightness temperature. The observed ratio of $T_{\rm MB}$(2,2) to $T_{\rm MB}$(1,1) ranges between 0.2 and 0.5 at the line detected positions. Using the collisional excitation model (Walmsley & Ungerechts 1983; Danby et al. 1988) we can derive the gas kinetic temperature, T_{kin}, from T_{rot}. We estimated it at 33 positions where both (1,1) and (2,2) lines are detected over 3σ level. They are ranging between 10 and 50 K.

The histogram and distribution of the resultant gas kinetic temperatures is shown in Figure 6.10 (right panel). From Figure 6.10 (left panel), it is evident that the warmer gas are distributed around S252A compact H II region, while the rest of the molecular gas distributed even along the MHN are relatively colder than those around S252A. The histogram shows that most part of the molecular cloud temperature range from 10 – 30 K.

6.3.3 Mass of the Molecular Cloud

The mass of the dense molecular cloud is critical to estimate the star formation activity in the region. We derived the Local Thermal Equilibrium (LTE) and virial masses of the molecular cloud. The LTE mass is estimated from the line intensity with an assumption of the Local Thermal Equilibrium (LTE). Using the line intensity, optical depth, and gas kinetic temperature, we can estimate the column density through the equation (2).

$$N_{\rm TOT}({\rm NH_3}) = {\rm N}(1,1)\left[\frac{1}{3}{\rm e}^{23.4/{\rm T_{rot}}} + 1 + \frac{5}{3}{\rm e}^{-41.5/{\rm T_{rot}}} + \frac{14}{3}{\rm e}^{-99.6/{\rm T_{rot}}} + \cdots + \frac{2{\rm g_J g_I g_K}}{3}{\rm e}^{\{(23.4-{\rm E(J,K)})/{\rm T_{ro}}} \quad (6.2)$$

where E(J,K) is the energy of the inversion state above the ground state in the unit of Kelvin, g_J is the rotational degeneracy, g_I is the nuclear spin degeneracy, and g_K is the K-degeneracy (Turner 1991).

The LTE mass is given as the integration of the column density over the cloud with the NH_3 abundance X(NH_3). There are many investigations about the NH_3 abundance. Ho & Townes (1983) estimated the abundance to be 10^{-7} for the dense molecular core

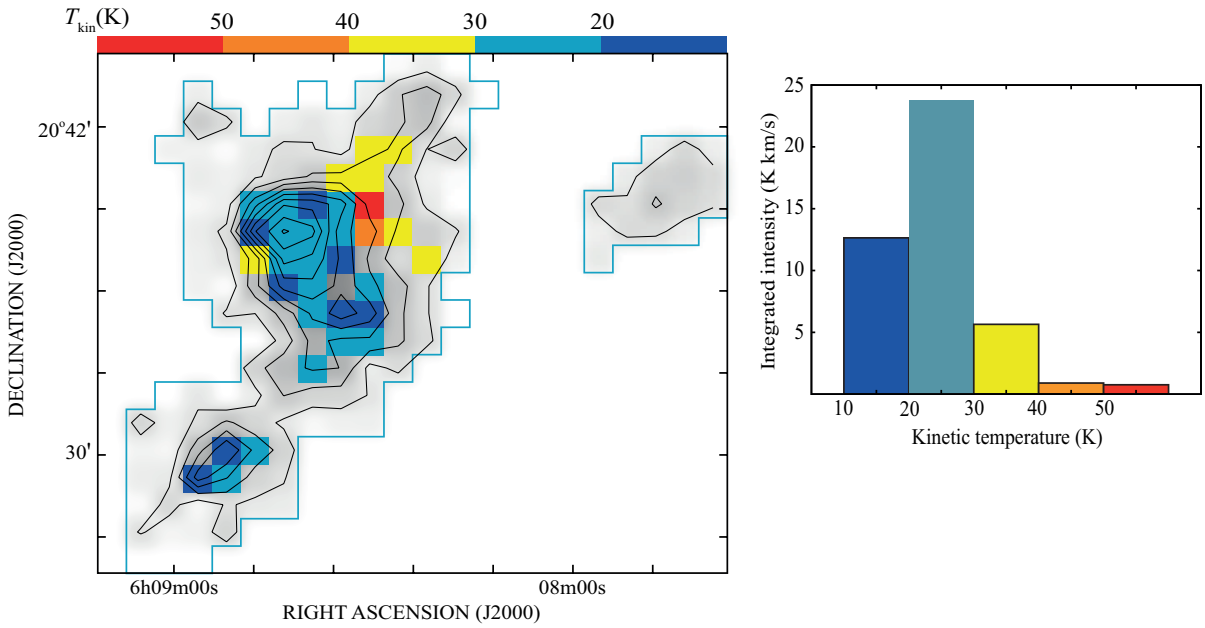

Figure 6.10: Kinetic temperature distribution - Kinetic temperature distribution in the molecular gas (left panel), and the gas temperature distribution histogram. Gases of temperature 20 – 30 K represent 84% of the entire gas, while those of 40 K and above represent the remaining 16% (right panel).

of the L183 dark core (Ungrerechts et al. 1980), and 10^{-5} in the hot core of the Orion KL (Genzel et al. 1982). Ion-molecule chemistry shows abundance to be 10^{-8} (Prasad & Huntress 1980). We assume X(NH_3) = 10^{-7} after Ho & Townes (1983). This is because our estimated kinetic temperature and the cloud size in Gem OB1 cloud are close to those of the L183. The resultant LTE mass is 1.8 $\times$ 10^3 $M_\odot$.

The virial mass is estimated from line width and cloud size with the assumption of the virial equilibrium. We used the typical velocity width of the cloud as 2.68 km s^{-1}, which is observed at the NH_3 peak. We divided the cloud into 4 parts for the purpose of deriving the virial mass (see Figure 6.5 left panel), applied the uniform sphere model (MacLaren et al. 1988), and estimated the cloud virial mass, M_{vir}, to be 1.75 $\times$ 10^3 $M_\odot$. Based both on mass estimations, we obtained mass of the molecular cloud to be $\sim$ 2 $\times$ 10^3 $M_\odot$.

6.4 Discussion

6.4.1 Star Formation in the Molecular Cloud

Two major paradigms are proposed to explain the star formation activities around a diffuse H II region; spontaneous and sequential. Spontaneous star formation is a star forming process starting from simple gravitational collapse of a dense core in a dense molecular cloud without any external trigger. Assuming Bonnell & Bate (2006) gravitational collapse and competitive accretion theory of massive star formation to be applicable in this situation, the spontaneous star formation imply that a massive star is formed by the natural, early gravitational collapse of a core in the center of a stellar cluster (the collapse is not influenced by an expanding H ll region nearby). Subsequently, it competitively accretes more materials than its counterpart by virtue of its location and early birth. Sequential star formation is a star forming process starting due to the effect of a massive star on the molecular gas, such as an expanding H II region (Elmegreen & Lada 1977; Deharveng et al. 2005) or supernova shock. The star formation around the MHN was suggested as a typical sequential star formation site (e.g. Carpenter et al. 1995b).

Figure 6.10 shows that the gas temperature on the eastern boundary of the molecular cloud is as cold as that of a typical molecular cloud or about 20 K. If the dense

cloud were formed by the shock due to expansion of the MHN, the compressed gas should be heated up.

We may say that the shock heated gas was not found, because the gas may have cooled down quickly enough to be smeared out. However, we believe that is not the case. Figure 6.10 shows the gas is as warm as 50 K at the back side of the cloud. This should not be due to the MHN. Our 8.4 GHz map shows that the extent of the ionized gas is well traced by the optical image (see Figure 6.8).

The warmest gas is $6'$ or 3.7 pc from the western edge of the MHN and beyond the main ridge of the molecular cloud. This warmest gas is located at a compact H II region, named S252A (Shepherd & Churchwell 1996; Bronfman et al. 1996). The position-velocity diagram (Figure 6.11) across the cloud in NH_3 shows a red shift at S252A. S252A is associated with an embedded star cluster and the H_2 (1-0)S1 line at 2.12 μm image shows an arc structure between the compact H II region and the molecular cloud (Tej et al. 2006). It means that the compact H II region, S252A, interacts with the dense molecular cloud. The warm molecular gas seen in our NH_3 map should be a result of this interaction.

6.4.2 Distribution of Young Stellar Objects

To investigate the star formation activities in the region, we should explore the distribution of young stellar objects (YSOs) in it. This was obtained from the point source catalog (PSC) with Wide-field Infrared Survey Explorer (WISE) archived at the NASA/IPAC Infrared Science Archive operated by the Jet Propulsion Laboratory (JPL).

This catalog covers the whole sky in 4 bands: 3.4 μm (Band 1), 4.6 μm (Band 2), 12 μm (Band 3), and 22 μm (Band 4). The angular resolutions are $6.1''$, $6.4''$, $6.5''$ and $12.0''$ for Band 1 to 4, respectively. We searched the WISE/2MASS sources centered at $(\alpha, \delta)_{J2000} = (06^h09^m06.00^s, +20°33"00.0")$ within $40' \times 40'$ area. We found about 5927 unclassified point sources from the catalog.

In order to classify the obtained point sources in class I and II YSOs, we employed the procedure shown in Koenig et al. (2012) which adapted a classification scheme developed by Guthermuth et al. (2008, 2009). This procedure includes the rejection of extragalactic sources, shock emission blobs, and resolved structures. Using the WISE band 4 or 22 μm and positionally associated 2MASS K_s band data, we retrieve some of

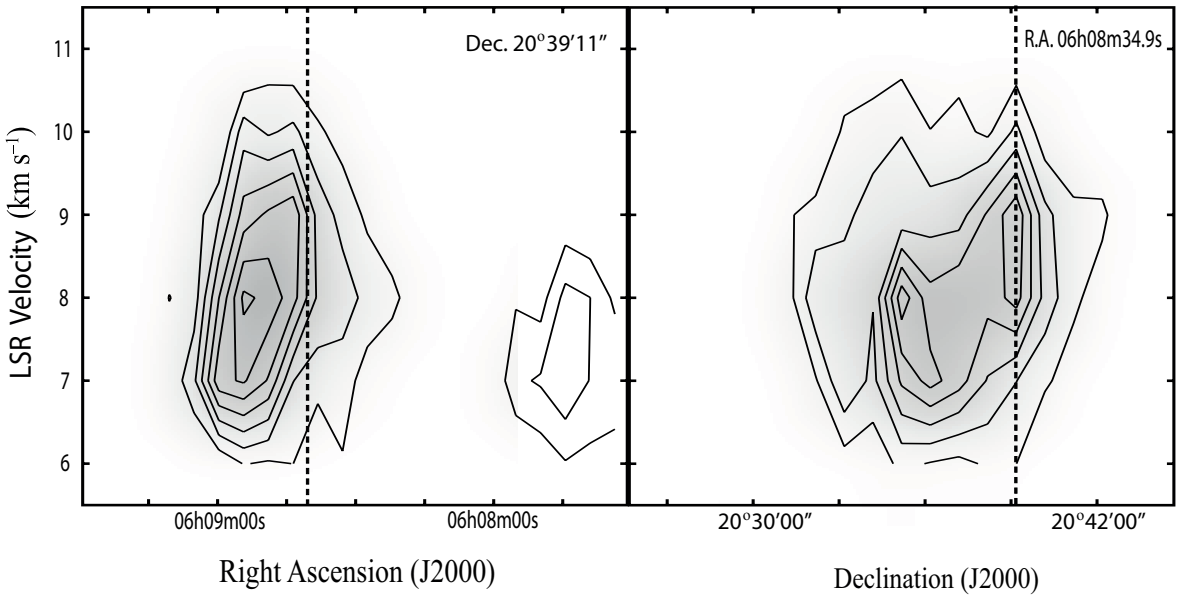

Figure 6.11: Position-velocity diagram - Position-velocity diagram obtained from the right ascension and declination slice at the highest temperature region around S252A. The dashed lines indicates the position of the slice and the existence of contour lines on both sides of the dashed lines indicate red and blue shift.

the reddened class II objects from transition disks, which are disks having photospheric color between 3.4 μm and 12 μm but an excess at 22 μm, following the procedure in the Appendix of Koenig et al. (2012). While Guthermuth and collaborators, as well as Koenig and collaborators made extinction maps to deredden the sources, we used the extinction value from the extinction map based on the 2MASS PSC by Dobashi (2011).

The classification procedure gave rise to 175 class I, 268 class II YSOs, and 15 transition disk sources. Before delving into our analyses and classification of the YSOs, we want to note that we assumed the YSOs to be of low and intermediate masses. There may be a few massive protostars among them but the number is insignificant and does not alter the overall judgement based on the YSO distribution. Our judgment is supported by the 2MASS Color-Magnitude diagram of WISE selected YSOs (Class I, Class II, and Transition disk). The total number of YSOs with 2MASS J and H-band data is 253. You can see that 155 (about 60%) of WISE selected YSOs is of mass, M $>$ 2 $M_\odot$, we adopt the 3 Myr evolutionary track by Siess et al. (2000). Stars with M $>$ 3 $M_\odot$ have already entered the main sequence at 3 Myr (see Figure 6.12) and thus should be visible in the optical if they are massive as they would have formed compact H II regions. Minier et al. (2005) reported two methanol maser around the region associated with MSX sources. We have also checked the MSX catalog of the region and found some YSOs detected to be associated with the bright H II regions and the intermediate mass stars.

The distribution of all the obtained YSOs is shown in Figure 6.13. We can find both class I and II YSOs everywhere over the observed region, although some are concentrated around the compact H II region S252A, and around S252C (Felli et al. 1977), the bright Hα condensation east of S252A, which is associated with the NGC 2175H134 O6V star (Haikala 1994), as well as around the ultra-compact H II region coincidding with the position of the small NH_3 located west of S252A, corresponds to IRAS 06047+2040 in position.

These YSO-concentrations should be made due to triggered star formation by these three H II regions. However, other YSOs are distributed rather uniformly. If most of the stars in this region were formed by expansion of MHN, these YSOs would show shell-like distribution after the propagation of star formation activity. A lot of YSOs beyond the dense molecular cloud cannot be made by the assumed expanding shell, because the shell should be located near the molecular cloud. Moreover, we cannot

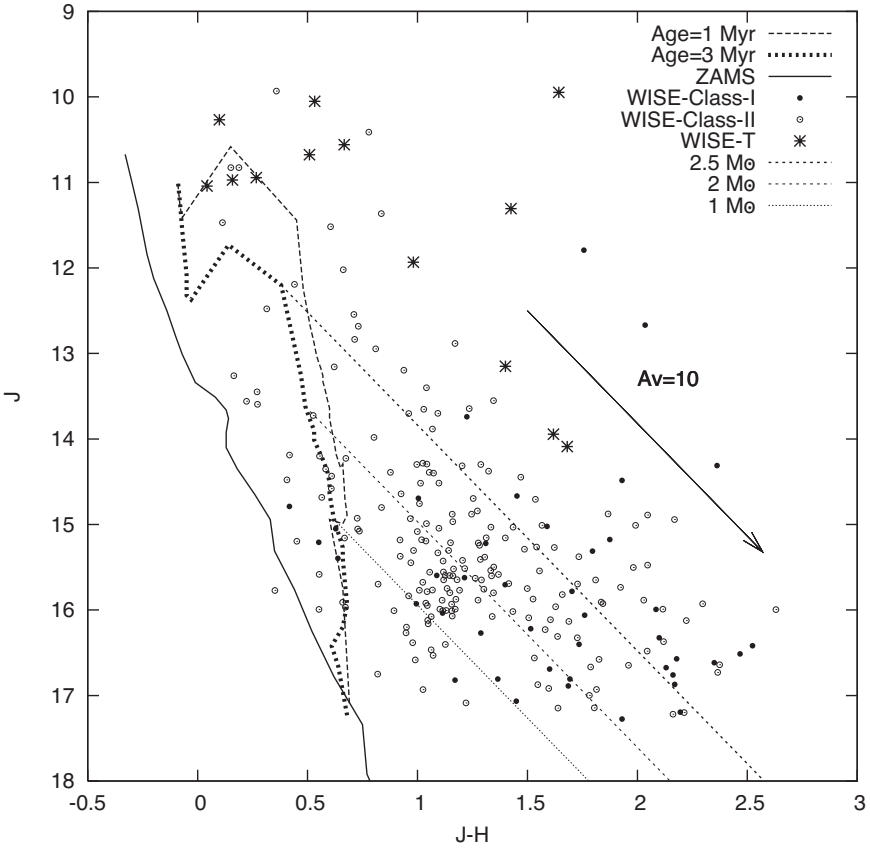

Figure 6.12: 2MASS coolr-magnitude diagram - 2MASS color-magnitude diagram of the WISE-selected YSOs in the Gem OB1 cloud. ZAMS line is the zero age main sequence line, while the WISE-T are the WISE-selected transition stars. Most of the YSOs lie on the right side of the 3 Myr line.

find any systematic age difference of YSOs over the region. All these results reject that these YSOs are made by an expanding shell associated with MHN. They should have been formed randomly. This means that most of the YSOs in this region are made spontaneously.

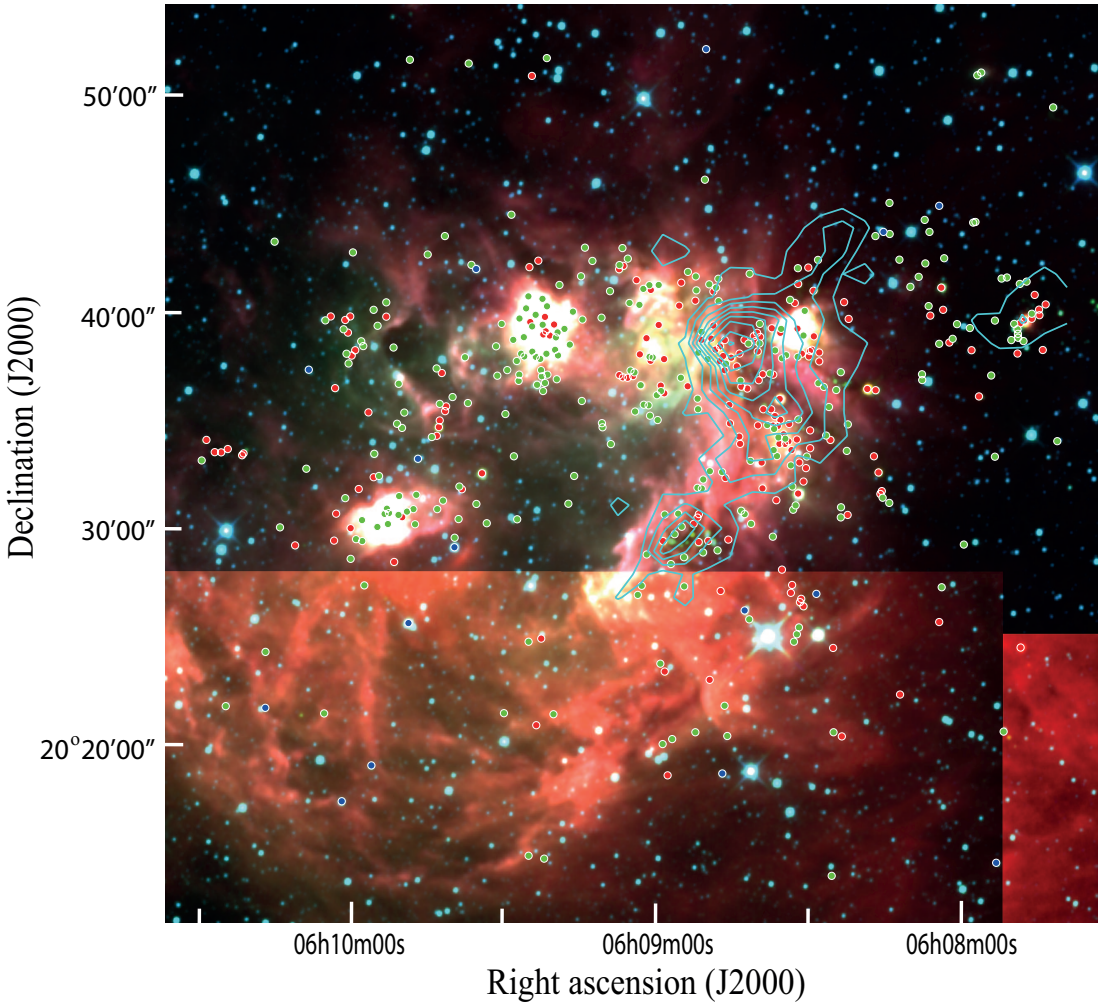

Figure 6.13: YSO distribution in the MHN - Distribution of the WISE/2MASS class I (red filled circles) and II (green filled circles) YSOs with NH_3 (1,1) contour map overlaid on the WISE image of the region.

6.4.3 Evidence of Small-scale Triggered Star Formation

We found that neither molecular gas nor YSOs in the MHN region show any systematic evidence of large-scale triggered star formation due to MHN. It means that the sequential star formation does not take place there. However, we cannot discard all triggered star formation activity in this region.

We found temperature enhancement in the molecular gas associated with the compact H II region, S252A (Figure 6.10). From the WISE archive data, we found there are YSO concentrations in the compact H II regions (Figure 6.13). Tej et al. (2006) found a bow shock associated to S252A in the shock molecular hydrogen line. The shock is located toward the dense molecular cloud. Bonatto & Bica (2011) suggested that the embedded star cluster in S252A should be made in coeval star formation event with ±5 Myr and extended for about 10 Myr and the cluster should be made after the single star formation event. Our WISE/2MASS results support this, because we did not find any hierarchal distribution of the class II and class I YSOs, which should have been an evidence of their formation occurring due to two different events separated by a time lag.

All these results show that there is some effect of an expanding H II region on nearby molecular gas. However, it is very limited both in spatial and mass scales. The warmest part of the dense molecular cloud is 0.9 pc apart from S252A. The molecular gas temperature map (Figure 6.10) shows the warmest gas size is smaller than our beam size or 0.9 pc at the distance to MHN. Therefore, we conclude the expanding H II region affects as large as 0.9 pc of the nearby molecular cloud. We found YSO concentration around two compact H II regions. However, all these YSOs are less massive ones and we cannot find any massive YSOs associated with these compact H II regions.

6.4.4 OB Star Formation Scenario in the MHN

If the effect of MHN on the surrounding interstellar matter is limited, how should we explain the association of the dense molecular gas and MHN? Our radio continuum mapping shows that the H II region and the dense molecular cloud are physically in contact; it is not an apparent association on the same line of sight by chance nor apparent by extinction due to the dense molecular cloud.

We propose that the dense molecular cloud is not formed by expansion of MHN but was pre-existing before MHN expansion caught with it. At that time there are several dense gas cores in this region. At first the most massive core collapsed and became an O6.5V star HD 42088 which is the exciting star of whole MHN (Haikala 1994). Although expansion of the H II region affected the interstellar matter around it, its effect was limited. About 1 Myr later, some cores collapsed spontaneously and formed some compact H II regions in this region. S252A is among youngest of them. During this short time scale, simultaneously, a lot of YSOs were formed from the dense gas cloud.

This scenario can also explain why the dense molecular cloud is located only in the north-western edge of MHN. Figure 6.6 shows that MHN edge is less associated with the ^{13}CO map morphologically. We observed no significant emission in NH_3 line at a few positions of these ^{13}CO peak, for example at $(\alpha, \delta)_{J2000} = (06^h09^m26.51^s, +20°39'10.70")$ and

6.5 Conclusions & Summary

We presented the results of our NH_3 emission and dust emission towards the MHN. From our observations we have obtained the physical parameters and temperature distribution of the dense molecular gas distributed northwest to southeast of the MHN. Evidently, the region around S252A compact H II region has higher temperatures compared to the rest of the molecular gas including the interface between the dense molecular cloud and MHN. And this is due to the heating effect of the radiation wind from the exciting star of S252A compact H II region and does not seem to have anything to do with the extended H II region of the MHN. We have also explored the star formation scenario in the region and argue that the OB stars in the region form spontaneously rather than sequentially due to the effect of the expanding H II region.

The molecular gas region traced in our NH_3 observations should have been originally formed and spontaneously collapsed leading to the formation of stars rather than the idea of sweeping together materials and then triggering star formation.

The overall distribution of low and medium mass stars obtained with WISE/2MASS (see Koenig et al. 2012) in the region supports spontaneous star formation scenario. However, localized triggered formation of low and medium mass stars around the S252A

compact H II region and two other H II regions are favored by our WISE/2MASS results. Though triggered star formation may be happening in limited portions of the entire region, we do not think that the triggering process is responsible for the formation of the massive OB stars in the Gem OB1.

6. SPONTANEOUS STAR FORMATION IN THE DENSE MOLECULAR CLOUD ASSOCIATED WITH THE MONKEY HEAD NEBULA

7

Evolutionary Phases of Massive Stars & Formation Scenario

In this chapter we will focus on two fundamental mysteries of massive star formation, namely, its evolutionary sequence and the scenario of formation. The redefinition of the evolutionary sequence is based on maser studies and sure incomplete considering that maser are excited only under special conditions obtainable only in a relatively small area in massive star-forming region. Yet, we can glean quite a good number of useful and some new information for the sequence described in §7.1. In §7.2, the spontaneous formation scenario proposed in Chibueze et al. (2013) is explained as against the Elmegreem & Lada (1977) sequential star formation scenario. This is based on the observational results we have obtained from the dense molecular cloud associated with the MHN as shown (in details) in Chapter 6.

7.1 Evolutionary Sequence of Massive Star Formation

In this section, we will focus on the description of the evolutionary sequence of massive star formation. In this description, the processes leading to the formation of the natal environment, the dense molecular cloud, will not be considered, therefore, the description will begin with the assumption that the dense molecular cloud is already formed, so starting from the dense molecular cloud, gravitational instabilities set in, probably due to the volume density distribution of the Dense molecular cloud (hereafter referred to as DMC) or the influence of dark matter around the DMC.These gravita-

tional instabilities leads to the collapse of the DMC and the consequent formation of cold cores (simply regions of high number density but relatively similar temperature as the rest of the DMC $\sim$ 20 K).The high density in the cold cores translate into high pressure in the cores which give rise to increase in temperature in the cores but prior to the formation of relatively higher temperature hot cores, conditions favorable for the emission of masers are reached and masers are emitted (see Chapter 5 for details). A typical case is the SM2 maser emissions which was reported in Brogan et al 2009 prior to the resolution of the hot cores in SM2. Also, before the formation of the hot cores there are turbulent instabilities in the central region of the cold cores and these can be traced by the emitted masers in the region. Examples of these periodic ejections can be found in the Cepheus A R4, R5, maser clusters reported in Torelles et al 2011.Then the hot cores appear, at this point an accretion disk begins to develop around the massive young stellar objects (hereafter referred to as MYSOs), simultaneously during the formation of the disk ,hyper-compact HII regions are formed (Beltran et al 2006). The disk assists accretion of materials into the central MYSOs and has been argued to support very high accretion rates. During accretion the hyper-compact HII region gradually expands due to the emission of ionizing photons, and form ultra-compact H II regions of temperature $\sim$ 100 K and size 0.1 pc. The ultra-compact H II region continues to expand as the MYSO evolves and emits more energetic photons.

Accretion of matter into the MYSO continues and a high velocity ($\sim$ 500 km s^{-1}) jet is formed (Patel et al. 2005). It was only in the recent past that the disk around MYSO has been resolved, before then, jets are known to be footprints of the existence of the disk-YSO in a star-forming region. Centimeter continuum VLBI observations can be used to study the jet-systems in YSOs. H_2O masers can trace their path at lower velocities. Jets are usually collimated. Low velocity bipolar outflow are formed most likely due to the influence of the high-velocity jet. Depending on the condition of the YSO's surrounding cloud, the jet from the YSO is expected to shock the environment and excite maser emissions. The masers excited close to the jet have relatively higher velocity and trace a highly collimated bipolar outflow, over time, this jet influence spread over a wider area, causing what we now know as wide-angle outflow (Torrelles et al. 2011; Chibueze et al. 2012). At this point the MYSO is already 'mature' enough to enter the main sequence phase, while still actively accreting material, and having an evolved H II region.

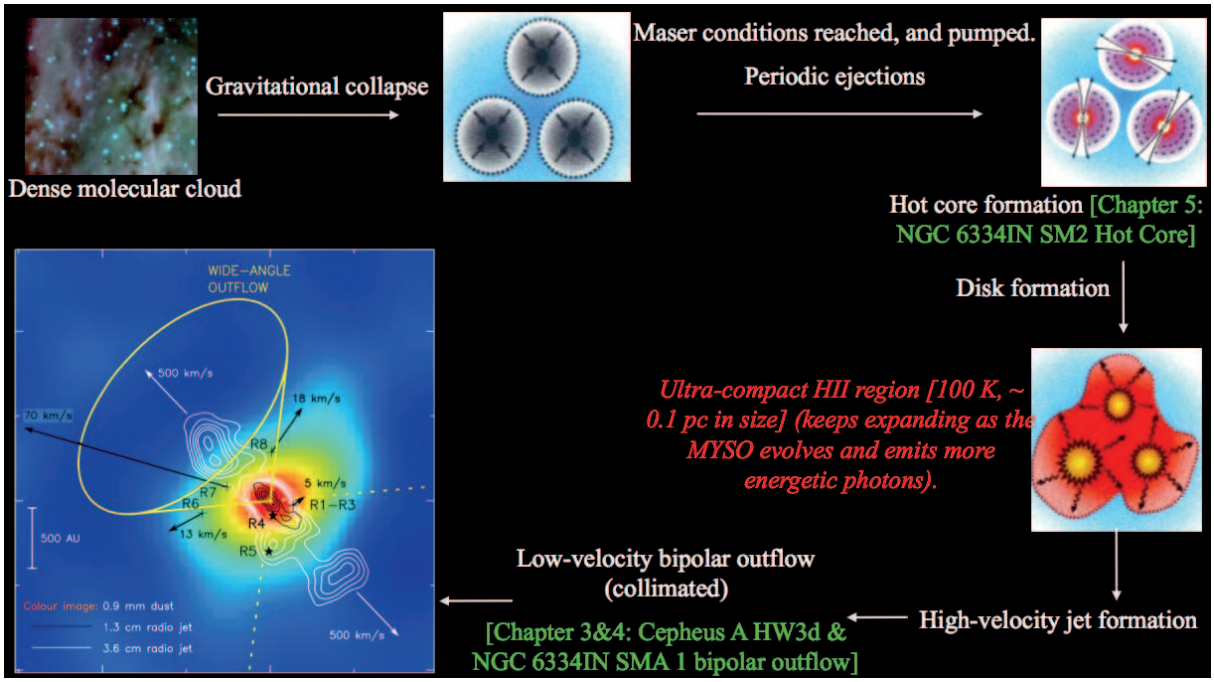

Figure 7.1: Schematic diagram of the redefined evolutionary sequence of massive star formation - Schematic diagram of the redefined evolutionary sequence of massive star formation using H_2O spatio-kinematics.

7.2 Scenario of Massive Star Formation - Sequential or Spontaneous?

Spontaneous formation scenario simply implies formation of high-mass stars through the gravitational collapse of the molecular cloud without the influence of its nearby environment. This is based on our recent observational test of the sequential star formation proposed by Elmegreen & Lada (1977). We estimated the physical parameters and temperature distribution of the dense molecular gas distributed northwest to southeast of the MHN using NH_3 line observations and dust emission observations to trace the true distribution of the ionized gas in the MHN without dust extinction. Evidently, the region around S252A compact H II region has higher temperatures compared to the rest of the molecular gas including the interface between the dense molecular cloud and MHN. And this is due to the heating effect of the radiation wind from the exciting star of S252A compact H II region and does not seem to have anything to do with the extended H II region of the MHN. We have also explored the star formation scenario in the region and argue that the OB stars in the region, especially the massive star associated with S252A, form spontaneously rather than sequentially due to the effect of the expanding H II region. The molecular gas region traced in our NH_3 observations should have been originally formed and spontaneously collapsed leading to the formation of stars rather than the idea of sweeping together materials and then triggering star formation (see Chapter 6 for details of these results).

Thompson et al. (2012) suggested that only about 14% of the massive stars in the Milky Way could have triggered, in effect, the remaining 86% formed through a different scenario. We are of the opinion that a large fraction of the 86% are formed spontaneously. The influence of an expanding H II region may vary depending on the number of OB stars in the association, and the photons emission rate. From our observational results shown in chapter 6, such influence may be limited to ~ 4 pc from the edge of the H II region, and at best triggered only localized low- and intermediate-mass stars. Our newly proposed scenario is figuratively explained in Figure 8.2.

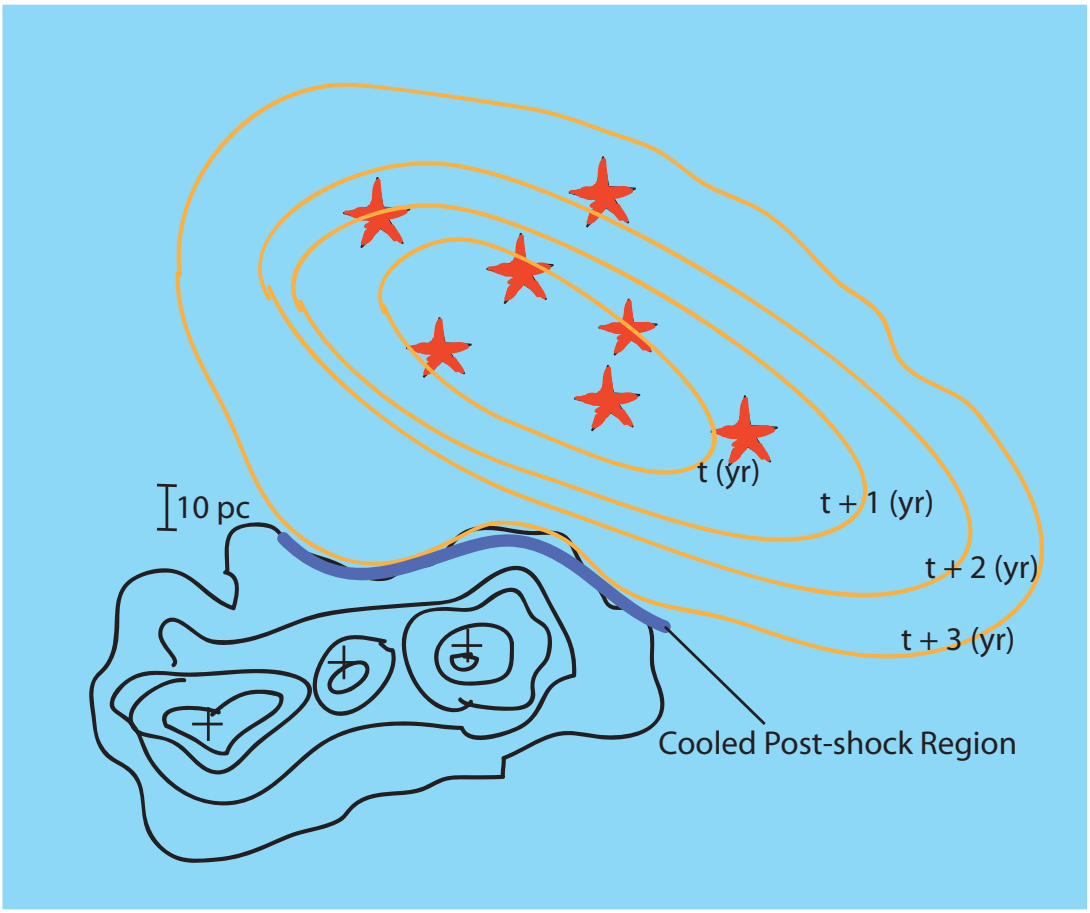

Figure 7.2: Schematic diagram demonstrating the spontaneous scenario of massive star formation - Schematic diagram demonstrating the spontaneous scenario of massive star formation. The red stars represent the OB association stars, which are ionizing their surrounding, while the orange contours represent the time-dependent expanding H II region. The black contour represents the dense molecular cloud and the crosses are the positions of the evolved massive stars with visible compact H II regions. The influence of the expanding H II region are limited to less than 4 pc from the cooled post-shock region or interface, thus not causing the birth of the 3 stars in the dense molecular cloud.

7.3 Future Works

7.3.1 Testing the Merger Theory in NGC 6334I(N) Using Atacama Large Millimeter Array (ALMA)

I plan to conduct ALMA band 7 (345 GHz) high resolution study of NGC 6334I(N). This would not only be a good follow-up of previous SMA observations towards this massive star forming region, but also a promising means of testing the merger theory of massive star formation. This is possible because ALMA will provide us with more sensitivity and higher resolution so as to detect and distinguish yet undetected sources, study their spectral indices and kinematics. We would also be able to estimate the dust temperatures of the MYSOs, as well as study the velocity dispersion of the sources detected in the region. This will provide a clue into the scenario responsible for the formation of high-mass stars in the region, and will help us estimate typical stellar density in massive star forming region which will be useful for future theoretical simulations.

7.3.2 Scientific Justification

A lot of efforts both theoretically and observationally has been put towards unveiling how massive stars form and evolve. The fact that high-mass stars have very significant impact on the evolution of the interstellar medium of galaxies, with strong influences on their environments by means of strong winds, expanding HII regions, UV radiation, supernovae, and sometimes activates other star formation events, underscores the importance of this research. Certainly, understanding massive star formation is very a vital part of understanding galactic evolution.

However, the difficulty in identifying and probing the early phases of massive young stellar objects underscores the fact that massive star formation has remained a poorly understood topic in the field of astronomy. Massive stars are known to form within a short timescale (10^5 years) deeply embedded in their natal clouds, in close proximity of other high-mass stars. These factors complicate the resolution of the individual MYSOs, impeding the effort to trace their evolutionary sequence.

Some theoretical simulations have been used to attempt to describe the formation scenarios of high-mass stars. There are mainly three proposed scenarios; formation

through the merging of less massive stars (Bonnell, Bate, & Zinnecker 1998), competitive accretion in a protocluster environment (Bonnell & Bate 2006), and gravitational collapse involving high-rate, disc-assisted accretion into the core which helps to overcome radiation pressure (Yorke & Sonnhalter 2002; McKee & Tan 2003; Krumholz et al. 2009).

High resolution observations are crucial in order to resolve the very early formation phases, explore the dominant formation activities and then piece it into the current knowledge of more evolved MYSOs. In order to study and trace the different evolutionary stages of massive star formation, selecting a massive star forming region which houses MYSOs at various phases of its formation is vital. NGC 6334I(N) provides such a good candidate for such study.

NGC 6334I(N) is a massive star-forming region located on the northeast of the molecular cloud/HII region complex NGC 6334 (an optical emission nebula popularly called Cat's Paw nebula). The complex extends $32'$ x $40'$ across the sky. From the sun, the distance to NGC 6334 complex was reported as 1.62 kpc (Persi & Tapia 2008). The gas mass and luminosity of NGC 6334(IN) is 400 solar masses and 10^3 solar luminosities, respectively. Kogan & Slysh (1998) and Walsh et al. (1998) detected Class I and II methanol masers which is direct evidence of the presence of protostars in the region. It is a good candidate for testing the merger formation scenario because it houses many YSOs.

7.3.3 Scientific rationale

Hunter et al. (2006) presented a $1''.5$ resolution millimeter interferometric observation (with the Submillimeter Array, SMA) results of the I(N) region, uncovering a cluster of compact dust continuum cores. 7 mm very large array (VLA) continuum observations resolved the principal SMA source (SMA1) into multiple components (Rodriguez et al. 2007). Beuther et al. (2008) traced the dominant bipolar outflow kinematics in SMA1 with HCN(1-0) observed at 3 mm. Compact CH3CN (5-4) emission was also detected towards SMA1. Brogan et al. (2009) confirmed the I(N) to be an actively forming massive protostellar cluster (estimating the dust temperatures, gas mass and column densities of the SMA sources), identifying multiple outflows.

Our proposed ALMA band 7 observation would resolve a lot more protostellar objects allowing us the rare opportunity to observationally test the merger formation

scenario proposed by Bonnell, Bate, & Zinnecker (1998). It would provide us highly sensitive image with high resolution to study the kinematics of the individual sources in the region.

The setup of our proposal would cover among other useful spectral lines, HCN and its isotopologues which are good tracers of dense gas, as well as CS lines. HCO^+ (good outflow tracer); methanol (CH_3OH), ethyl cynaide, SO_2, and SO (good tracers of hot cores), as well as CO lines.

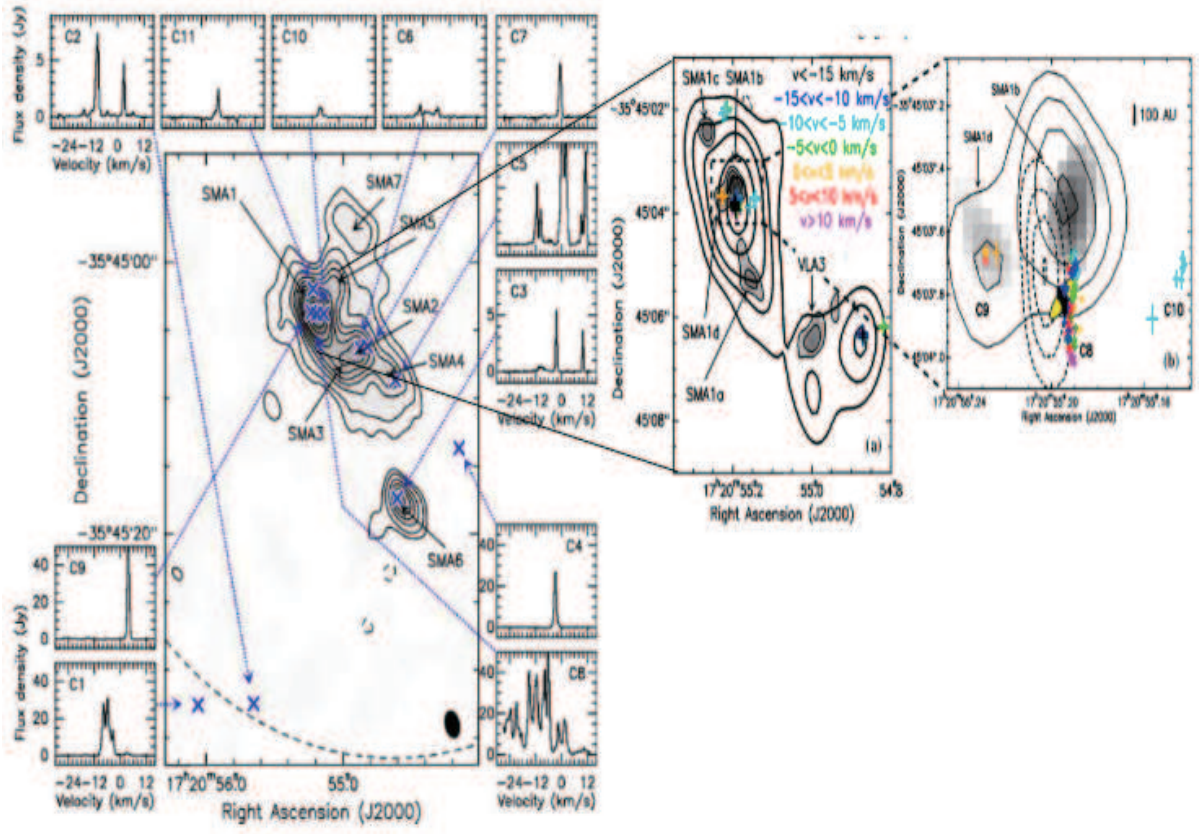

Figure 7.3: SMA contour map of NGC 6334I(N) with VLA 22 GHz H_2O masers (adapted from Brogan et al. 2009) - SMA contour map of NGC 6334I(N) with VLA 22 GHz H_2O masers (right panel), and the zoomed image of SMA 1, 2 and 3, showing the resolved components of SMA1 at 7 mm with the VLA (right panel). The dash line contour is 3.6 cm continuum associated with SMA1b component. Contour levels are 170, 250, 330, 490, and 650 mJy (for SMA continuum), -0.6, 0.6, 0.8, 1.0, 1.2 mJy beam^{-1} (7 mm VLA continuum) and 0.12, 0.20, 0.28, and 0.36 mJy (3.6 cm VLA).

Sources	RA (J2000)	Dec (J2000)	Peak Intensity (Jy beam^{-1})
SMA1	$17^h20^m55.188^s$	-35°45′03″.86	1.78
SMA2	$17^h20^m54.870^s$	-35°45′06″.50	0.57
SMA3	$17^h20^m54.999^s$	-35°45′07″.03	0.09
SMA4	$17^h20^m54.621^s$	-35°45′08″.71	0.23
SMA5	$17^h20^m55.042^s$	-35°45′01″.57	0.20
SMA6	$17^h20^m54.589^s$	-35°45′17″.46	0.88

Table 7.1: Resolve millimeter sources in NGC 6334I(N).

Resolve millimeter sources in NGC 6334I(N).

7.3.4 Immediate objective

The high sensitivity and resolution provided by the ALMA band 7 in the cycle 1 observation is vital for the exploration of the star formation activities in NGC 6334I(N). Recent SMA 218 GHz observation (see Figure 8.1: right panel) (Brogan et al. 2013 *in prep.*) shows a good number of possible protostars but the image has less sensitivity, thus the spectral indices of the protostellar candidates cannot be determined with the SMA observation. ALMA band 7 (345 GHz) 1.4-hour observation will afford us a 0.5″ resolution and 0.7 mJy beam$_{-1}$ rms near bright sources and 0.1 mJy beam$_{-1}$ in regions with no bright emissions, therefore we would be able to detect (see Figure 8.1 left panel: ALMA band 7 simulated clean image made from the 218 GHz SMA clean image), with high SNR, all the real components in the region. It would also be useful in differentiating the detected emissions into thermal, free-free (or emanating from ultra compact HII regions) by obtaining their spectra indices (advantage of the ALMA over the SMA observations).

From our simulation, the dynamic range is about 2500:1 for a 3.5-minute observation, and a peak flux of 1.78 Jy is detectable in SMA1 (see Table 8.1).

Massive stars are known to form close to each other. Resolving and confirming the number of MYSOs in the region would help to estimate the stellar density per parsec which could be typical of massive star forming regions. The inability to confirm that some bring components are actually YSOs has in the past made the estimation of MYSO population density difficult and our proposed ALMA observation will be useful

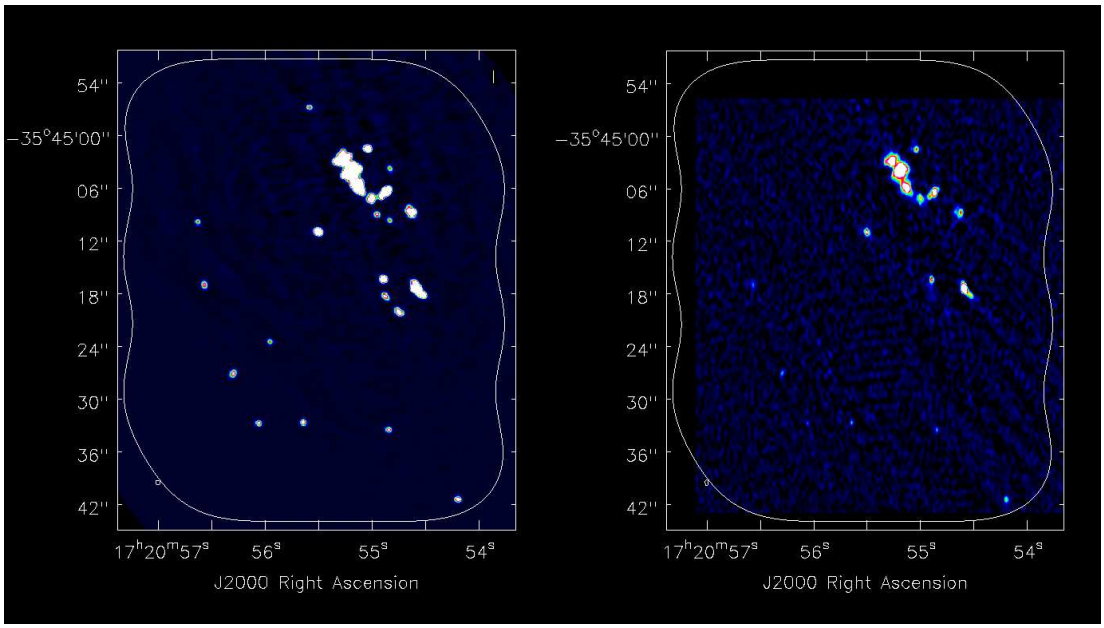

Figure 7.4: ALMA 345 GHz (band 7) simulated image of the continuum emissions from NGC 6334I((N) - SMA 218 GHz clean image (right panel) of NGC 6634I(N) and the simulated clean image (left panel) of the ALMA 345 GHz (band 7) band of the SMA clean image.

in obtaining such information about the region which could be applied to other regions for theoretical simulation purposes.

We would be able to estimate the gas masses of the individual detected sources from the dust temperatures using Equation 4 of Brogan et al. (2009). The spectral lines would be employed in obtaining the velocity dispersion of the individual source and help us ascertain the possibility of massive star formation through the merging of less massive stars.

The ALMA high resolution spectral line emissions would trace the kinematics of star formation activities like outflows (bipolar) in the resolved objects. Beuther et al. (2008) and Brogan et al. 2009 indicate the possibility of finding a good number of outflow sources. The extent, size and velocities of the outflow would be useful for tracing the star formation evolutionary sequence in the region. Objects in earlier phases of their formation may not have started violent ejections from their cores and would not show evidence of outflows.

7.3.5 Testing the Spontaneous Star Formation Scenario in Other Massive Star-forming Regions

Are there other examples of high-mass stars formed through a spontaneous process? Is the case of the massive star associated with the compact HII region (S252A) discussed in Chapter 6 an exception? Bearing in mind that Thompson et al. (2012) suggested that only about 14% of the massive stars in the Milky Way could have triggered, meaning that, the remaining 86% were formed through a different scenario, we have proposed to conduct a large-scale NH_3 line mapping observations of massive star-forming regions in the Milky Way (focusing on the galactic plane) with the Nobeyama Radio Observatory 45 m telescope (PI Prof. Handa Toshihiro).

We hope to explore the molecular gas temperature distribution in as many massive star-forming regions as possible, along with other physical properties like LTE and virial masses, sizes and tracing of shocks in the regions. The intensity ratio of NH_3 (3,3) to (1,1) is a shock indicator in molecular gas (Nagayama et al 2009).

7.3.6 Expected Scientific Results

Our already accepted NRO 45 m observation will expose the physical conditions in many massive star-forming region in the galactic plane. This would be instrumental

in exploring the extent of spontaneous star formation in the Milky Way. There is also a chance of finding evidence of sequential star formation, but the extent of such possibility is yet to be known.

We will observationally verify or debunk the Kennicutt-Schmidt law of tight correlation between less dense (CO) and dense molecular gas by comparing our NH_3 maps with the NRO 45 m CO map of the galactic plane (PI Prof. Handa Toshihiro).

As a large-scale survey, statistical study and classification of dense molecular clouds based on the scenario of star formation in the various regions. This is a new perspective in the study of dense molecular gas, we are hoping to finding the most plausible, or at least, the most statistically significant scenario of massive star formation. There is also the possibility of a spin-off of a new scenario from our research.

8

Appendix

Pipeline Scripts for Data Reduction

A pipeline for data analysis is a sequence of the analysis procedures, which is well defined from the beginning to the end of the data analysis so that all analysts using the pipeline can obtain almost the same analyzed results. A pipeline is used for several purposes in data analysis, not only to obtain a preliminary result, but also to repeat the same procedures with different parameters in order to investigate the dependence of analyzed results on the input parameters. AIPS pipelines for data of JVN/VERA observations have been developed by Hiroshi Imai and are now available to users of JVN and VERA. The manual and the scripts of the pipeline can be downloaded from the following URL: http://milkyway.sci.kagoshima-u.ac.jp/ imai/AIPS-analysis.html. Since 2010, the pipeline scripts running on the ParselTongue platform (developed in the Joint Institute for VLBI in Europe) are available from the VCON Wiki Page: http://milkyway.sci.kagoshima-u.ac.jp/groups/vcon lib/wiki/9fbfd/Data Analysis.html. The ParselTongue scripts are Python scripts. They have some extension of functions from previous POPS scripts like the MMAP used in the making of maser image map of Cepheus A VERA observations (see Chapter 3).

CASA Data Reduction Script

Considering that CASA is a new astronomy data reduction package, yet under development, I consider it necessary to append the details of the CASA data reduction script for reference purposes. It is important to note that the data reduction procedure shown below does not include the system temperature correction, which was done using the MIRIAD before loading the data in CASA.

LOADING OF THE DATA FILES

rawdata=[‘sm2-rx0.lsb.if1.tsys.ms’, ‘sm2-rx0.lsb.if2.tsys.ms’,
‘sm2-rx0.usb.if1.tsys.ms’, ’sm2-rx0.usb.if2.tsys.ms’]

DISPLAYING THE OBSERVATION DETAILS

for vis in rawdata:
os.system(‘rm ’+vis+‘.listobs’)
listobs(vis, verbose=T, listfile=vis+‘.listobs’)

DISPLAYING ANTENNAS

plotants(vis=‘sm2-rx0.lsb.if1.tsys.ms’, figfile=‘sma-ant.png’)

PLOTTING VISIBILITIES

plotms(vis=‘sm2-rx0.lsb.if1.tsys.ms’, xaxis=‘time’,
yaxis=‘amp’,field=‘’, avgchannel=‘128’, spw=‘0 23:8 120’,
coloraxis=‘field’, iteraxis=‘spw’)
Replot with the x-axis changed to frequency, uvdist (meaning UV distance).

FLAGGING OF BAD VISIBILITIES

rawdata=[‘sm2-rx0.lsb.if1.tsys.ms’, ‘sm2-rx0.lsb.if2.tsys.ms’,
‘sm2-rx0.usb.if1.tsys.ms’, ‘sm2-rx0.usb.if2.tsys.ms’]

for vis in rawdata:
flagmanager(vis=vis,mode=‘save’,versionname=‘Original’)

for vis in rawdata:
flagmanager(vis=vis,mode=‘restore’,versionname=‘Original’)
flagdata(vis=‘sm2-rx0.usb.if1.tsys.ms’,field=‘titan’, spw=‘7 23’,flagbackup=False)
flagdata(vis=‘sm2-rx0.usb.if2.tsys.ms’,field=‘titan’, spw=‘0 5’,flagbackup=False)

DATA CALIBRATION

rawdata=[‘sm2-rx0.lsb.if1.tsys.ms’, ‘sm2-rx0.lsb.if2.tsys.ms’,
‘sm2-rx0.usb.if1.tsys.ms’, ‘sm2-rx0.usb.if2.tsys.ms’]
DEFINITIONS
flux=‘titan’
bpcal=‘3c454.3’
pcal=‘1733-130’
science=‘SM2’
check=‘1924-292’
calfields=‘titan,3c454.3,1733 130,1924 292’

```
bpchans='0 23:50 60'
calchans='0 23:5 122'
(hereafter as rawdata and definitions)
    for vis in rawdata:
clearcal(vis)
setjy(vis=vis,field=flux, standard='Butler-JPL-Horizons 2010',scalebychan=F,
usescratch=True)
    os.system('rm -rf *bpphase.gcal *bcal')
for vis in rawdata:
gaincal(vis=vis,caltable=vis+'.bpphase.gcal',
field=bpcal,spw=bpchans,refant='ANT5',
calmode='p',solint='int',minsnr=3.0,minblperant=4)
for vis in rawdata:
bandpass(vis=vis,caltable=vis+'.bandpass.bcal',
field=bpcal,spw='',combine='',refant='ANT5',
solint='inf',solnorm=T,minblperant=4,fillgaps=7,
gaintable=[vis+'.bpphase.gcal'])
for vis in rawdata:
bandpass(vis=vis,caltable=vis+'.bandpass.avg4.bcal',
bandtype='B',
field=bpcal,spw='',combine='',refant='ANT5',
solint='inf,4',solnorm=T,minblperant=4,fillgaps=7,
gaintable=[vis+'.bpphase.gcal'])
    os.system('rm -rf *phase.gcal *amp.gcal')
for vis in rawdata:
gaincal(vis=vis,caltable=vis+'.intphase.gcal',
field=calfields,spw=calchans,refant='ANT5',
calmode='p',solint='int',minsnr=3.0,minblperant=4,
gaintable=[vis+'.bandpass.avg4.bcal'])
for vis in rawdata:
gaincal(vis=vis,caltable=vis+'.scanphase.gcal',
field=calfields,spw=calchans,refant='ANT5',
calmode='p',solint='inf',minsnr=3.0,minblperant=4,
```

```
gaintable=[vis+'.bandpass.avg4.bcal'])
for vis in rawdata:
gaincal(vis=vis,caltable=vis+'.amp.gcal',
field=calfields,spw=calchans,refant='ANT5',
calmode='ap',solint='inf',minsnr=3.0,minblperant=4,
gaintable=[vis+'.bandpass.avg4.bcal',vis+'.intphase.gcal'])
When you flag titan use this version:
os.system('rm -rf *flux.cal')
fluxresults={}
vis=rawdata[0]
fluxresults[vis]=fluxscale(vis=vis,caltable=vis+'.amp.gcal',
fluxtable=vis+'.flux.cal',reference=flux)

    vis=rawdata[1]
fluxresults[vis]=fluxscale(vis=vis,caltable=vis+'.amp.gcal',
fluxtable=vis+'.flux.cal',reference=flux)

    vis=rawdata[2]
fluxresults[vis]=fluxscale(vis=vis,caltable=vis+'.amp.gcal',
fluxtable=vis+'.flux.cal',reference='titan',
refspwmap=[0,1,2,3,4,5,6,6,6,6,6,6,6,6,6,6,6,6,6,6,6,6,6,6])

    vis=rawdata[3]
fluxresults[vis]=fluxscale(vis=vis,caltable=vis+'.amp.gcal',
fluxtable=vis+'.flux.cal',reference='titan',
refspwmap=[6,6,6,6,6,6,6,7,8,9,10,11,12,13,14,15,16,17,18,19,20,21,22,23])

    import numpy
numpy.median(fluxresults[rawdata[0]]['1']['fluxd'])
numpy.median(fluxresults[rawdata[1]]['1']['fluxd'])
numpy.median(fluxresults[rawdata[2]]['1']['fluxd'])
numpy.median(fluxresults[rawdata[3]]['1']['fluxd'])
```

numpy.std(fluxresults[rawdata[0]][‘1’][‘fluxd’])
numpy.std(fluxresults[rawdata[1]][‘1’][‘fluxd’])
numpy.std(fluxresults[rawdata[2]][‘1’][‘fluxd’])
numpy.std(fluxresults[rawdata[3]][‘1’][‘fluxd’])

for vis in rawdata:
setjy(vis=vis,field=pcal,
fluxdensity=[numpy.median(fluxresults[vis][‘1’][‘fluxd’]),0,0,0])

for vis in rawdata:
setjy(vis=vis,field=bpcal,
fluxdensity=[numpy.median(fluxresults[vis][‘4’][‘fluxd’]),0,0,0])

for vis in rawdata:
gaincal(vis=vis,caltable=vis+‘.amp.final.gcal’,
field=calfields,spw=calchans,refant=‘ANT5’,
calmode=‘ap’,solint=‘inf’,minsnr=2.0,minblperant=4,
gaintable=[vis+‘.bandpass.avg4.bcal’,vis+‘.intphase.gcal’])

INSPECTION OF CALIBRATION SOLUTIONS
rawdata and definitions
os.system(‘rm -rf cal-plots’)
os.system(‘mkdir cal-plots’)
for vis in rawdata:
aU.plotbandpass(caltable=vis+‘.bandpass.bcal’,ms=vis,
caltable2=vis+‘.bandpass.avg4.bcal’,
field=bpcal,xaxis=‘freq’,yaxis=‘amp’,
figfile=‘cal-plots/’+vis+‘.bandpass-avg4-amp.png’,
interactive=False,subplot=11,poln=‘X’)
Replot with y-axis set as phase, and antenna=‘1-8’.
APPLYING THE CALIBRATION SOLUTIONS
rawdata and definitions
for vis in rawdata:

flagmanager(vis=vis,mode='save',versionname='beforeapplycal')

for vis in rawdata:
applycal(vis=vis,field=bpcal,
gaintable=[vis+'.bandpass.avg4.bcal',vis+'.intphase.gcal',
vis+'.amp.final.gcal'],
interp=['nearest,linear','nearest','nearest'],
gainfield=[bpcal,bpcal,bpcal],flagbackup=F,calwt=F)
for vis in rawdata:
applycal(vis=vis,field=pcal,
gaintable=[vis+'.bandpass.avg4.bcal',vis+'.intphase.gcal',
vis+'.amp.final.gcal'],
interp=['nearest,linear','nearest','nearest'],
gainfield=[bpcal,pcal,pcal],flagbackup=F,calwt=F)

for vis in rawdata:
applycal(vis=vis,field=flux,
gaintable=[vis+'.bandpass.avg4.bcal',vis+'.intphase.gcal',
vis+'.amp.final.gcal'],
interp=['nearest,linear','nearest','nearest'],
gainfield=[bpcal,flux,flux],flagbackup=F,calwt=F)

for vis in rawdata:
applycal(vis=vis,field=science,
interp=['nearest,linear','linear','linear'],
gaintable=[vis+'.bandpass.avg4.bcal',vis+'.scanphase.gcal',
vis+'.amp.final.gcal'],
gainfield=[bpcal,pcal,pcal],flagbackup=F,calwt=F)

for vis in rawdata:
applycal(vis=vis,field=check,
interp=['nearest,linear','linear','linear'],
gaintable=[vis+'.bandpass.avg4.bcal',vis+'.scanphase.gcal',

vis+‘.amp.final.gcal’],
gainfield=[bpcal,pcal,pcal],flagbackup=F,calwt=F)

PLOT CALIBRATED DATA

plotms(vis=‘sm2-rx0.lsb.if1.tsys.ms’,xaxis=‘time’,
yaxis=‘amp’,field=‘’,avgchannel=‘128’,spw=‘0 23:8 120’,
coloraxis=‘field’,iteraxis=‘spw’,ydatacolumn=‘corrected’)

Quasars should be near zero phase, science target and Titan won’t be.

plotms(vis=‘sm2-rx0.lsb.if1.tsys.ms’,xaxis=‘time’,
yaxis=‘phase’,field=‘’,avgchannel=’128’,spw=‘0 23:8 120’,
coloraxis=‘field’,iteraxis=‘spw’,ydatacolumn=‘corrected’)

Repeated with xaxis as frequency and uvdist.

SPLIT

rawdata
vis=rawdata[0]
split(vis=vis,outputvis=‘Cal-SM2-lsbif1.split.ms’,field=‘SM2’,
spw=‘0 23:5 122’,datacolumn=‘corrected’)

vis=rawdata[1]
split(vis=vis,outputvis=‘Cal-SM2-lsbif2.split.ms’,field=‘SM2’,
spw=‘0 23:5 122’,datacolumn=‘corrected’)

vis=rawdata[2]
split(vis=vis,outputvis=‘Cal-SM2-usbif1.split.ms’,field=‘SM2’,
spw=‘0 23:5 122’,datacolumn=‘corrected’)

vis=rawdata[3]
split(vis=vis,outputvis=‘Cal-SM2-usbif2.split.ms’,field=‘SM2’,
spw=‘0 23:5 122’,datacolumn=‘corrected’)

IMAGING

os.system($'cp - rCal * split.msIMAGING'$)
plotms(vis=‘Cal-SM2-lsbif1.split.ms’,spw=’5’,xaxis=’uvdist’,
yaxis=‘amp’,field=‘’,antenna=‘’,avgtime=‘1e8’,

avgchannel='128',avgscan=F,coloraxis='spw')
Repeated with xaxis as frequency and uvdist for all data sets.
spwlsbif1='0:0 117,1:0 25;100 115,2:0 10;100 115,3:60 115,
4:0 105,5:0 40;80 110,6:0 110,7:0 110,8:50 80,9:0 35;65 115,
10:0 80,11:45 55;80 115,12:0 80,13:0 50,14:20 115,15:0 80;105 115,
16:0 115,17:0 115,18:0 115,19:0 115,20:0 115,21:0 115,22:0 115,23:0 80'
spwlsbif2='0:0 110,1:40 115,2:0 115,3:0 115,4:0 55;80 100,5:30 115,
6:0 45,7:0 60,8:0 115,9:0 115,10:0 115,11:0 115,12:0 115,13:0 115,
14:10 115,15:0 115,16:0 115,17:0 40;70 115,18:10 115,19:20 70;100 115,
20:0 90,21:80 105,22:0 100,23:75 115'
spwusbif1='0:0 20;50 115,1:0 105,2:0 115,3:0 115,4:0 115,5:0 105,6:0 115,
7:0 115,8:0 115,9:0 115,10:0 55;100 115,11:0 115,12:0 115,13:0 80,14:20 115,
15:0 115,16:0 115,17:70 100,18:0 115,19:0 80,20:70 115,21:30 50;100 115,
22:10 115,23:0 115'
spwusbif2='0:0 110,1:40 105,2:0 10;40 115,3:0 115,4:40 115,5:0 115,6:0 115,
7:0 115,8:0 50,9:0 115,10:0 115,11:0 115,12:0 115,13:65 100,14:0 115,15:0 115,
16:0 115,17:0 115,18:0 70;100 115,19:0 115,20:0 115,21:0 115,22:0 115,23:0 115'
au.findChannelRanges(invertstring=spwlsbif1,nchan=118)
au.findChannelRanges(invertstring=spwlsbif2,nchan=118)
au.findChannelRanges(invertstring=spwusbif1,nchan=118)
au.findChannelRanges(invertstring=spwusbif2,nchan=118)

inversespwlsbif1 = inverse of the above specified range
inversespwlsbif2 = inverse of the above specified range
inversespwusbif1 = inverse of the above specified range
inversespwusbif2 = inverse of the above specified range

———————————- Quick test ———————————-
os.system('rm -rf SM2-lsbif1.CONTIN')
clean(vis='Cal-SM2-lsbif1.split.ms',
imagename='SM2-lsbif1.CONTIN',
spw=spwlsbif1,field='',
mode='mfs',imagermode='csclean',

imsize=300,cell='0.5arcsec',minpb=0.25,
interactive=T,
weighting='briggs',robust=0.5,
niter=10000, threshold='0.3mJy',usescratch=F)

Subsequently, the cleaning, self-calibration and the imaging of the continuum and the individual molecular line emissions.

References

[1] Aannestad, P. A.. **Molecule Formation. II. In Interstellar Shock Waves**. *ApJS*, 1973, 25, 223

[2] Ando, K., Nagayama, T., Omodaka, T., et al.. **Astrometry of Galactic Star-Forming Region ON2N with VERA: Estimation of the Galactic Constants**. *PASJ*, 2011, 63, 45

[3] Antonuccio-Delogu, V, & Silk Joseph. **Active Galactic Nuclei Activity: Self-regulation from Backflow**. *MNRAS*, 2010, 405, 1303

[4] Ball, John A., Gottlieb, Carl A., Lilley, A. E. & Radford, H. E.. **Detection of Methyl Alcohol in Sagittarius**. *ApJ*, 1970, 162, 203

[5] Baraffe, I., Chabrier, G., Allard, F., & Hauschildt, P. H. **Evolutionary models for low-mass stars and brown dwarfs: Uncertainties and limits at very young ages**. *A&A*, 2002, 382, 563

[6] Bate, M. R.. **Predicting the properties of binary stellar systems: the evolution of accreting protobinary systems**. *MNRAS*, 2000, 314, 33

[7] Beltran, M. T., Cesaroni, R., Codella, C., et al.. **Infall of gas as the formation mechanism of stars up to 20 times more massive than the Sun**. *Nature*, 2006, 443, 427

[8] Beuther, H., Walsh, A. J., Thorwirth, S., et al.. **ATCA 3 mm observations of NGC 6334I and I(N): dense cores, outflows, and an UCH II region**. *A&A*, 2008, 481, 169

[9] Beuther, H., Thorwirth, S., Zhang, Q., et al.. **High Spatial Resolution Observations of NH3 and CH3OH toward the Massive Twin Cores NGC 6334I and NGC 6334I(N)**. *ApJ*, 2005, 627, 834

[10] Bloemhof, E. E.. **Kinematics of the H2O Masers in W49N: Analysis of the Velocity Variance-Covariance Matrix**. *ApJ*, 2000, 533, 893

[11] Bloemhof, E. E.. **Diagonalization of the velocity variance/covariance matrix as a diagnostic of maser proper motions**. *ApJ*, 1993, 406, 75

[12] Bonatto, C., & Bica, E.. **Uniform detection of the pre-main-sequence population in the five embedded clusters related to the H II region NGC 2174 (Sh2-252)**. *MNRAS*, 2011, 414, 3769

[13] Bonnell, I. A., & Bate, M. R.. **Star formation through gravitational collapse and competitive accretion**. *MNRAS*, 2006, 370, 488

[14] Bonnell, I. A., Bate, M. R., Clarke, C. J., & Pringle, J. E.. **Competitive accretion in embedded stellar clusters**. *MNRAS*, 2001, 323, 785

[15] Bonnell, I. A., Bate, M. R., & Zinnecker, H.. **On the formation of massive stars**. *MNRAS*, 1998, 298, 93

[16] Bonnell, I. A., Bate, M. R., Clarke, C. J., & Pringle, J. E.. **Accretion and the stellar mass spectrum in small clusters**. *MNRAS*, 1997, 285, 201

[17] Brogan, C. L., Hunter, T. R., Cyganowski, C. J., et al.. **Digging Into NGC 6334 I(N): Multiwavelength Imaging of a Massive Protostellar Cluster**. *ApJ*, 2009, 707, 1

[18] Brogan, C. L., Hunter, T. R., Cyganowski, C. J., et al.. **NGC 6334 I(N): Multiwavelength Imaging of a Massive Protostellar Cluster**. *ApJ*, 2013 (in prep.)

[19] Bronfman, L., Nyman, L.-A., & May, J.. **A CS(2-1) survey of IRAS point sources with color characteristics of ultra-compact HII regions**. *A&AS*, 1996, 115, 81

[20] Brunthaler, A., Reid, M. J., Menten, K. M., et al.. **Trigonometric Parallaxes of Massive Star-Forming Regions. V. G23.01-0.41 and G23.44-0.18**. *ApJ*, 2009, 693, 424

[21] Burke, B. F., & Graham-Smith, F.. **An Introduction to Radio Astronomy**. *Book*, 1997, ISBN 0521554543

[22] Carpenter, J. M., Snell, R. L., & Schloerb, F. P.. **Star Formation in the Gemini OB1 Molecular Cloud Complex**. *ApJ*, 1995a, 450, 201

[23] Carpenter, J. M., Snell, R. L., & Schloerb, F. P.. **Anatomy of the Gemini OB1 molecular cloud complex**. *ApJ*, 1995b, 445, 246

[24] Carral, P., Kurtz, Stan E., Rodríguez, L. F., et al.. **Detection of the Winds from the Exciting Sources of Shell H II Regions in NGC 6334**. *AJ*, 2002, 123, 2574

[25] Caswell, J. L., & Haynes, R. F.. **Southern H II regions - an extensive study of radio recombination line emission**. *A&A*, 1987, 171, 261

[26] Chavarra, Luis A., Allen, Lori E., Hora, Joseph L., et al.. **Spitzer Observations of the Massive Star-forming Complex S254-S258: Structure and Evolution**. *ApJ*, 2008, 682, 445

[27] Cheung, L., Frogel, J. A., Hauser, M. G., & Gezari, D. Y.. **1.0 millimeter continuum map of cool sources in the NGC 6334 complex**. *ApJ*, 1978, 226, 149

[28] Cheung, A. C., Rank, D. M., Townes, C. H., et al.. **Detection of NH_3 Molecules in the Interstellar Medium by Their Microwave Emission**. *Physical Review Letters*, 1968, vol. 21, Issue 25, pp. 1701

[29] Chibueze, J. O., Kenji, I., Omodaka, T., et al. **Star Formation in the Molecular Cloud Associated with the Monkey Head Nebula: Sequential or Spontaneous?**. *ApJ*, 2013, 762, 17

REFERENCES

[30] Chibueze, J. O., Imai, H., Tafoya, D., et al. **A Highly Collimated Water Maser Bipolar Outflow in the Cepheus A HW3d Massive Young Stellar Object**. *ApJ*, 2012, 748, 146

[31] Choi, Y. K., Hirota, T., Honma, M., et al.. **Distance to VY Canis Majoris with VERA**. *PASJ*, 2008, 60, 1007

[32] Cohen, R. J., Rowland, P. R., & Blair, M. M.. **The source of the bipolar outflow in Cepheus A**. *MNRAS*, 1984, 210, 425

[33] Conti, P. S., & Alschuler, W. R.. **Spectroscopic Studies of O-Type Stars. I. Classification and Absolute Magnitudes**. *ApJ*, 1971, 170, 325

[34] Curiel, S., Ho, P. T. P., Patel, N. A., et al.. **Large Proper Motions in the Jet of the High-Mass YSO Cepheus A HW2**. *ApJ*, 2006, 638, 878

[35] Danby, G., Flower, D. R., Valiron, P., et al.. **A recalibration of the interstellar ammonia thermometer**. *MNRAS*, 1988, 235, 229

[36] Deharveng, L., Zavagno, A., Schuller, F., et al. **Star formation around RCW 120, the perfect bubble**. *A&A*, 2009, 496, 177

[37] Deharveng, L., Zavagno, A., & Caplan, L.. **Triggered massive-star formation on the borders of Galactic H II regions. I. A search for "collect and collapse" candidates**. *A&A*, 2005, 433, 565

[38] Dobashi, K.. **Atlas and Catalog of Dark Clouds Based on the 2 Micron All Sky Survey**. *PASJ*, 2011, 63, 1

[39] Dzib, S., Loinard, L., Rodríguez, L. F., et al. **VLBA Determination of the Distance to Nearby Star-forming Regions. VI. The Distance to the Young Stellar Object HW 9 in Cepheus A**. *ApJ*, 2011, 733, 71

[40] Efremov, Y. N.. **Star Complexes and Associations: Fundamental and Elementary Cells of Star Formation**. *AJ*, 1995, 110, 275

[41] Elmegreen, B. G., & Lada, C. J.. **Sequential formation of subgroups in OB associations**. *ApJ*, 1977, 214, 725

[42] Ezoe, Y., Kokubun, M., Makishima, K., et al.. **Investigation of Diffuse Hard X-Ray Emission from the Massive Star-forming Region NGC 6334**. *ApJ*, 2006, 638, 860

[43] Feigelson, E. D., Martin, A. L. McNeill, C. J., et al.. **Stellar Clusters in the NGC 6334 Star-Forming Complex**. *AJ*, 2009, 138, 227

[44] Felli, M., Habing, H. J., & Israel, F. P.. **Aperture synthesis observations of galactic H II regions. V - The galactic nebula S 252 /NGC 2175/**. *A&A*, 1977, 59, 43

[45] Fountain, W. F., Gary, G. A., & Odell, C. R.. **An H-alpha velocity study of S252**. *ApJ*, 1983, 273, 639

[46] Gallimore, J. F., Cool, R. J., Thornley, M. D., & McMullin, J.. **Expansion of the R4 H2O Maser Arc near Cepheus A HW2**. *ApJ*, 2003, 586, 306

[47] Garay, G., Ramírez, S., Rodríguez, L. F., Curiel, S., & Torrelles, J. M.. **The Nature of the Radio Sources within the Cepheus A Star-forming Region**. *ApJ*, 1996, 459, 193

[48] Genzel, R., RHo, P.T.P., Bieging, J., & Downes, D.. **NH3 in Orion-KL - A new interpretation**. *ApJ*, 1982, 259, 103

[49] Genzel, R., Reid, M. J., Moran, J. M., & Downes, D.. **Proper motions and distances of H2O maser sources. I - The outflow in Orion-KL**. *ApJ*, 1981, 244, 884

[50] Gezari, D. Y.. **The remarkable 400 micron source NGC 6334/I/North/**. *ApJ*, 1982, 259, 29

[51] Goddi, C., Moscadelli, L., Alef, W., et al.. **Kinematics of H2O masers in high-mass star forming regions**. *A&A*, 2005, 432, 161

[52] Goddi, C., Moscadelli, L., Torrelles, J. M., et al.. **Evidence supporting the kinematic interpretation of water maser proper motions**. *A&A*, 2006, 447, 6

[53] Gutermuth, R. A., Megeath, S. T., Myers, P. C., et al.. **A Spitzer Survey of Young Stellar Clusters Within One Kiloparsec of the Sun: Cluster Core Extraction and Basic Structural Analysis**. *ApJS*, 2009, 184, 18

[54] Gutermuth, R. A., Myers, P. C., Megeath, S. T., et al.. **A Spitzer Observations of NGC 1333: A Study of Structure and Evolution in a Nearby Embedded Cluster**. *ApJ*, 2008, 674, 336

[55] Haikala, L. K.. **UBVRI photometry and polarimetry of the stars in S 252 (NGC 2175). I. The observations**. *A&AS*, 1994, 108, 643

[56] Harris, D. E.. **The Einstein Observatory Catalog of IPC X-ray Sources**. *EOCI*, 1990

[57] Henriksen, R. N., Mirabel, I. F., & Ptuskin, V. S.. *Bipolar radio sources in star-forming regions?*. *A&A*, 1991, 248, 221

[58] Hirota, T., Bushimata, T., Choi, Y. K., et al. **Astrometry of H_2O Masers in Nearby Star-Forming Regions with VERA. II. SVS13 in NGC1333**. *PASJ*, 2008, 60, 37

[59] Hirota, T., Bushimata, T., Choi, Y. K., et al. **Distance to Orion KL Measured with VERA**. *PASJ*, 2007, 59, 897

[60] Ho, P. T. P., & Townes, C. H.. *Interstellar Ammonia*. *ARA&A*, 1983, 21, 239

[61] Hoare, M. G., & Franco, J.. *in Hartquist T. W., Pittard, J. M., Falle, S. A. E. G., eds, Diffuse Matter from Star Forming Regions to Active Galaxies. Series A&SSP*, 2007, 61

[62] Honma, M., Tamura, Y., & Reid, M. J.. **Tropospheric Delay Calibrations for VERA**. *PASJ*, 2008, 60, 951

[63] Honma, M., Bushimata, T., Choi, Y. K., et al. **Astrometry of Galactic Star-Forming Region Sharpless 269 with VERA: Parallax Measurements and Constraint on Outer Rotation Curve**. *PASJ*, 2007, 59, 889

[64] Hughes, V. A., Cohen, R. J., & Garrington, S.. **High-resolution observations of Cepheus A**. *MNRAS*, 1995, 272, 469

[65] Hughes, V. A.. **Time-dependent radio sources in the star-forming region Cepheus A (east)**. *ApJ*, 1991, 383, 280

[66] Hughes, V. A.. **Radio observations of Cepheus A. I. The evolving pre-main-sequence stars in Cepheus A East?**. *ApJ*, 1988, 333, 788

[67] Hughes, V. A., & Wouterloot, J. G. A.. **The star-forming region in Cepheus A**. *ApJ*, 1984, 276, 204

[68] Hughes, V. A., & Wouterloot, J. G. A.. **The radio H II regions associated with CEP A**. *A&A*, 1982, 106, 171

[69] Hunter, T. R., Brogan, C. L., Megeath, S. T., et al.. **Millimeter Multiplicity in NGC 6334 I and I(N)**. *ApJ*, 2006, 649, 888

[70] Imai, H., Omi, R., Kurayama, T., et al. **Multiple Outflows Traced by H2O Masers around the Ultra-Compact H II Region G 34.26+0.15**. *PASJ*, 2011, 63, 1293

[71] Imai, H., Nakashima, K., Bushimata, T., et al. **Astrometry of H2O Masers in Nearby Star-Forming Regions with VERA I. IRAS 16293-2422 in Oph East**. *PASJ*, 2007, 59, 1107

[72] Imai, H., Watanabe, T., Omodaka, T., et al. **3-D Kinematics of Water Masers in the W 51A Region**. *PASJ*, 2002, 52, 741

[73] Imai, H., Kameya, O., Sasao, T., et al. **Kinematics and Distance of Water Masers in W3 IRS 5**. *ApJ*, 2000, 538, 751

[74] Jappsen, A.-K.; Klessen, R. S.; Larson, R. B.; Li, Y.; Mac Low, M.-M. **The stellar mass spectrum from non-isothermal gravoturbulent fragmentation**. *A&A*, 2005, 435, 611

[75] Jike, T., Tamura, Y., Manabe, S., et al.. **Start of regular geodetic VLBI observations within VERA network**. *ARAOJ*, 2005, 7, 48

[76] Jiménez-Serra, I., Martín-Pintado, J.; Rodríguez-Franco, A., et al. . **A Photoevaporating Rotating Disk in the Cepheus A HW2 Star Cluster**. *ApJ*, 2007, 661, 187

[77] Johnson, H. L.. **Photometric Distances of Galactic Clusters**. *ApJ*, 1957, 126, 121

[78] Kamezaki,T., Kenji, I. Omodaka, T., et al.. **Discovery of the maser feature associated with the X-ray-loud Class 0 protostar in the NGC 2264 Star Forming Region**. *ApJ*, 2013, (submitted)

[79] Kahn, F. D.. **Cocoons around early-type stars**. *A&A*, 1974, 37, 149

[80] Klessen, R. S., Ballesteros-Paredes, J., Vzquez-Semadeni, E., & Durn-Rojas, C.. **Quiescent and Coherent Cores from Gravoturbulent Fragmentation**. *ApJ*, 2005, 620, 786

[81] Kimberk, R. S., Hunter, T. R., Leiker, P. S., et al.. **A Multi-Baseline 12 GHz Atmospheric Phase Interferometer with One Micron Path Length Sensitivity**. *JAI*, 2012, 1, 150002

[82] Koenig, X. P., Leisawitz, D. T., Benford, D. J., et al.. **Wide-field Infrared Survey Explorer Observations of the Evolution of Massive Star-forming Regions**. *ApJ*, 2012, 744, 130

[83] Koenig, X. P., Allen, L. E., Gutermuth, R. A., et al.. **Clustered and Triggered Star Formation in W5: Observations with Spitzer**. *ApJ*, 2008, 688, 1142

[84] Kogan, L., & Slysh, V.. **VLA Imaging of Class I Methanol Masers at 7 Millimeters with Angular Resolution approximately 0.2 Arcseconds**. *ApJ*, 1998, 497, 800

[85] Kraemer, K. E., & Jackson, J. M.. **Molecular Gas in the NGC 6334 Star Formation Region**. *ApJS*, 1999, 124, 439

[86] Kronberger, M., Teutsch, P., Alessi, B., et al.. **New galactic open cluster candidates from DSS and 2MASS imagery**. *A&A*, 2006, 447, 921

[87] Krumholz, M. R., Mark, R., Klein, R. I., et al.. **The Formation of Massive Star Systems by Accretion**. *Science*, 2009, 323, 754

[88] Krumholz, M. R., & McKee, C. F.. **A General Theory of Turbulence-regulated Star Formation, from Spirals to Ultraluminous Infrared Galaxies**. *ApJ*, 2005a, 630, 250

[89] Krumholz, M. R., McKee, C. F., & Klein, R. I.. **A Bondi Accretion in the Presence of Vorticity**. *ApJ*, 2005b, 618, 757

[90] Kudritzki, R. P.. **Line-driven Winds, Ionizing Fluxes, and Ultraviolet Spectra of Hot Stars at Extremely Low Metallicity. I. Very Massive O Stars**. *ApJ*, 2002, 577, 389

[91] Kurayama, T., Nakagawa, A., Sawada-Satoh, S., et al. . **Annual Parallax Measurements of an Infrared Dark Cloud, MSXDC G034.43+00.24 with VERA**. *PASJ*, 2011, 63, 513

[92] Kutner, M. L., & Ulich, B. L.. **Recommendations for calibration of millimeter-wavelength spectral line data**. *ApJ*, 1981, 250, 341

[93] Lada, C. J., Blitz, L., Reid, M. J., & Moran, J. M.. **VLBI observations of the water vapor masers in Cepheus A, S252A, GL 2789, GL 2139, CO 59.79+0.04, W33B, and U Orionis**. *ApJ*, 1981, 243, 769

[94] Larson, R. B.. **Thermal physics, cloud geometry and the stellar initial mass function**. *MNRAS*, 2005, 359, 211

REFERENCES

[95] Larson, R. B., & Starrfield, S.. **On the formation of massive stars and the upper limit of stellar masses**. *A&A*, 1971, 13, 190

[96] Larson, R. B.. **Numerical calculations of the dynamics of collapsing proto-star**. *MNRAS*, 1969, 145, 271

[97] Lenzen, R.. **High velocity Herbig-Haro objects near CEP A**. *A&A*, 1988, 190, 269

[98] MacLaren, I., Richardson, K. M., & Wolfendale, A. W.. **Corrections to virial estimates of molecular cloud masses**. *ApJ*, 1988, 333, 821

[99] Mac Low, M.,& Klessen, R. S.. **Control of star formation by supersonic turbulence**. *Review of Modern Physics*, 2004, 76, 125

[100] Manabe, S., Sato, T., Sakai, S., & Yokoyama, K.. **Atmospheric Loading Effect on VLBI Observations**. *Conference proceeding GVMG*, 1991, 111

[101] McKee, C. F., & Ostriker, E. C.. **Theory of Star Formation**. *ARA&A*, 2007, 45, 565

[102] McKee, C. F., & Tan, J. C.. **The Formation of Massive Stars from Turbulent Cores**. *ApJ*, 2003, 585, 850

[103] McMullin, J. P., Waters, B., Schiebel, D., et al.. **CASA Architecture and Applications**. *ASPC*, 2007, 376, 127

[104] Megeath, S. T., Wilson, T. L., & Corbin, M. R. **Hubble Space Telescope NICMOS Imaging of W3 IRS 5: A Trapezium in the Making?**. *ApJ*, 2005, 622, 141

[105] Migenes, V., Cohen, R. J., & Brebner, G. C.. **OH maser proper motions in Cepheus A**. *MNRAS*, 1992, 253, 501

[106] Minier, V., Burton, M. G., Hill, T., et al.. **tarforming protoclusters associated with methanol masers**. *A&A*, 2005, 429, 945

[107] Moreno-Corral, M. A., Chavarria, K. C., de Lara, E., & Wagner, S.. **Hα Interferometric Optical and Near Infrared Photometric Studies of Star Forming Regions - Part One - the Cepheus-B / SH:2-155 / CEPHEUS-OB3 Association Complex**. *A&A*, 1993, 273, 619

[108] Morgan, W. W., Whitford, A. E., & Code, A. D.. **Studies in Galactic Structure. I. a Preliminary Determination of the Space Distribution of the Blue Giants**. *ApJ*, 1953, 118, 318

[109] Moscadelli, L., Reid, M. J., Menten, K. M., et al. **Trigonometric Parallaxes of Massive Star-Forming Regions. II. Cep A and NGC 7538**. *ApJ*, 2009, 693, 406

[110] Moscadelli, L., Testi, L., Furuya, R. S., et al. **First results from a VLBA proper motion survey of H2O masers in low-mass YSOs: the Serpens core and RNO 15-FIR**. *A&A*, 2006, 446, 985

[111] Mueller, K. E., Shirley, Y. L., Evans, N. J., II, & Jacobson, H. R.. **The Physical Conditions for Massive Star Formation: Dust Continuum Maps and Modeling**. *ApJS*, 2002, 143, 469

[112] Nagayama, T., Omodaka, T., Nakagawa, A. et al.. **Astrometry of Galactic Star-Forming Region Onsala 1 with VERA: Estimation of Angular Velocity of Galactic Rotation at the Sun**. *PASJ*, 2011, 63, 23

[113] Nakajima, T., Kaiden, M., Korogi, J., et al.. **A New 60-cm Radio Survey Telescope with the Sideband-Separating SIS Receiver for the 200 GHz Band**. *PASJ*, 2007, 59, 1005

[114] Nakano, T., Hasegawa, T., & Norman, C.. **The Mass of a Star Formed in a Cloud Core: Theory and Its Application to the Orion A Cloud**. *ApJ*, 1995, 450, 183

[115] Nakano, T.. **Conditions for the formation of massive stars through nonspherical accretion**. *ApJ*, 1989, 345, 464

[116] Neckel, T.. **UBV, VRI and H-beta observations of stars in the H II regions NGC 6334 and NGC 6357**. *A&A*, 1978, 69, 51

[117] Padoan, Paolo, & Nordlund, Ake. **The Stellar Initial Mass Function from Turbulent Fragmentation**. *ApJ*, 2002, 576, 870

[118] Palla, F., & Stahler, S. W.. **The Pre-Main-Sequence Evolution of Intermediate-Mass Stars**. *ApJ*, 1993, 418, 414

[119] Pankonin, V., Churchwell, E., Watson, C., & Bieging, J. H. **A Methyl Cyanide Search for the Earliest Stages of Massive Protostars**. *ApJ*, 2001, 558, 194

[120] Patel, N. A., Curiel, S., Sridharan, T. K., et al.. **A disk of dust and molecular gas around a high-mass protostar**. *Nature*, 2005, 437, 109

[121] Perryman, M. A. C., Lindegren, L., Kovalevsky, J., et al.. **The HIPPARCOS Catalogue**. *A&A*, 1997, 323, 49

[122] Persi, P., & Tapia, M.. **Star Formation in NGC 6334**. *Handbook on Star Formation 2*, 2008, 456

[123] Petry, D., CASA Development Team.. **Analysing ALMA Data with CASA**. *ASPC*, 2012, 461, 849

[124] Prasad, S. S., & Huntress, W. T., Jr.. **A model for gas phase chemistry in interstellar clouds. I - The basic model, library of chemical reactions, and chemistry among C, N, and O compounds**. *ApJS*, 1980, 43, 1

[125] Reid, M. J., Menten, K. M., Zheng, X. W., et al.. **Trigonometric Parallaxes of Massive Star-Forming Regions. VI. Galactic Structure, Fundamental Parameters, and Noncircular Motions**. *ApJ*, 2009, 700, 137

[126] Rodríguez, L. F., Zapata, L. A., & Ho, P. T. P.. **Compact Centimeter and Millimeter Sources in NGC 6334 I(N): OB Stars in the Making?**. *ApJ*, 2007, 654, L143

[127] Rodríguez, L. F., Garay, G., Curiel, S., et al.. **Cepheus A HW2: A powerful thermal radio jet**. *ApJ*, 1994, 430, L65

[128] Rodríguez, L. F., & Canto, J.. **Stellar Winds and Molecular Clouds - a Search for Ionized Stellar Winds**. *RMxAA*, 1983, 8, 163

[129] Russeil, D., Zavagno, A., Motte, F., et al.. **The earliest phases of high-mass star formation: the NGC 6334-NGC 6357 complex**. *A&A*, 2010, 515, 55

[130] Sandell, G.. **(Sub)mm continuum mapping of NGC 6334 I & I(N). A cobweb of filaments and protostars**. *A&A*, 2000, 358, 242

[131] Sanna, A., Reid, M. J., Moscadelli, L., et al.. **Trigonometric Parallaxes of Massive Star-Forming Regions. VII. G9.62+0.20 and the Expanding 3 kpc ARM**. *ApJ*, 2009, 706, 464

[132] Sargent, A. I.. **Molecular clouds and star formation. I - Observations of the Cepheus OB3 molecular cloud**. *ApJ*, 1977, 218, 736

[133] Sato, M., Hirota, T., Honma, M., et al.. **Distance to NGC 281 in a Galactic Fragmenting Superbubble: Parallax Measurements with VERA**. *PASJ*, 2008, 60, 975

[134] Sault, R. J., Teuben, P. J., & Wright, M. C. H.. **A Retrospective View of MIRIAD**. *ASPC*, 1995, 77, 433

[135] Sharpless, S.. **A Catalogue of H II Regions**. *ApJS*, 1959, 4, 257

[136] Shepherd, D. S., & Churchwell, E.. **Bipolar Molecular Outflows in Massive Star Formation Regions**. *ApJ*, 1996, 472, 225

[137] Shu, F. H., Adams, F. C., & Lizano, S.. **Star formation in molecular clouds - Observation and theory**. *ARA&A*, 1987, 25, 23

[138] Shu, F. H.. **Self-similar collapse of isothermal spheres and star formation**. *ApJ*, 1977, 214, 488

[139] Siess, L., Dufour, E., & Forestini, M.. **An internet server for pre-main sequence tracks of low- and intermediate-mass stars**. *A&A*, 2000, 358, 593

[140] Snyder, L. E., & Buhl, D.. **Detection of Possible Maser Emission Near 3.48 Millimeters from an Unidentified Molecular Species in Orion**. *ApJ*, 1974, 189, 31

[141] Snyder, L. E., Buhl, D., Zuckerman, B., & Palmer, P.. **Microwave Detection of Interstellar Formaldehyde**. *Physical Review Letters*, 1969, vol. 22, Issue 13, pp. 670

[142] Sofue, Y., & Reich, W.. **Radio continuum observations of the North Polar Spur at 1420 MHz**. *A&AS*, 1979, 38, 251

[143] Surcis, G., Vlemmings, W. H. T., Curiel, S., et al.. **The structure of the magnetic field in the massive star-forming region W75N**. *A&A*, 2011, 527, 48

[144] Tej, A., Ojha, D. K. Ghosh, S. K., et al.. **A multi-wavelength study of the massive star-forming region IRAS 06055+2039 (RAFGL 5179)**. *A&A*, 2006, 452, 203

[145] Thompson, M. A., Urquhart, J. S., Moore, T. J. T., & Morgan, L. K.. **The statistics of triggered star formation: an overdensity of massive young stellar objects around Spitzer bubbles**. *MNRAS*, 2012, 421, 408

[146] Torrelles, J. M., Patel, N. A., Curiel, S., et al. **A wide-angle outflow with the simultaneous presence of a high-velocity jet in the high-mass Cepheus A HW2 system**. *MNRAS*, 2011, 410, 627

[147] Torrelles, J. M., Patel, N. A., Curiel, S., et al. **The Circumstellar Structure and Excitation Effects around the Massive Protostar Cepheus A HW 2**. *ApJ*, 2007, 666, 37

[148] Torrelles, J. M., Patel, N. A., Anglada, G., et al. **Evidence for Evolution of the Outflow Collimation in Very Young Stellar Objects**. *ApJ*, 2003, 598, L115

[149] Torrelles, J. M., Patel, N. A., Gómez, J. F., et al. **Spherical episodic ejection of material from a young star**. *Nature*, 2001a, 411, 277

[150] Torrelles, J. M., Patel, N. A., Nimesh, A., et al. **Discovery of Linear "Building Blocks" of Water Masers Shaping Linear/Arcuate Microstructures in Cepheus A**. *ApJ*, 2001b, 560, 853

[151] Torrelles, J. M., Gómez, J. F., Garay, G., et al. **Systems with H_2O Maser and 1.3 Centimeter Continuum Emission in Cepheus A**. *ApJ*, 1998, 509, 262

[152] Toujima, H., Nagayama, T., Omodaka, T., et al. **Propagation of Highly Efficient Star Formation in NGC 7000**. *PASJ*, 2011, 63, 1259

[153] Turner, B. E.. **A molecular line survey of Sagittarius B2 and Orion-KL from 70 to 115 GHz. II - Analysis of the data**. *ApJS*, 1991, 76, 617

[154] Ungerechts, H., Walmsley, C. M., & Winnewisser, G.. **Ammonia and cyanoacetylene observations of the high density core of L 183 /L 134 n/**. *A&A*, 1980, 88, 259

[155] Vlemmings, W. H., T., Surcis, G., Torstensson, K. J. E., & van Langevelde, H. J.. **TMagnetic field regulated infall on the disc around the massive protostar CepheusAHW2**. *MNRAS*, 2010, 404, 134

[156] Vlemmings, W. H., T., Diamond, P. J., van Langevelde, H., J., & Torrelles, J. M.. **The magnetic field in the star-forming region Cepheus A. from H2O maser polarization observations**. *A&A*, 2006, 448, 597

[157] Walborn, N. R., Barb, R. H., Brandner, W., et al.. **Some Characteristics of Current Star Formation in the 30 Doradus Nebula Revealed by HST/NICMOS**. *AJ*, 1999, 117, 225

[158] Walborn, N. R., Morrell, N. I., Howarth, I. D., et al.. **A CNO Dichotomy among O2 Giant Spectra in the Magellanic Clouds**. *ApJ*, 2004, 608, 1028

[159] Walborn, N. R.. **Spectral classification of OB stars in both hemispheres and the absolute-magnitude calibration**. *AJ*, 1972, 77, 312

[160] Walmsley, C. M., & Ungerechts, H.. **Ammonia as a molecular cloud thermometer**. *A&A*, 1983, 122, 164

[161] Walsh, A. J., Burton, M. G., Hyland, A. R., & Robinson, G.. **Studies of ultracompact HII regions - II. High-resolution radio continuum and methanol maser survey**. *MNRAS*, 1998, 301, 640

[162] Weaver, H., Williams, D. R. W., Dieter, N. H., & Lum, W. T.. **Observations of a Strong Unidentified Microwave Line and of Emission from the OH Molecule**. *Nature*, 1965, 208, 29

[163] Weinreb, S., Barrett, A. H., Meeks, M. L., & Henry, J. C.. **Radio Observations of OH in the Interstellar Medium**. *Nature*, 1963, 200, 829

[164] Westerhout, G.. **A survey of the continuous radiation from the Galactic System at a frequency of 1390 Mc/s**. *BAN*, 1958, 14, 215

[165] Wolfire, M. G., & Cassinelli, J. P.. **Conditions for the formation of massive stars**. *ApJ*, 1987, 319, 850

[166] Wu, Y. W., Xu, Y., Pandian, J. D., et al.. **Ammonia and CO Observations Toward Low-luminosity 6.7 GHz Methanol Masers**. *ApJ*, 2010, 720, 392

[167] Yorke, H. W., & Sonnhalter, C.. **On the formation of massive stars**. *ApJ*, 2002, 569, 846

[168] Zinnecker, H., & Yorke, H. W. **Toward Understanding Massive Star Formation**. *AR&A*, 2007, 45, 481

[169] Zinnecker, H., McCaughrean, M. J., & Wilking, B. A.. **The Initial Stellar Population**. *Protostars and planets III*, 1993, (A93-42937 17-90), p. 429-495

Declaration

I herewith declare that I have produced this paper without the prohibited assistance of third parties and without making use of aids other than those specified; notions taken over directly or indirectly from other sources have been identified as such. This paper has not previously been presented in identical or similar form to any other Japanese or foreign examination board.

The thesis work was conducted from 2010 to 2013 under the supervision of Prof. Handa Toshihiro at Kagoshima University.

Kagoshima, Japan